2016

Magnetic sensors based on topological insulators

Yan Ni
Iowa State University

Magnetic sensors based on topological insulators

by

Yan Ni

A dissertation submitted to the graduate faculty

in partial fulfillment of the requirements for the degree of

DOCTOR OF PHILOSOPHY

Major: Electrical Engineering

Program of Study Committee:

David C. Jiles, Major Professor

Mani Mina

Rana Biswas

Jiming Song

Meng Lu

Ulrike Genschel

Iowa State University

Ames, Iowa

2016

DEDICATION

I would like to dedicate this dissertation to my parents Jingwei Ni and Xiaoqin Yan and to my husband Zhen Zhang.

TABLE OF CONTENTS

LIST OF FIGURES vii

NOMENCLATURE xii

ACKNOWLEDGMENTS xiii

ABSTRACT xiv

CHAPTER 1. INTRODUCTION 1

1.1 Magnetic Sensors and Material Aspect Consideration 1
1.2 Hall Effect, Quantum Hall Effect and Quantum Spin Hall Effect 2
1.2.1 Hall effect 2
1.2.2 Integer quantum Hall effect 6
1.2.3 Quantum spin Hall effect 8
1.3 Topological Insulators 9
1.3.1 Band theory, topology of solids and symmetries 9
1.3.2 Ferromagentism in topological insulators and anomalous Hall effect 15
1.4 Topological Insulator Based Devices 19
1.4.1 Proposed devices based on topological insulator 19
1.4.1 Background of magnetoelectric and multiferroic 23
1.5 Motivation and Objectives 27

CHAPTER 2. SAMPLE SYNTHESIS AND MAJOR EXPERIMENTAL TECHNIQUES .. 30

2.1 Molecular Beam Epitaxy (MBE) 30
2.2 Hall Sensor Fabrication by Plasma Etching and E-beam Lithography 35
2.3 X-ray Diffraction Measurement (XRD) 37
2.4 Atomic Force Microscopy (AFM) 40
2.5 Composite Sample Preparation Procedures 41

CHAPTER 3. TOPOLOGICAL INSULATOR GROWTH AND CHARACTERIZATION. 44

3.1 Introduction 44
3.2 Source Material Temperature and Flux Rate Control 45
3.3 Substrates Selection for Device Application 48
3.4 Substrate Temperature Effect on Film Quality 51
3.5 Element Doping in Thin Film Growth 52
3.6 Characterization on Phase Formation of TI 55

CHAPTER 4. MAGNETOTRANSPORT STUDY OF TOPOLOGICAL INSULATOR THIN FILM ON MICA SUBSTRATE 57

4.1 Introduction 57
4.2 Experiment 58
4.3 Results and Discussion 59
4.3.1 Structure of $(Sb_{1-x}Bi_x)_2Te_3$ thin films deposited on mica substrate 59
4.3.2 Effect of Bi on sheet resistivity of $(Sb_{1-x}Bi_x)_2Te_3$ thin films 60
4.3.3 Weak antilocalization of $(Sb_{0.957}Bi_{0.043})_2Te_3$ thin films under low magnetic field 62
4.3.4 Quantum oscillation of $(Sb_{0.957}Bi_{0.043})_2Te_3$ thin films under high magnetic field 63
4.4 Conclusion 64

CHAPTER 5. STUDY ON MAGNETICALLY DOPED TOPOLOGICAL INSULATOR . 66

5.1 Introduction 66
5.2. Experiments 68
5.3. Results and Discussion 68
5.3 1 Structural Characterization of $Cr_xBi_{2-x}Te_3$ thin films 68
5.3.3 Electrical transport and anomalous Hall effect of $Cr_xBi_{2-x}Te_3$ thin films 72
5.3.4 Critical property of the ferromagnetism in $Cr_xBi_{2-x}Te_3$ thin films 74
5.4 Conclusion 75

CHAPTER 6. HALL EFFECT SENSOR BASED ON TOPOLOGICAL INSULATORS ... 77

6.1 Introduction 77
6.2 Experiment 79

6.3 Results and Discussion 80
6.3.1 Crystal structure of $Mn_xBi_{2-x}Te_3$ Hall effect sensors 80
6.3.2 Surface morphology of $Mn_xBi_{2-x}Te_3$ and $Cr_xBi_{2-x}Te_3$ Hall effect sensors 81
6.3.3 Electric transport properties of $Mn_xBi_{2-x}Te_3$ and $Cr_xBi_{2-x}Te_3$ Hall effect sensors 83
6.3.4 The effect of temperature and Mn concentration on sensitivity of $Mn_xBi_{2-x}Te_3$ Hall effect sensors 85
6.4 Conclusion 87

CHAPTER 7. ANOMALOUS HALL EFFECT SENSOR BASED ON TOPOLOGICAL INSULATOR 88

7.1 Introduction 88
7.2 Experiment 90
7.3 Results and Discussion 90
7.3.1 Surface morphology and crystal structure of $Cr_{0.14}Bi_{1.86}Te_3$ Hall effect sensors 90
7.3.2 Magneto-transport properties of $Cr_{0.14}Bi_{1.86}Te_3$ Hall effect sensors 92
7.3.3 The effect of temperature on sensitivity of $Cr_xBi_{2-x}Te_3$ Hall effect sensors 96
7.4 Conclusion 97

CHAPTER 8. MAGNETIC SENSOR BASED ON MAGNETOELECTRIC EFFECT IN COBALT FERRITE AND BARIUM TITANATE COMPOSITE..... 99

8.1 Introduction 99
8.2 Experiment 100
8.3 Results and Discussion 101
8.4. Conclusion 108

CHAPTER 9. ULTRAFAST OBSERVATION OF DEMAGNETIZATION IN MAGNETICALLY DOPED TOPOLOGICAL INSULATORS 109

9.1. Introduction 109
9.2. Ultrafast Time-Resolve Magneto-Optical Kerr Spectroscopy Setup 109
9.3. Results and Discussions 111

CHAPTER 10. CONCLUSION 114

REFERENCES 121

LIST OF FIGURES

Figure 1.1	Schematic picture of simple plate model to demonstrate Hall effect.	3
Figure 1.2	The discovery of quantum Hall effect on a silicon MOSFET at liquid helium temperature. The quantized plateau on Hall resistance and vanish of longitudinal resistance can be observed.	7
Figure 1.3	Band structure of toplogical insulators and other insulators.	11
Figure 1.4	Edge and surface states of topological insulators	13
Figure 1.5	Idealized band structure of topological insulators.	14
Figure 1.6	Ideal 3D topological insulator band structure and ferromagnetic topological insulators band structure.	15
Figure 1.7	Schematic picture of quantum Hall effect and quantum anomalous Hall effect.	16
Figure 1.8	Quantum Hall trio.	17
Figure 1.9	Crystal structure and quintuple layer.	19
Figure 1.10	(a) Proposed current switch devices. Orientating $\vec{M}$ perpendicular to the TI surface leads to high resistance state, whereas the low resistance state is restored when M is parallel with the TI surface. (b) Comparison on $R_{on/off}$ ratio and electricresistivity between TI-based current switch devices and other high magnetoresistance materials.	20
Figure 1.11	A proposed current switch device based on the manipulation of surface states. The magnetization direction of ferromagnetic oxide can be adjusted via an electrical field applied on the metal gate (b). When θ is 90°, surface gap is open, resulting in massive Fermions with low mobility (a); however, when θ is 0°, surface remains gapless, leading to massless Fermions with high mobility (c). By controlling the magnetization directions, the switch could be operated with $R_{on/off}$ states (d).	22
Figure 1.12	Magnetoelectric multiferroic composite design.	26
Figure 1.13	Schematic picture of surface state and Dirac cone in Bi_2Se_3 (a) and Bi_2Te_3 (b); and their relative constant-energy contours of Dirac cones(c) Bi_2Se_3 and (d) Bi_2Te_3.	28
Figure 2.1	Sample fabrication and characterization flow chart of magnetoelectric multiferroic sensor.	31

Figure 2.2	Molecular Beam Epitaxy (a) Schematic picture of MBE vacuum chamber (b) Picture of MBE used in this work.	33
Figure 2.3	Mica crystal(a) and mica substrate(b). Mica crystal structrure(c). Schematic picture of van der Waals epitaxy of TI on mica(d) and sample on mica in present work(e).	34
Figure 2.4	Schematic showing an Ewald sphere with radius k0 cutting into the surface reciprocal rods, leading to a diffraction pattern.	36
Figure 2.5	Schematic picture of plasma etching for Hall sensor fabrication (a) and equipment in use for this work (b).	37
Figure 2.6	Electron beam lithography process of sensor fabrication. Flow chart of Hall sensor fabrication (a) and Raith e-beam lithography (b).	39
Figure 2.7	Schematic picture of (a) X-ray diffraction machine setup (b) incident X-rays with certain wavelength interact with crystal producing constructive interference.	41
Figure 2.8	Schematic picture of atomic force microscopy (AFM).	42
Figure 3.1	Vapor pressure curves of solid elements.	46
Figure 3.2	Thickness of Te and Sb thin film as a function of source temperature when substrates were at room temperature.	47
Figure 3.3	AFM image of Sb_2Te_3 film on <111> GaAs (a) before deoxidation and (b) after deoxidation at 600°C.	49
Figure 3.4	(a) AFM image of a Sb_2Te_3 thin film deposited on mica substrate. Inset shows its streaky RHEED pattern, indicating the 2D-growth of thin film. (b) Topography of Sb_2Te_3 thin film along the dashed line, displays the quintuple-layer structure. (c) Thickness profile of Sb_2Te_3 thin film.	50
Figure 3.5	Surface morphology of Sb_2Te_3 film on (a) <111> Si (b) <111> GaAs (c) mica substrate.	51
Figure 3.6	Surface morphology of Sb_2Te_3 film on mica substrate with different substrate temperatures (a) 170°C (b) 200°C (c) 210°C (d) 230°C (e) 235 °C; (f) RMS roughness of above samples.	52
Figure 3.7	Composition and structure analysis of $(Sb_{1-x}Bi_x)_2Te_3$. (a) The EDS spectrum of $(Sb_{1-x}Bi_x)_2Te_3$ with x = 0.18. (b) Bi concentration of $(Sb_{1-x}Bi_x)_2Te_3$ as a function of Bi diffusion cell temperature.	54
Figure 3.8	AFM images of $(Sb_{1-x}Bi_x)_2Te_3$ thin film as a function of Bi concentration x. Large amount of pyramidal-shape terraces over ten quintuple layers can be observed when x > 0.11.	55
Figure 3.9	Reflection High-Energy Electron Diffraction (RHEED) as real-time tool to monitor the surface of TI thin film	56

Figure 4.1	Characterization of topological insulator thin films (a) ~ (d) AFM image of thin films $(Sb_{1-x}Bi_x)_2Te_3$ grown on mica substrate, where (a) x = 0.0, (b) x = 0.014, (c) x = 0.043, and (d) x = 0.07. RHEED pattern of thin film (Sb_2Te_3) during growth is shown in (a) inset. (e) Height profile of Sb_2Te_3 thin film along the dashed line in (a). (c) XRD profile of $(Sb_{1-x}Bi_x)_2Te_3$ thin film with x = 0.043.	60
Figure 4.2	Schematic illustrations on tuning the Fermi level and surface Dirac point of $(Sb_{1-x}Bi_x)_2Te_3$ with increasing Bi concentration. (b) Sheet resistivity of $(Sb_{1-x}Bi_x)_2Te_3$ thin films at room temperature.	61
Figure 4.3	(a) Magnetoconductance of $(Sb_{1-x}Bi_x)_2Te_3$ with x = 0.043 at low magnetic field. (b) Fitting of conductance change with Hikami-Larkin-Nagaoka (*HLN*) model. (c) Phase coherence length as a function of temperature, fitted with power law $L_\Phi \sim T^\beta$.	62
Figure 4.4	(a) Shubnikov-de Hass (SdH) oscillation of Hall resistance for $(Sb_{1-x}Bi_x)_2Te_3$ with x = 0.043 at 2.5 K. Inset shows the periodical oscillation of dR_{xy}/dB with $1/B$. (c) SdH oscillation behavior of its magnetoconductance as various temperatures. (d) Normalized conductivity amplitude, fitted with Lifshitz-Kosevich (LK) model.	64
Figure 5.1	Structural characterization of $Cr_xBi_{2-x}Te_3$ thin films. (a) AFM images of $Cr_xBi_{2-x}Te_3$, with x = 0.00, 0.14, and 0.29. (b) Surface RMS roughness as a function of Cr concentration in $Cr_xBi_{2-x}Te_3$. (c) XRD pattern of $Cr_xBi_{2-x}Te_3$ with x = 0.29 grown on mica substrate	69
Figure 5.2	(a) The temperature dependence of magnetization under 0.05 T for $Cr_xBi_{2-x}Te_3$ with x=0.03, 0.14, and 0.29. (b) The corresponding dM/dT vs. T curves.	71
Figure 5.3	(a1), (a2), and (a3) Hall resistance curves at low magnetic field for $Cr_xBi_{2-x}Te_3$ with x = 0.03, 0.14, and 0.29 respectively. (b1), (b2), and (b3) Corresponding normalized magnetoconductance curves. The temperature dependent carrier concentration of $Cr_xBi_{2-x}Te_3$ is shown in (a1) inset.	73
Figure 5.4	(a) and (c) Arrott plot at various temperatures for $Cr_xBi_{2-x}Te_3$ with x= 0.14 and 0.29 respectively. (b) and (d) Arrott-Noakes plot at various temperatures for $Cr_xBi_{2-x}Te_3$ with x= 0.14 and 0.29 respectively, assuming $\beta = 0.36$ and $\gamma = 1.386$.	75
Figure 6.1	X-ray diffraction patterns of $Mn_xBi_{2-x}Te_3$ Hall effect sensor fabricated on mica substrate with (a) x = 0.01, (b) x = 0.08, and	81

	(c) x = 0.23, where diffraction peaks from mica substrate and $Mn_xBi_{2-x}Te_3$ thin film are indexed in blue and red, respectively.	
Fgiure 6.2	(a), (b), and (c) Surface morphology of $Mn_xBi_{2-x}Te_3$ thin films with x= 0.01, x=0.08, and x=0.23, respectively, (d) Hall effect sensor fabricated with $Mn_xBi_{2-x}Te_3$ thin films, and geometry of Hall effect measurement.	82
Figure 6.3	Temperature dependence of Hall resistance curves under low magnetic field for $Mn_xBi_{2-x}Te_3$ HE sensor with (a) x=0.01, (b) x = 0.08, and (c) x=0.23. (d) Temperature dependence of coercive field for $Mn_xBi_{2-x}Te_3$ HE sensor with x=0.23. Inset shows the temperature dependence of longitudinal resistance (R/R_{30K}) of sensors at various Mn concentrations.	85
Figure 6.4	The effect of temperature and Mn concentration on Hall sensitivity of $Mn_xBi_{2-x}Te_3$ HE sensor with x = 0.01, 0.08, and 0.23.	87
Figure 7.1	Characterization of $Cr_{0.14}Bi_{1.86}Te_3$ based sensors with different deposition duration. (a) and (b) surface morphology; (c) and (d) thickness; (e) and (f) X-ray diffraction patterns of sensors with 30min and 2hour growth, respectively.	91
Figure 7.2	Temperature dependence of Hall resistance curves for $Cr_xBi_{2-x}Te_3$ HE sensor with different thickness. (a) T = 20K, (b) T = 10K, (c) T = 7.5K, and (d) T= 2.5K. (e) temperature dependence of saturation field for $Cr_xBi_{2-x}Te_3$ HE sensor and (f) saturation Hall resistivity at zero magnetic field. The dashed lines in (e) and (f) are guides to the eye.	93
Figure 7.3	Carrier density(a) and carrier mobility(b) of TI AHE sensor with 15 nm and 65 nm thickness $Cr_xBi_{2-x}Te_3$ thin film.	95
Figure 7.4	Temperature dependence of sensitivity for $Cr_xBi_{2-x}Te_3$ AHE sensor with different thickness. Inset shows the schematic picture of HE sensor under testing. The green curve shows the topological insulator thin film Mn doped Bi_2Te_3 with similar testing condition.	97
Figure 8.1	Characterization of samples used for ME sensor. (a), (b), (c), and (d) SEM image and (e) XRD pattern of $CoGa_xFe_{2-x}O_4/BaTiO_3$ (x = 0.3) and EDS images.	102
Figure 8.2	Magnetic properties of $CoGa_xFe_{2-x}O_4/BaTiO_3$ (x = 0, 0.1, 0.2 ,0.3) at room temperature: (a) magnetization curve, (b) saturation magnetization (Ms), (c) remnant magnetization (Mr), and (d) magnetic coercive field.	103

Figure 8.3	Magnetostriction (λ) vs. magnetic field (H) curves for $CoGa_xFe_{2-x}O_4/BaTiO_3$ (x = 0, 0.1, 0.2, 0.3). (b) dλ/dH as a function of magnetic field (H). (c) The maximum sensitivity of magnetostriction with respect to different Ga concentrations.	105
Figure 8.4	(a) Ferroelectric properties of $CoGa_xFe_{2-x}O_4/BaTiO_3$ composites (x = 0, 0.1, 0.2, 0.3). (b) Remnant polarization and electric coercive field with different Ga concentration in the ferromagnetic phase. (c) Loss tangent as a function of temperature at 10 kHz frequency. (d) The unipolar electric-field-induced strain S(E) curves.	107
Figure 9.1	Ultrafast time-resolve magneto-optical Kerr spectroscopy setup with topological insulator samples	110
Figure 9.2	Schematic picture of pump laser interacting with magnetically doped TI thin film sample (a); Temperature dependence of the photoinduced MOKE signal first 300 ps with fitting curves in red (b).	111
Figure 9.3	Temperature dependent rise and decay time constants.	112

NOMENCLATURE

AFM	Atomic Force Microscope
AHE	Anomalous Hall Effect
ARPES	Angle-resolved Photoemission Spectroscopy
EDS	Energy-dispersive X-ray Spectroscopy
HE	Hall Effect
ME	Magnetoelectric
MEMF	Magentoelectric Multiferroic
MR	Magnetoresistance
PPMS	Physical Properties Measurement System
RHEED	Reflection High-energy Electron Diffraction
SdH	Shubnikov-de Haas
SOC	Spin-orbital Coupling
SS	Surface State
TI	Topological Insulator
TRS	Time-reversal Symmetry
VDWE	Van de Waals Epitaxy
WAL	Weak Anti-localization
WL	Weak Localization
XRD	X-ray Diffraction

ACKNOWLEDGMENTS

I would like to thank my major professor, Dr. David. C. Jiles for supporting me during my PhD study. I also thank my committee members Dr. Mani Mina, Dr. Rana Biswas, Dr. Jiming Song, Dr. Meng Lu and Dr. Ulrike Genschel for their guidance and support throughout the course of this research. My sincere thanks also go to Dr. John Basart who read my thesis carefully and gave modification suggestion. In addition, I would also like to thank my friends, colleagues, the department faculty and staff for making my time at Iowa State University a wonderful experience. Last but not least, without my husband Dr. Zhen Zhang and my parents, I could not come to United States for graduate study. I would like to thank them for supporting me spiritually throughout my study, my thesis writing and my life in general.

ABSTRACT

The ever-increasing demands for higher computing capabilities and low energy consumption has necessitated the developing of micro or nano electronics and sensors. This results in increasing demand for faster, higher performance, more compact and low energy consumption devices and sensors which pushes microelectronics to their physical limit. Driven by size, cost, sensitivity, reliability and power consumption, the electronic and magnetic related devices are entering a completely new age where innovations on new materials and physics are being explored. Among the most promising materials, magnetoelectric multiferroic (MEMF) and topological insulators (TI) have attracted a great deal of interest, since they are promising for their unique properties and innovative applications. The coupling of electric and magnetic properties of MEMF and the ultrahigh surface carrier mobility of TI enlighten the design of devices with extremely low thermal losses and energy cost.

However, most of the device implementations of these material systems are still in status of ideas and laboratory prototypes. The prospects of practical realization of devices based on MEMF and TI encounter several critical challenges: the low ME coupling coefficient and current leakage in ME sensor; fabrication large scale, low roughness and large terrace width of TI thin films for industry utilization; the high bulk conductivity and low sensitivity of TI based magnetic sensors. The present thesis will address some problems and challenges based on the above questions.

In this work, several aspects regarding to achieve a high performance and low energy consuming devices were investigated including: systemically studied and manipulated the energy band structure of TI for nanosized electronics and sensors application; developed Hall effect sensor and AHE sensor based on magnetically doped topological insulator; explored a

method to increase the ME coupling coefficient of ME sensors; There are nine chapters in this dissertation. Chapter 1 gives general background to readers on magnetic sensors which used widely in daily life. Basic physics of two kinds of important materials: topological insulators and MEMF composites will also be introduced. Besides that, Chapter 1 will also introduce a proposed switching device which integrates both two kinds of materials. The last part of Chapter 1 will be the motivation and objectives of work in this dissertation. Chapter 2 will review the experiments, techniques and equipment used for research in this dissertation including sample fabrication methods and testing methods. Starting from Chapter 3, topological insulators material fabrication and sensor application will be introduced based on different kind of TIs. Study on MEMF sensors will be introduced in Chapter 8. Chapter 9 is a summary of all the work and gives some general conclusions of this dissertation.

CHAPTER 1. INTRODUCTION

In the last decade there has been a significant growth of microelectronics and magnetic sensors. In order to fulfill the requirements of faster, higher performance, more compact and lower energy consumption devices, the exploration of advanced materials with novel electronic properties are needed. Two kinds of material are outstanding candidates. One is magnetoelectric multiferroic materials because of its coupling of electric and magnetic properties. Another one is topological insulator which is known as a quantum material with ultrahigh conductivity on the surface while insulating in the bulk. In this chapter, I will not only introduce background of these two materials but also demonstrate the critical problem in their devices applications and my objectives regarding to the problem.

1.1 Magnetic Sensors and Material Aspect Consideration

Magnetic sensors are variegated in shapes, sizes and types according to the different physical nature they make use of [1]. However, they share the same feature which acts like a transducer that converts a magnetic field into an electrical signal. The first sensor-like device using magnetic field can be traced back to compass which invented by Chinese over 2000 years back. Afterwards, the long and complex evolution of magnetic sensors begins to the modern days. People never stops exploring various kinds of magnetic sensors challenging our imagination and productivity. Nowadays, most common types of magnetic sensing include Hall effect sensor, anisotropic magnetoresistance (AMR) sensor, giant magnetoresistance (GMR) sensor, magneto-optical sensor, resonance magnetometers, SQUID, magnetic tunnel junction, magnetoelectric sensor and spin valve-based sensor.

The present thesis focus on magnetic sensors based on a newly discovered quantum material – topological insulators (TIs) and their physical principles, materials, designs and performance. The following parts will introduce the background.

1.2 Hall Effect, Quantum Hall Effect and Quantum Spin Hall Effect

1.2.1 Hall effect

Hall effect is a transverse voltage generated in a conductor or semiconductor by the charge carrier moving in the magnetic field perpendicular to the plane. It was discovered by Edwin Hall in 1879 at the University of Baltimore [2]. A simple-geometry plate-like Hall device can be used to demonstrate Hall effect as shown in Figure1.1. A bias current I is supplied to the plate via two of the contacts. The other two sense contacts are placed at two sides perpendicular to the current contact. When a perpendicular magnetic field is applied to the device, charge carriers experience Lorentz force.

$$\vec{F} = q\vec{E} + q\vec{v} \times \vec{B}$$

q is the point charge, $\vec{E}$ is electric field, v is driven velocity, $\vec{B}$ is magnetic field

In the steady state condition where charges are not moving in y-axis direction because the magnetic force is cancelled by a y-axis electrical force due to charge built up. A voltage generated called Hall voltage.

$$E_{\mathrm{y}} - v_{\mathrm{x}} B_{\mathrm{z}} = 0$$

Apply the relations: $v_{\mathrm{x}} = \frac{I}{nabq}$ and $E_{\mathrm{y}} = \frac{V_H}{a}$, we get Hall voltage ($V_H$):

$$V_H = \frac{IB_{\mathrm{z}}}{nbq}$$

$$R_H = \frac{E_y}{B_z j_x} = \frac{1}{n|q|}$$

Hall coefficient is defined by the above equation. To use Hall effect as a sensing technology, the Hall voltage can be used to carry the information of magnetic induction $\vec{B}$. Thus, it can be used as a magnetic sensor. What's more, from the measured Hall voltage, we may deduce some important properties of the material. In this case the Hall device is applied as a means of characterizing material. The sensor application of Hall effect devices became important with the development of semiconductor technology.

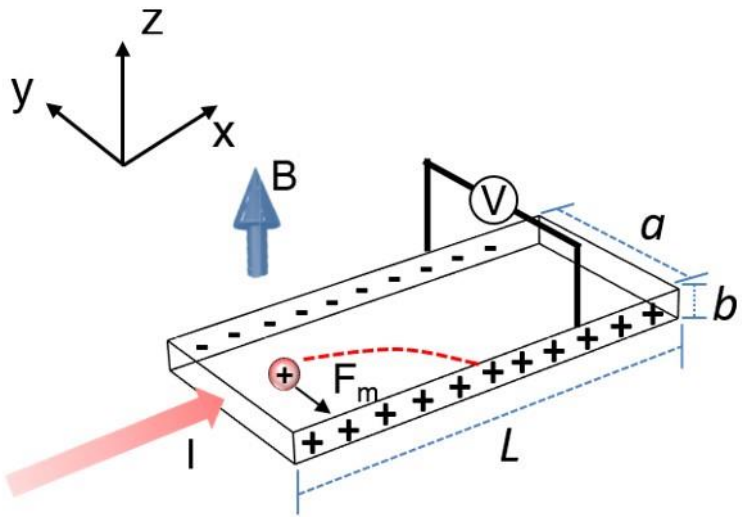

Figure 1.1 Simple plate model to demonstrate Hall effect.

The Hall effect also raises a question on the behavior of charged particles in a magnetic field. As we already know that, the Lorenz force drives the charged particles away from their ejection direction. If the magnetic field induced Lorenz force is large enough, the charged particles can move in circles called cyclotron. Take electrons with charge *e* and mass *m* for example,

$$\vec{F} = m\frac{d\vec{v}}{dt} = -e\vec{v} \times \vec{B}$$

When magnetic field points in the z direction, $\vec{B}$ = (0, 0, B), assume the particle only moves in the transverse plane, so $\vec{v}$ = (v_x, v_y, 0) = $(\dot{x}, \dot{y}, 0)$, solve the above two coupled differential equations,

$$m\ddot{x} = -e\dot{y}B \text{ and } m\ddot{y} = e\dot{x}B$$

we can get the general solution is

$$x(t) = X - Rsin(\omega_B t + \varphi) \text{ and } y(t) = Y + Rcos(\omega_B t + \varphi)$$

This indicates the particle moves in an anti-clockwise direction when going through the –z axis direction with center at (X, Y), the radius R and phase φ are all arbitrary. But circling frequency is fixed at $\omega_B = \frac{eB}{m}$, the cyclotron frequency. We further consider the electric field $\vec{E}$ which accelerates the charges and the resistance term which shows the charge cannot accelerate forever. The equation of a charged particle in magnetic field can be modified into

$$m\frac{d\vec{v}}{dt} = -e\vec{v} \times \vec{B} - e\vec{E} - \frac{m\vec{v}}{\tau}$$

in which $\frac{mv}{\tau}$ is the friction term that can represent electron scattered by impurities. This equation is the simplest model of charge transport called the Drude model. It assumes that electrons in solids is pinballs that bounding between the environment (ions) and the boundary. And there is no interaction between electron-electron and electron-lattice. The solution of the above equation at $\frac{dv}{dt} = 0$,

$$e\vec{v} \times \vec{B} + \frac{m\vec{v}}{\tau} = -e\vec{E}$$

The current density $\vec{J} = -ne\vec{v}$, where n is the density of charge carriers. The above equation becomes

$$\begin{pmatrix} 1 & \omega_B\tau \\ -\omega_B\tau & 1 \end{pmatrix}\begin{pmatrix} J_x \\ J_y \end{pmatrix} = \frac{e^2 n\tau}{m}\begin{pmatrix} E_x \\ E_y \end{pmatrix}$$

As we know J = σE. In the presence of a magnetic field σ becomes a matrix as conductivity tensor.

$$\sigma = \begin{pmatrix} \sigma_{xx} & \sigma_{xy} \\ -\sigma_{xy} & \sigma_{xx} \end{pmatrix}$$

Then we get the explicit expression for conductivity,

$$\sigma = \sigma_0 \frac{1}{1 + (\omega_B\tau)^2}\begin{pmatrix} 1 & -\omega_B\tau \\ w_B\tau & 1 \end{pmatrix}$$

in which, $\sigma_0 = \frac{e^2 n\tau}{m}$ is the conductivity without a magnetic field. The resistivity is the inverse of the conductivity from its definition. Therefore, regarding to the conductivity matrices, the resistivity matrices are,

$$\rho = \sigma^{-1} = \begin{pmatrix} \rho_{xx} & \rho_{xy} \\ -\rho_{xy} & \rho_{xx} \end{pmatrix}$$

From the above Drude model, we get

$$\rho = \frac{1}{\sigma_0}\begin{pmatrix} 1 & \omega_B\tau \\ -\omega_B\tau & 1 \end{pmatrix}$$

The diagonal terms are from longitudinal resistivity $\rho_{xx} = \frac{1}{\sigma_0} = \frac{m}{e^2 n\tau}$ The off-diagonal terms in the matrix stems from Hall effect $\rho_{xy} = \frac{w_B\tau}{\sigma_0} = \frac{B}{ne}$. During the experiment, we measure the longitudinal resistance Longitudinal resistance $\mathrm{R}_{xx} = V_x/I$ and Transverse resistance $\mathrm{R}_{xy} = V_y/I$. Then we can get $\rho_{xx}, \rho_{xy}, n, \tau$. We will use these equations to derive the carrier mobility and conductivity in our results of topological insulators based Hall sensors in the following chapters.

1.2.2 Integer quantum Hall effect

The Hall effect has been found widespread application in magnetic field sensors and has led to a wealth of new phenomena, such as the integer quantum Hall effect [3]. The integer quantized Hall effect also discovered 100 years later in 1980 at low temperatures and strong magnetic fields [4]. The history of the quantum Hall effect is intimately related to technological advances in the fabrication of the metal-oxide-semiconductor (MOS) structure. At that time, researchers began to explore the electron properties which can enhance the performance of MOS devices. The motion of electrons in the thin layer of silicon and silicon oxide interface is expected to be confined into two dimension. To increase the carrier mobility, researchers were seeking for the answer about which scattering process during the charge transport dominate the motion.

As postulated by Schrieffer in 1957, if the wavelength of the charge carrier is comparable to the distance from interface to the classical turning point, they cannot behave classically in the direction perpendicular to the interface. However, because of the scattering process of carriers with impurities, the quantized behavior of carrier is expected but not observe until researcher's decrease experiment temperature to liquid helium and applied a strong magnetic field (19.8T). A review article published by T. Ando, A. Fowler and F. Stern in 1982 [5] summarizes the discovery process of QHE. Von Klitzing was awarded the 1985 Nobel prize for discovering integer quantum Hall effect. As shown in the original experimental curve of QHE in Figure 1.2, the Hall resistance appears plateaus together with vanishing longitudinal resistance is observed. This is because the localized electrons and appearance of Landau level. The Hall resistance is the integer multiples of h/e^2 when Fermi level is in between Landau

levels. Similar to the problem of "particle in a box", electrons are confined in a thin layer of few nanomaters plan so the energies are quantized:

$$\mathrm{E}_{0,N} = \mathrm{E}_0 + \left(N + \frac{1}{2}\right)\hbar\omega_B \quad (N = 0,1,2 \ldots)$$

where $\hbar\omega_B = \hbar eB/m$ is the cyclotron energy..

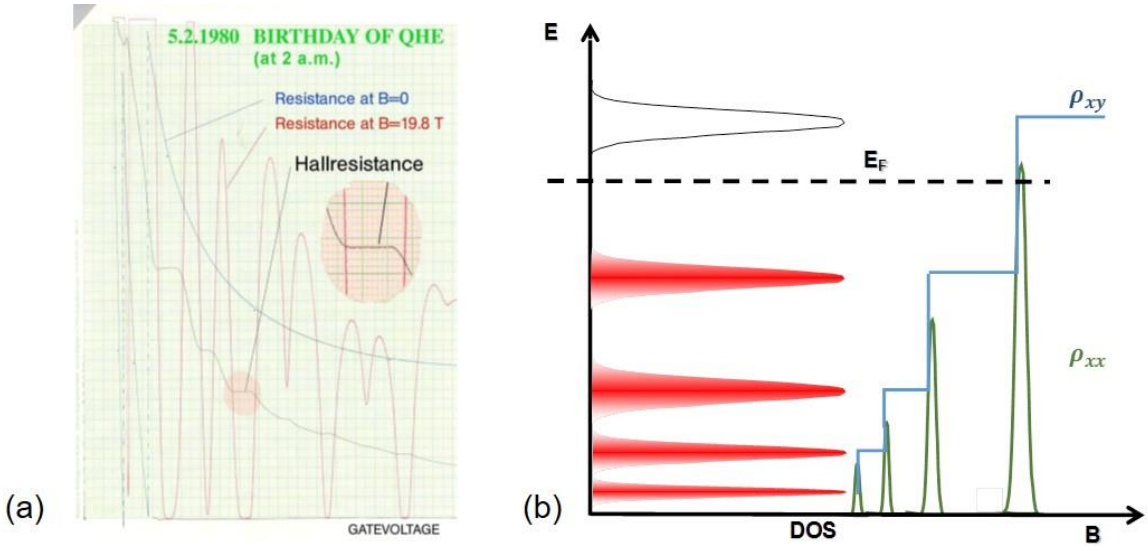

Figure 1.2 The discovery of quantum Hall effect in a silicon MOSFET at liquid helium temperature [6]. The quantized plateau on Hall resistance and vanish of longitudinal resistance were observed.

Ando in his review paper on topological insulator materials [7] descriped that the quantum Hall systems can be considered to be the first topological insulator because the Landau quantization causing the energy gap and Fermi level are located in the gap, which is a situation akin to an insulator.

1.2.3 Quantum spin Hall effect

The research on quantum spin Hall effect(QSHE) is motivated both by the quest for spin based electronic devices and by its scientific impact in condense matter physics. It is proposed that quantum spintronic devices process information and storage memories with lower power consumption compared to the logic devices based on charge current [8]. Quantum spin Hall effect is the quantized version of spin Hall effect which theoretically proposed in 1970s. In analogy to Hall effect, a transverse spin current in response to longitudinal electric field for spin Hall effect. The first evidence for the spin Hall effect is observation of spin-up and spin-down electrons are deflected to opposite side of a semiconductor which resulting the spin current with no net charge current, perpendicular to the direction of the electric field in the absence of applied magnetic fields by Kato *et al*. in 2004 [3]. This experiment evidence of spin Hall effect boosts the research on manipulating electrons spins in non-magnetic semiconductors.

Similar to QHE happens in confined electrons in two dimensions, researchers soon predicted that when spin-polarized electrons flow opposite directions using the edge state, quantized spin Hall effect can be observed. Kane and Mele provided a theoretical model system composed of a graphene model with spin-orbital coupling (SOC) to achieve the QSHE [9]. However, the SOC in graphene is very weak so it is difficult to obtain experimental evidence of QSHE in graphene. Though QSHE in graphene systems is not observed, it was soon predicted that it could be achieved by 2D quantum well structure by Bernevig, Hughes, and Zhang (BHZ) [10]. This theoretical breakthrough finally leads to the experimental observation of QSHE and the birth of topological insulators.

In 2007, Konig et al observed the quantization of magneto-conductivity in zero magnetic field in CdTe/HgTe/CdTe quantum well [11]. This was defined as 2D topological insulator. Soon after the discovery, theorists extended the concept of topological insulators into 3D systems.

1.3 Topological Insulators

1.3.1 Band theory, topology of solids and symmetries

When "topological insulator" appears on the paper, our first impression is we know insulator since we were in our science class. "Topology" is a Greek word define the properties of space that are preserved under continuous deformation. For example, a mug with a handle on the side can be continuously deformed into a doughnut in principle without tearing and gluing because both have one hole. However, a basketball cannot transfer into a doughnut without cutting it because the ball shape has no hole. In this sense, the doughnut and mug have the same topology whereas the ball has a different topology from them.

In order to explain the concept of topological insulator, some knowledge in quantum physics need to introduce first. In quantum mechanical, if a system is confined spatially, they could only have certain discrete value of energy. These values are defined as energy levels. The lowest possible energy level of a system can stay is called ground state. If in some circumstance, such as heating the system, it goes to higher energy level, we said the system is excited. It is on excited state. How could we know how many energy states and their value in a system? This can be achieved by using Schrodinger equation with a Hamiltonian operator on a wave function as an eigenfunction. The eigenvalues are the energy level values. The Hamiltonian is the total energy of a system including kinetic energy and potential energy. For

any system contain electrons in atoms, ions or molecules, we can calculate the energy levels, which are the possible state the electron can stay or occupied. However, this does not mean, the electron occupies all the energy states. Besides, there is also a possibility that an energy range in a solid where no electron energy state can exist, energy gap. Therefore, the "insulator" in terms of the band theory are all gapped systems, where the Hamiltonian $\vec{H}$ displays an energy gap between the ground state and the first excited state. For example, in diamond crystal, the electrons fully occupy energy states and the next available energy state is far away. The energy gap prevents the electron jump to the higher state without external excitation at room temperature. Therefore, diamond is an insulator which has a gaped Hamiltonian.

Another important concept in condense matter physics is symmetry. It is defined as the system is not change to any of the transformations such as reflection, rotation or scaling. Each of this transformation correlates to a symmetry operation. In group theory, there are unitary symmetries and antiunitary symmetries. For the former one, the symmetry operation commutes with the Hamiltonian so that the Hamiltonian can be block-diagonalized into irreducible unit. One can just study the Hamiltonian within the unit. These symmetries include translation, rotation and scaling. However, systems with antiunitary symmetries cannot be block diagonalization into small units. These includes time-reversal symmetry, particle hole symmetry and chiral symmetry.

When a set of symmetries is specified, different Hamiltonians $\overrightarrow{H'}$ are grouped under the same equivalence class to which $\vec{H}$ may be deformed without closing of energy gap and no violations of the specified symmetries. The ordinary insulators of which the Hamiltonian can deformed continuously to each other without closing of energy gap share the same topology.

However, topological insulators are insulators that do not share the same topology with ordinary insulators [12].

Although for topological insulators, the Hamiltonian also displays an energy gap between the occupied and empty energy states but it is fundamentally modified due to the spin-orbit interaction. That is, the interaction between electrons' spin and orbital angular momentum. This is a relativistic effect that happened in all chemical atoms. But in material compose heavy elements auch as Bi or Sb, the spin-orbital interaction is stronger and crucial. The interaction is so strong that the energy gap is inverted, the states should have higher energy appears below the gap. This twist in the order of electronic states, like the twist in the Mobius strips, comparing to the ordinary insulator band gap like a close stripe (Figure 1.3).

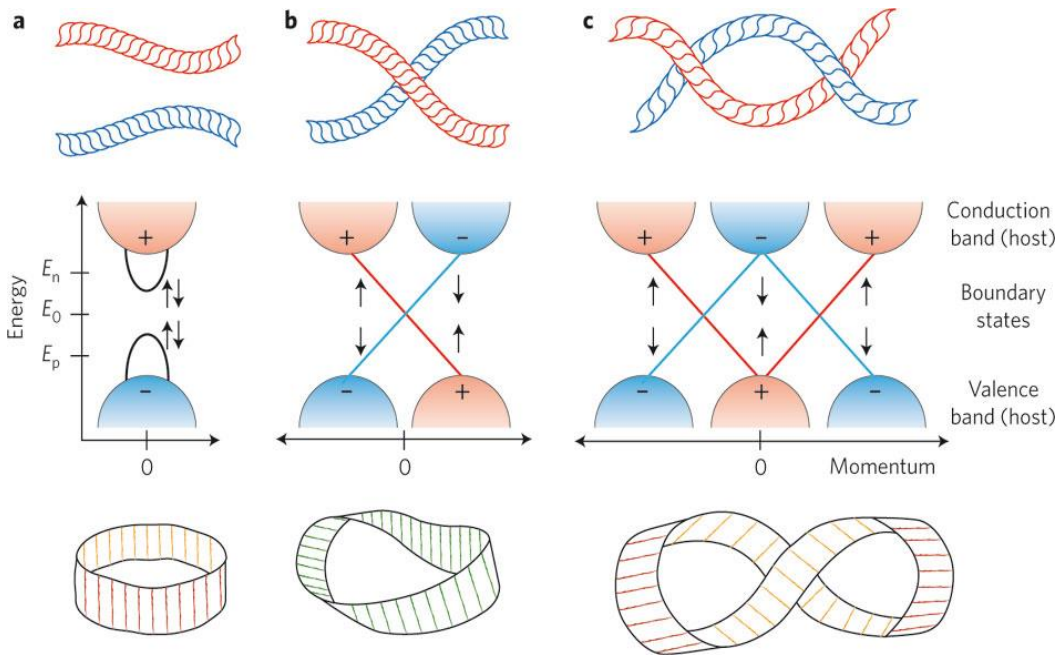

Figure 1.3 Band structure of toplogical insulators and other insulators [13].

The topology of this two gaped system is distinct. Also, as introduced above the energy states are discrete in gaped systems, as long as the energy gap remains open, the topology cannot change [13]. Thinking about a situation that a topological insulator physically contact

to an ordinary insulator like vacuum or air. In order to change topology across the interface between a topological insulator and an ordinary insulator, the energy gap must close and reopen [13]. Similar to the process of opening the Mobius strips and form a close stripe, one need to cut the Mobius stripe and make a half-twist to flatten then joining the ends of the strip to form a close loop. This gap closing at interface is where the surface state of 3D TIs and edge state of 2D TIs comes from (Figure 1.4).

The principle for the occurrence of gapless interface states is called bulk-boundary correspondence in topological phases [4]. Most of the unique properties of TIs come from this peculiar surface/edge states. The most profound one is the highly metallic conducting surface/edges (ultrahigh electron mobility on the surfaces/edges), which don't exist in ordinary insulators.

Moreover, these metallic surfaces/edges are fundamental different from the ordinary conductor or other 2D conducting surfaces. The electrons on these surfaces/edges not only have ultrahigh mobility but also immune to non-magnetic impurities [14]. These surface/edge electrons cannot be backscattered during propagation because the above mentioned strong spin-orbital coupling. For these electrons, the momentum and spin are 90 degrees locking to each other. Figure 1.4 shows the electron propagation on the edge/surface of 2D/3D TIs. The spin up electrons travel in one direction while spin down in a opposite direction. If the electron is backscattered, they will travel to opposite direction because of spin-momentum locking, the spin at same time need to flip in opposite direction. However, if there is nothing like magnetic field or magnetic impurities to help flip the spin, the electrons cannot travel backwards [6]. Therefore, the surface electrons propagate with no resistance in theory.

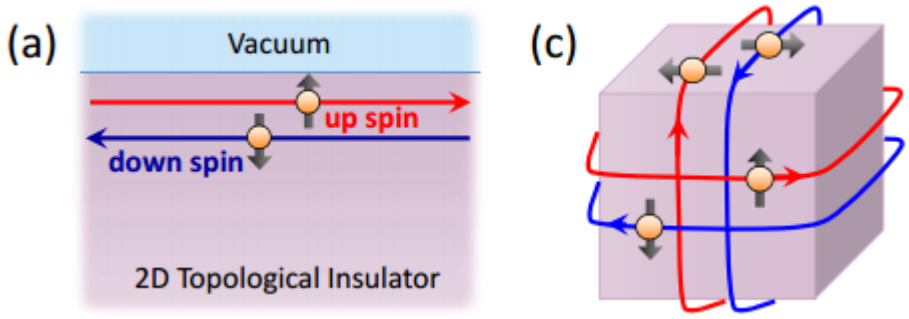

Figure 1.4 Edge and surface states of topological insulators [7].

Topological insulators were defined in the process of searching for the Z_2 topology insulators [14]. It was first discoved in CdTe/HgTe/CdTe quantum well in 2007 by low temparture transport measurement, then in $Bi_{1-x}Sb_x$ alloy 3D system in 2008 by angle-resolved photoemission spectroscopy (ARPES). In this work, we only focus on 3D topological systems.

To give a brief summary of topological insulators, it is a recent discovered kind of quantum material which possesses a ultra-high carrier mobility at surface while insulating in the bulk [15]. The exotic metallic surface behavior of TI is supported by the unique bulk band structure where the bulk conduction band and bulk valence band are inverted at a certain point. The band inversion is caused by SOC. The extreme strong coupling of electron's spin and orbit in TI leads to the spin and momentum locking in the material and eventually leads to band inversion and a linear dispersion of surface states. Though TI originate from its unique bulk insulators, its surface state which support localized metallic states with special properties such as spin polarization.

The surface states of topological insulators are characterized by an odd number of linearly dispersed Dirac cones, meaning that the bands exhibit very small curvature and therefore the surface carriers have little effective mass. Moreover, these conducting surfaces states are topologically protected since the directions of spin and momentum are locked due to

a strong spin-orbit coupling. The strong SOC ensures that the spin state of a surface carrier can be determined from the direction of the wave vector alone and that there is only one state for each point on the surface bands.

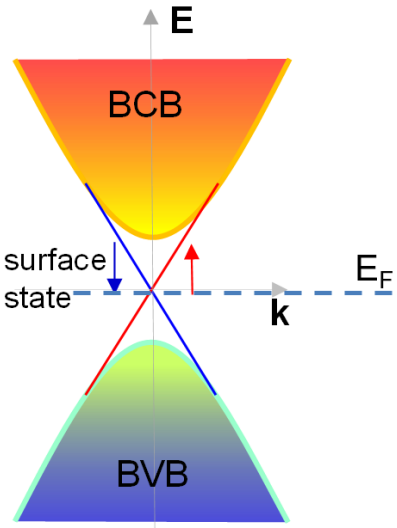

Figure 1.5. Idealized band structure of topological insulators.

Due to this topological origin of the surface states, the gapless surface dispersion is robust and can keep its form (without the opening of a surface band gap) even in the presence of perturbations such as defects, impurities, and other perturbing influences in their environment that do not break time reversal symmetry (TRS) [14]. The topological robustness and the SOC act together to suppress backscattering of surface carriers, allowing for highly conductive surface channels. Recently, by doping copper in bismuth selenide TI, it's possible to make the topologically ordered electrons superconducting, dropping electrical resistance in the surface states to zero. Thus, the topological insulator should lead to the advancement of future low-power electronics.

1.3.2 Ferromagentism in topological insulators and anomalous Hall effect

The exotic surface state of TIs protected by TRS can be broken by certain perturbations, such as the application of a magnetic field out of plane of the surface or elemental doping that leads to magnetic ordering out of plane. As shown in Figure 1.6, the breaking of TRS in the system results in opening a surface energy gap at the Dirac point, separating the energy states of spin-up carriers from spin-down upon the surface.

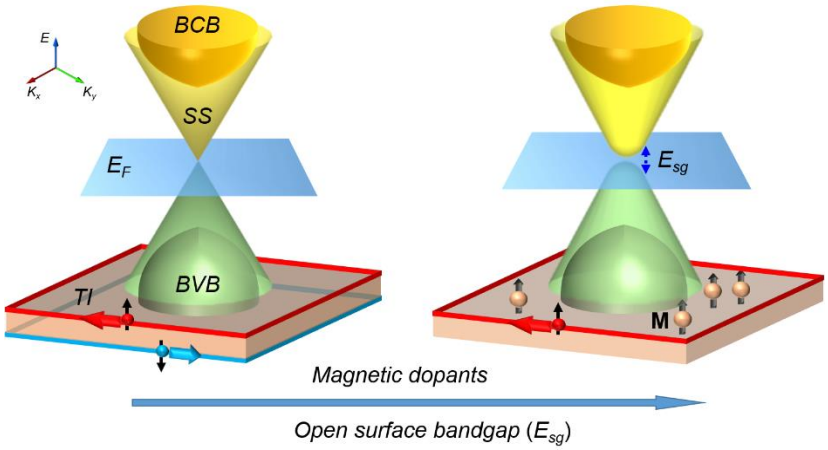

Figure 1.6 Ideal 3D topological insulator band structure and ferromagnetic topological insulators band structure.

This phenomenon can be understood by considering a simple Hamiltonian for the surface states without turbulence from magnetic field as $\vec{H}_0 = \vec{v}_F(k_x\sigma_y - k_y\sigma_x)$ where $\vec{v}_F$ is the Fermi velocity, $\vec{k} = (k_x; k_y)$ is the wave vector and σ_x and σ_y are Pauli matrices. The energy of electrons are $E = \pm v_F k$. When magnetic elements are doped in topological insulators, with inducing the ferromagnetic phases when placing the TIs at low temperature environment. With magnetization direction normal to the surface, the Hamiltonian of the system changes to $\vec{H} = \vec{H}_0 + JM\sigma_z/2$ [16], where the magnetization is $\vec{M}=(0, 0, M)$ and J the dimensionless exchange coefficient. To solve the eigenfunction, energy eigenvalues of electrons are given by $E_k = \pm[(v_F$

$k)^2 + (JM/2)^2]^{1/2}$, where $k^2=k_x^2+k_y^2$, which describes surface bands separated by an energy gap of JM. This can be compared directly with the well-known expression for the dispersion of a free relativistic particle from Dirac equation, $E_p = \pm[(cp)^2 + (mc^2)^2]^{1/2}$ where c is the speed of light, m is the particle mass and p is the momentum. Through comparison of the two dispersion relations, the dispersion characteristics of surface carriers in TIs are very similar to free relativistic particles, with the magnetization and exchange coupling accounting for the energy gap instead of the particle mass. It is in this situation, with a surface energy gap, that topological insulators find many of their interesting properties such as the anomalous quantum Hall effect (QAHE) and its quantized conductivity [17-20]. The anomalous Hall effect in a ferromagnet can be induced by spontaneous magnetization [21].

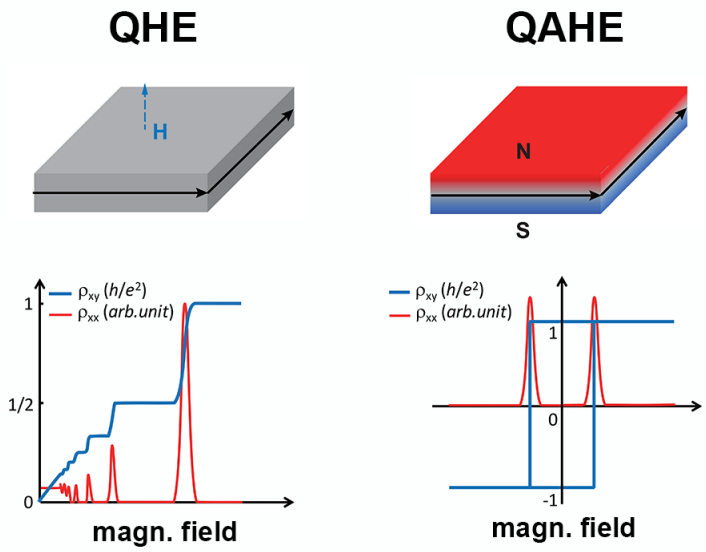

Figure 1.7 Schematic picture of quantum Hall effect and quantum anomalous Hall effect [22]

As introduced above, the discover of quantum spin Hall effect leads to the development of TIs. Researchers also recognized that QSHE in nonmagnetic systems is funmanetally related to the anomalous Hall effect in ferromagnetic systems [21]. Through suppressing one of the

spin channels in the QSH system by inducing ferromagnetism, it will naturally leads to the QAHE [23]. Different from QHE, QAHE can happen without a external magnetic field. The combination of spontaneous magnetization in ferromagnetic TIs and strong spin-orbital coupling could take over the role of external magnetic field in QHE. QAHE was first observed in Cr-doped Bi_2Te_3 in 2013 [24] where the Hall resistance shows h/e^2 as magnetic field drops to zero (Figure 1.7). One can observed that Hall resistance jumps from $-1h/e^2$ to $1h/e^2$ directly when applied magnetic field and stay at $1h/e^2$ when remove the field in QAHE. This is different from the QHE in which Hall resistance reach to $1h/e^2$ step by step as magnetic field increasing.

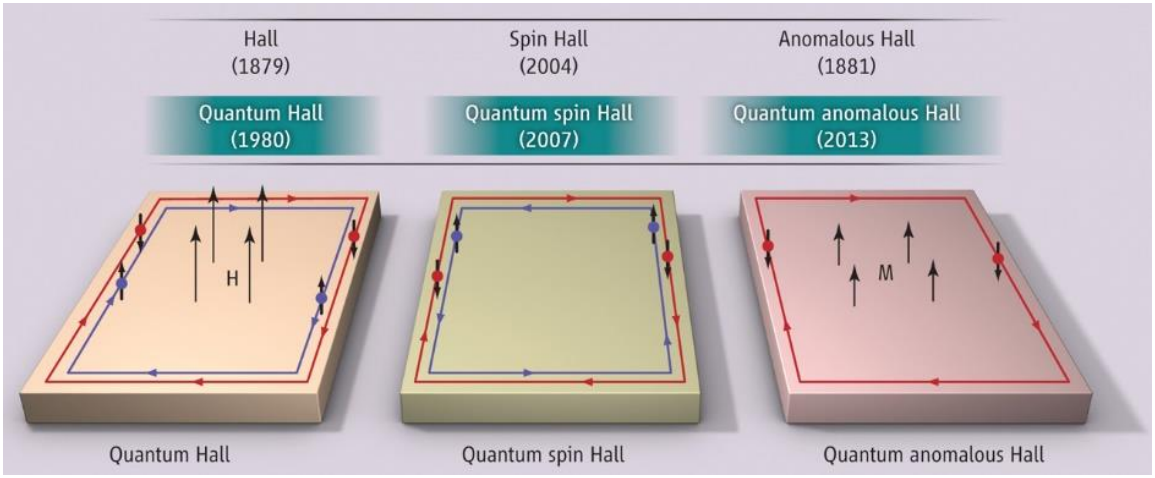

Figure 1.8 Quantum Hall trio [23].

The discovery of QAHE completes the Hall effect family. Figure 1.8 shows the Hall effect family since the first Hall effect been discovered by Edwin Hall in 1897. The year of each discovery lists in the parentheses. For all three quantum Hall effect, electrons flow on the edges whereas the bulk of the systems keep insulating. When there is a net flow of electrons for Hall resistance measurements, the extra electrons only occupy the left edge channels regardless of spin direction in QHE, spin with opposite directions occupy the opposite sides

of edges in QSHE, and only spin-down electrons flow through the left edge in QAHE [23]. Besides, QHE requires the external magnetic field in 2D semiconductor or conductor. QSHE happens in nonmagnetic thin films. QAHE happens in ferromagnetic TIs.

The lossless edge channel and the exact quantization of QAHE not only spur the research of TIs but also could be applied in many fields including spintronic devices and quantized resistance can be used as a resistance standard [23]. In this work, we explore the sensor applications of TIs for ultrahigh sensivity sensors.

1.3.3 3D topological insulators

Although $Bi_{1-x}Sb_x$ alloys were the first 3D TI material discovered by Fu and Kane [25] but it is not suitable for detailed study of topological surface state and the further application due to its complicated surface state [26, 27]. Some theoretical prediction and first-principle calculations [28, 29] of $Bi_{1-x}Sb_x$ surface are not consistent with the experimental results. The understanding is still in an incomplete state for this system [7]. Therefore, Zhang *et al*. theoretically predicted that Bi_2Se_3, Bi_2Te_3 and Sb_2Te_3 should be 3D TIs using a low-energy effective model. Soon after the prediction, the experimental observation of surface states of Bi_2Se_3 [30], Bi_2Te_3 [31] and Sb_2Te_3 [32] were reported. These materials are all tetradymite structure which can be defined as five layer of atoms stacked in X-Y-X-Y-X form in covalence bond [7]. These five atomic layers form one quintuple layer which is about 1nm thick. The interaction between quintuple layers is via van der Waals force. This provides a change to deposite TI thin films on any substrates by van der Waals epitaxy which requires less on lattice matching. This will be discussed in next chapter. Crystal structure of 3D TI systems and quintuple layer are shown in Figure 1.9.

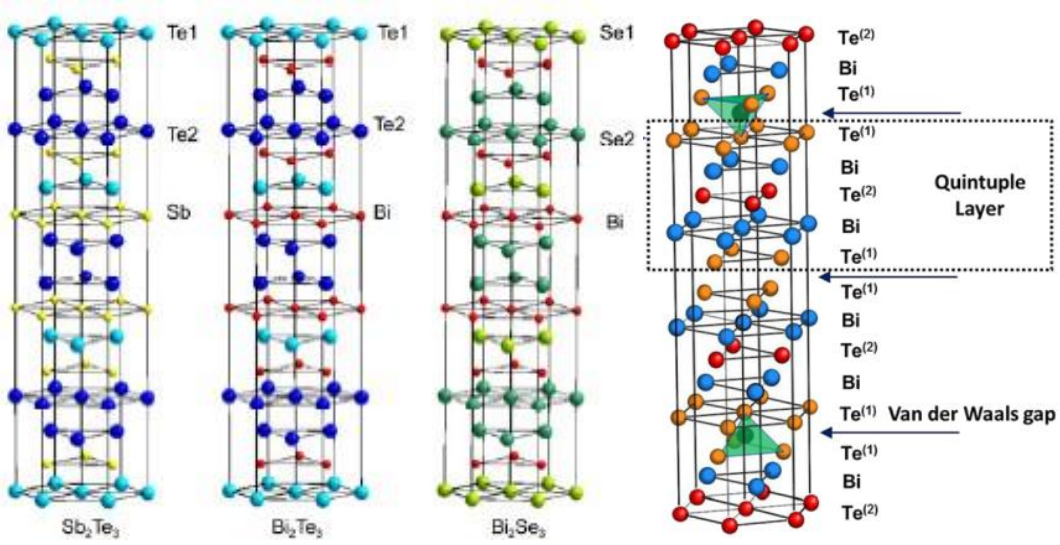

Figure 1.9 Crystal structure and quintuple layer [33].

1.4 Topological Insulator Based Devices

1.4.1 Proposed devices based on topological insulator

The exotic surface state of TIs can be broken by certain perturbations, such as the application of a magnetic field out of plane or elemental doping that leads to magnetic ordering out of plane. This finally leads to anumolous Hall effect as introduced above. The surface band gap turning from close to open provide an opportunity to make a switching device that can be used in modern electronics and spintronics.

We proposed a high resistance on/off ratio, smaller size and less power consumption switches based on TIs. Figure1.10 (a) shows the central idea of the proposal: The $R_{on/off}$ ratio of the current switch devices is controlled by manipulating the surface band gap of topological insulator through magnetization direction of the magnetoelectric oxide layer. And the magnetization ($\vec{M}$) direction in the magnetoelectric oxide can be controlled via an electric field applied through the metal gate. Orientating $\vec{M}$ perpendicular to the TI surface leads to high

resistance state, whereas the low resistance state is restored when $\vec{M}$ is parallel with the TI surface. Moreover, as Figure 1.10 (b) shows, the energy consuming of topological insulator based current switch devices (TI), which is proportional to their electric resistivity, is far below other high magentoresistance devices based on magnetic tunneling junction (MTJ), ferromagnetic Mott insulators (FFET), and giant magnetoresistance (GMR).

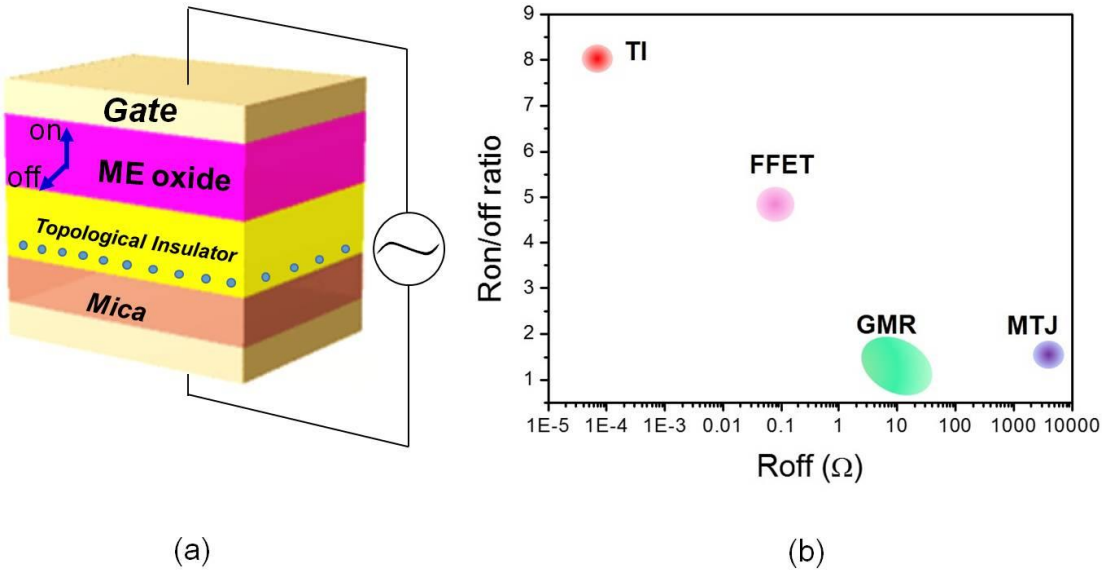

Figure 1.10 (a) Proposed current switch devices. Orientating $\vec{M}$ perpendicular to the TI surface leads to high resistance state, whereas the low resistance state is restored when M is parallel with the TI surface. (b) Comparison on $R_{on/off}$ ratio and electricresistivity between TI-based current switch devices and other high magnetoresistance materials.

The TI-based switching functioning based on the proximity effect of TI and ferromagnets as shown in Figure 1.11(a). The device consists of a gate metal layer, magnetoelectric oxide (EM oxide) layers, a thin topological insulator layer and a magnetic doped topological insulator buffer layer on mica substrate. The magnetic doped topological insulator buffer layer can break time-reversal symmetry of the bottom surface while keeping

the top surface active. The net magnetization ($\vec{M}$) will generate in ferromagnetic thin layer in the magnetoelectric oxide (for example, magnetoelectric multiferroic $CoFe_2O_4/BaTiO_3$ heterostructure). Its direction with respect to z axis (Θ) can be manipulated via the ferroelectric thin layer in ME oxide through the metal gate. Figure1.11 (c) shows the magnetization direction change from (Θ=0˚to 90˚) as the gate voltage increase/decrease . As Figure 1.11(b) shows, orientating $\vec{M}$ perpendicular to the TI surface (Θ=90˚) leads to a bandgap, whereas the bandgap vanishes when $\vec{M}$ is parallel to the TI surface(Θ=0˚). Therefore the current switch device can be operated when the magnetization direction is varied by the external electrical field. These two states will enable the device to change from insulator to conductor reversiably when exposed to a small gate voltage. The band diagram of the two states of switch are describe in Figure 1.11(d). One can see that when the gate voltage increase to certain threshold, the current through source to drain will jump because of the surface bandgap and its relative position to Fermi level. By further exploring the tunneling behavior in scaled devices with intermediate channel lengths, it is expected to substantially increase the Ron/off ratios in which the device enters a critical regime between diffusive (low bias) and ballistic (high bias) transort — A significant change in the channel mobility is expected to result in high $R_{on/off}$ ratios, which is a highly sought-after feature for low-power electronics.

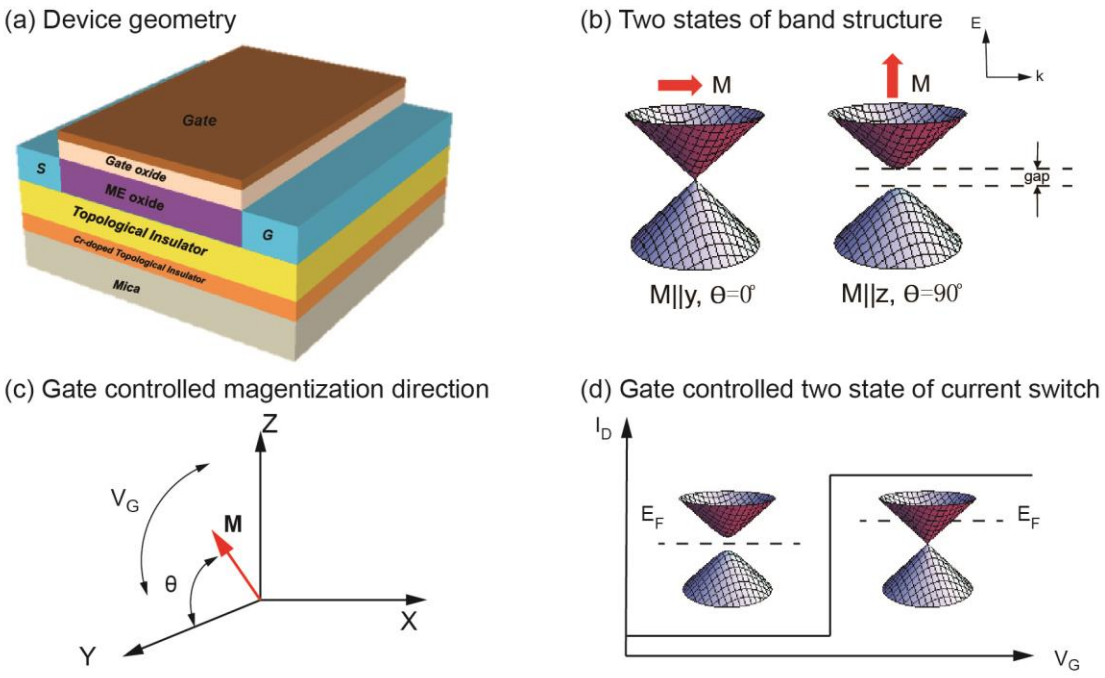

Figure 1.11 A proposed current switch device based on the manipulation of surface states. The magnetization direction of ferromagnetic oxide can be adjusted via an electrical field applied on the metal gate (b). When θ is 90°, surface gap is open, resulting in massive Fermions with low mobility (a); however, when θ is 0°, surface remains gapless, leading to massless Fermions with high mobility (c). By controlling the magnetization directions, the switch could be operated with Ron/off states (d).

The device proposed above requires several combination of several layers of material including not only TIs but also magnetoelectric multiferroics. We will introduce the concept of magnetoelectric multiferroics below.

The coupling of electric and magnetic phenomena is not a novel idea since James Clerk Maxwell already established the dynamic coupling between these two in his electromagnetic equations. Electromagnetism originated from the electrodynamics, namely, time-dependent magnetic field and electric field are coupled, whereas the electrostatic field and magnetostatic field are independent of each other. However, magnetoelectric (ME) effect exits even in static

field that static electric field induces magnetization and a static magnetic field gives rise to electric polarization. This property promises the ME device to consume less energy since the thermal loss associating the electron motion in the AC field can be reduced [34].

The present section begins with an introduction to the physics of magnetoelectric coupling, followed by the material consideration of magnetoelectric multiferroics and the origin of magnetoelectric composites.

1.4.1 Background of magnetoelectric and multiferroic

The idea of ME can traced back to Pierrer Curie in 19th century who was the first to state that molecules are magnetized by applying an electric field and electrized by a magnetic field [35]. The coupling between the ferromagnetic order and ferroelectric order in a single phase has been described by many researchers [36-38]. As introduced above, the coupling can be described by Landau theory by writing the free energy G of the system in terms of magnetic field ($\vec{H}$) and electric field ($\vec{E}$). When we consider the temperature induced ferroic phase transition in the couple the system, the spontaneous polarization ($\vec{P_s}$) and spontaneous magnetization ($\vec{M_s}$) will also be accounted in the free energy formula. Therefore, the applying the Einstein summation, the tensor notation of the free energy can be expressed as follows [36]

$$-G(\vec{E},\vec{H}) = \frac{1}{2}\varepsilon_0\varepsilon_{ij}E_iE_j + \frac{1}{2}\mu_0\mu_{ij}H_iH_j + \alpha_{ij}E_iH_j + \frac{\beta_{ijk}}{2}E_iH_jH_k + \cdots$$

The first term on the right hand side of the equation describes the contribution of electrical response to an electric field, where ε_0 and ε_{ij} are permeability in free space and in the material respectively. The second term is the magnetic response of a magnetic field which is equivalent to the first term. The third term described the linear coupling of magnetic ordering and electric ordering. $\alpha_{ij}$is the linear coupling coefficient and β_{ijk} is the higher-order coupling coefficient.

The coupling effect of ferromagnetic and ferroelectric can be established in the form of $P_i(H_j)$ *a*nd $M_i(E_j)$ by differentiating free energy with respect to $\vec{E}$ and $\vec{H}$ respectively. We can obtain：

$$-P_i = \frac{1}{2}\varepsilon_0\varepsilon_{ij}E_j + \alpha_{ij}H_j + \frac{\beta_{ijk}}{2}H_jH_k + \cdots$$

Set $E_j = 0$, we get:

$$-P_i = \alpha_{ij}H_j + \frac{\beta_{ijk}}{2}H_jH_k + \cdots$$

Similarly, differentiating free energy with respect to H and set $H_j = 0$, we obtain:

$$-M_i = \alpha_{ji}E_j + \frac{\beta_{jik}}{2}E_jE_k + \cdots$$

According the equation above, the coupling coefficient becomes a critical value to describe whether it is a strong coupling or a weak coupling between the magnetic property and electric property [39]. The linear magnetoelectric effect in their book and proposed the model as followings:

$$P_i = \frac{\partial E_i}{\partial H_j}H_j$$

$$M_i = \frac{\partial H_j}{\partial E_i}E_\mathrm{j}$$

$\frac{\partial E_i}{\partial H_j}$ is the inverse ME effect coefficient.

After spontaneous magnetization and polarization simultaneous happened in a single phase compound discovered in nickel iodine boracites ($Ni_3B_2O_{13}I$) [40], lots of other bulk ceramic multiferroic materials have been explored. These bulk single phase multiferroic materials including $Bi(Fe,Mn)O_3$ [41-43], $ReMnO_3$ and the series of $ReMn_2O_5$ single crystals (Re = rare earth). $BiFeO_3$ is discovered which perhaps the only material that is both magnetic and a strong ferroelectric at room temperature [44]. It exhibits an antiferromagnetic behavior

with a relatively high Neel temperature at about 380 °C and a ferroelectric behavior with high Curie temperature (T_c = 810°C). Its weak ferromagnetism at room temperature is due to a residual moment from spin structure [45]. The existence of a spin cycloid averages out any linear magnetoelectric (ME) coupling between polarization and magnetization. However, the compound which has the ME properties are very few in nature because in general, the transition metal *d* electrons, which are essential for magnetism, reduce the tendency for off-center ferroelectric distortion. Consequently, an additional electronic or structural driving force must be present for ferromagnetism and ferroelectricity to occur simultaneously. The linear interaction can only exist under very restrictive crystal symmetry constraints, thus the number of crystals that are able to show it are rather limited. Also, their weak ME effect still hinder the application.

An alternative method in enhancement of ME effect is to introduce indirect coupling through strain between two materials such as ferroelectric material and ferromagnetic material [46]. This is a biquadratic coupling between polarization and magnetization placing no constraints on crystal symmetry and is thus allowed in all materials. This coupling is so far the most commonly exploited, and has the largest potential to commercially viable [47]. The biquadratic magnetoelectricity can be achieved and manipulated by strain as the intermediate step.

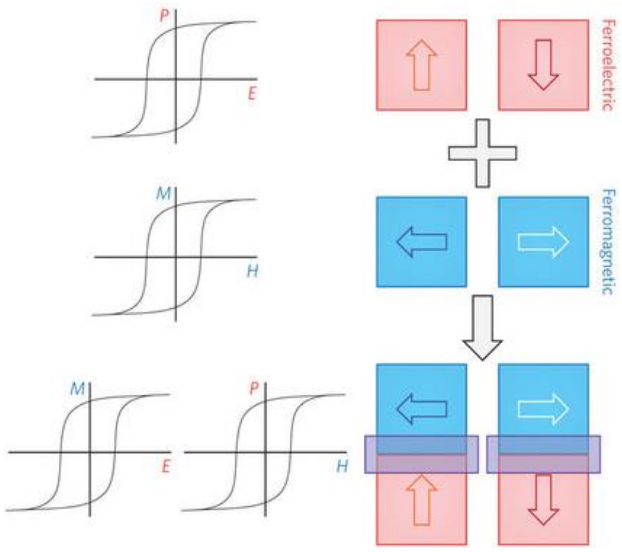

Figure 1.12 Magnetoelectric multiferroic composite design [48].

The ferroelectric/ferromagnetic composites enable the development of magnetoelectric materials with enhanced ME effect. This can be achieved by indirect coupling through the interfacial strain between the ferroelectric and ferromagnetic materials [46, 49-51] shown in Figure 1.12. Such strain mediated ME effect can be used to generate electric polarization in the ferroelectric component of the composite due to applied magnetic field in the ferromagnetic component or magnetization in the ferromagnetic component due to applied electric field in the ferromagnetic component. The property tensor $\frac{\partial E_i}{\partial H_j}$ can be given by the product of the proportionality tensor of the phases [52]:

$$\alpha_{ij} = \frac{\partial \lambda_{ij}}{\partial H_j} \frac{\partial E_i}{\partial \lambda_{ij}}$$

where $\frac{\partial \lambda_{ij}}{\partial H_j}$ is the magnetostriction derivative and $\frac{\partial E_i}{\partial \lambda_{ij}}$ is the change of the electric field with strain. Therefore, according to the equation above, for the engineering of materials with the desired properties, two types of composites can be proposed, those with product properties of

inverse magnetostrictive effect-electrostrictive phases and those with product properties of magetostrictive-pizoeletricity. For example, the ME effect, when a magnetic field is applied to a composite, the magnetic phase changes its shape magnetostrictively. The strain is then passed along to the piezoelectric phase, resulting in an electric polarization. Thus, the ME effect in composites is extrinsic, depending on the composite microstructure and coupling interaction across magnetic-piezoelectric interfaces [53].

1.5 Motivation and Objectives

Though TI has very unique properties as introduced above, there are still several critical challenges need to be addressed in order to utilize TI practically such as building electronic devices and magnetic sensors.

First challenge is to choosing proper syntheses method to fabricate TI materials with high quality: large area of thin films, low surface roughness, large terrace width, thickness controllable TIs. There are several ways of syntheses: bulk single crystals growth by Bridgman method or vapor transport; nanoribbons and nanoplates fabrication by gold-catalyzed vapor liquid solid (VLS) technique; and thin film growth by molecular beam epitaxy (MBE) or chemical vapor deposition (CVD). Though the single crystal of TIs is easy to grow, it is not easy to get large pieces when you cleave them. Usually the nano flakes can be made by exfoliation using Scoth tapes. Thin film deposition is the method I choose for my TI samples. Compared to single crystal growth, deposition method can give more controllability regarding to both the composition and thickness of samples. Also, with epitaxy growth, there are more flexibility to sysnthese more complex TI systems such doping or co-doping different elements. Besides, since the van der Waals gap between the quintuple layers, the lattice matching of

sample with substrate is not crucial in epitaxy which gives the possibility to deposite TIs on different kind of substrates to fullfill the need of different measurement requirements.

Second, most TI systems discovered nowadays are semiconductors in the bulk rather than insulators. The Fermi level lines at bulk conduction band or bulk valence band. Also, the Dirac cone is not within the bulk band gap for most TIs [Fig 13 (b)]. It is often difficult to obtain sufficiently bulk-insulating samples because of the unintentionally-doped Se or Te vacancies. Therefore, reducing bulk conductivity is crucial to achieve ultrahigh carrier mobility of surface state.

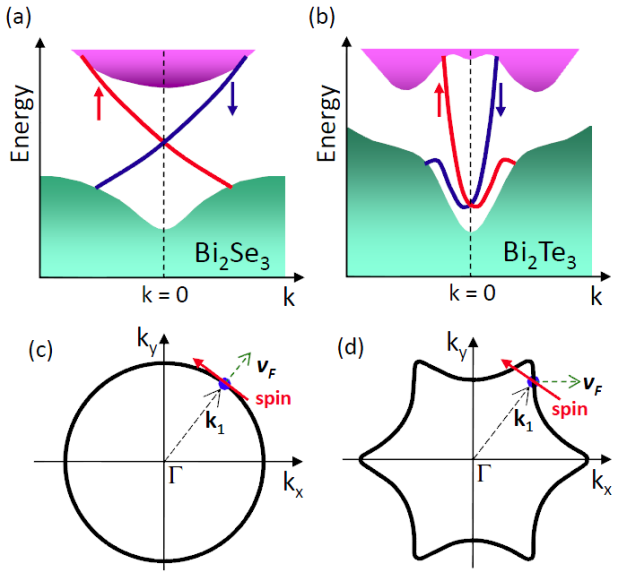

Figure 1.13 Schematic picture of surface state and Dirac cone in Bi_2Se_3 (a) and Bi_2Te_3 (b); and their relative constant-energy contours of Dirac cones(c) Bi_2Se_3 and (d) Bi_2Te_3 [7]

Third, magnetic doping of TI may introducing ferromagnetism in TIs, largely increasing its response and sensitivity to external magnetic field. At the same time, ferromagnetism destroies the surface state, opening a small energy band gap on surface state,

inducing an interesting phenomena, quantum anomalous Hall effect. Therefore, extensive understanding of magnetically doped TIs is still required.

Last but not least, in order to make sensors and switch devices as we proposed we need to investigate magnetoelectric multiferroics to integrated ME and TI in the same device. There is therefore a requirement to develop magnetoelectric materials with low leakage current and high ME coupling coefficient.

Based on the problems and challenges above, I will approach the TI based magnetic sensors and devices in the following three aspects:

First, grow large pieces with low surface roughness and large terrace width and thickness controllable epitaxial TI thin films by MBE. Second, optimize a TI system aiming at reducing the bulk conductivity and increasing surface carrier mobility by changing systematic with different elements. Third, explore the magnetic doped TI about its response to a magnetic field and improve the sensitivity of the response. Fourth, utilize Hall effect (HE) and anomalous Hall effect (AHE) to design high sensitivity magnetic sensor using magnetic doped TI. Last, for integrating switch device, study magnetoelectric multiferroics by using high magnetostriction sensitivity material with doping element to increase magnetostriction derivative term in the coupling coefficient

CHAPTER 2. SAMPLE SYNTHESIS AND MAJOR EXPERIMENTAL TECHNIQUES

Different techniques of sensor fabrication, characterization and testing have been applied in this work according to different sensor applications. For thin film sensors based on topological insulators, molecular beam epitaxy (MBE) method were used for thin film deposition. Characterization methods such as reflective high energy emission diffraction (RHEED), atomic force microscopy (AFM) were applied to the as-growth thin film to detect the quality of samples. Plasma etching method was used to fabricate micro sized magnetic sensors. For a multiferroic bulk senor in this work, solid state reaction method were used to fabricate the material and characterization methods such as X-ray diffraction for crystal structure, scanning electron microscopy for surface morphology, SQUID for magnetic properties, and electronic properties with a LCR meter. In the chapter, detailed information on most of the equipment and techniques will be introduced.

2.1 Molecular Beam Epitaxy (MBE)

Since Cho and Arthur first successfully investigated GaAs epilayers in high-vacuum epitaxy growth techniques in the late 1960s, the particle beam technique developed rapidly. This development accelerated when different semiconductor devices with quantum-well structures were invented in the 1970s [54]. Since then, MBE began to be used in implement in all kinds of devices such as quantum-well lasers, ion gauge, high-electron mobility transistor and superlattice avalanche photodiodes. It is a versatile technique for growing thin epitaxial structures made of semiconductors, metals or insulators.

The schematic picture of the basic physical processes in the MBE vacuum chamber is shown in Figure 2.1. The essential elements in the chamber include heater, substrate, effusion

cells, crucibles with source materials, RHEED gun and screen. There are also two valves connecting to transfer chamber and cryo-pump. There are mainly three zones where different physical phenomena take place. The first zone is the generation zone where molecular beams are generated from sources of the Knudsen effusion cell. The cell temperature can be accurately controlled by proportional-integral-derivative (PID) controllers. The desired chemical composition of the thin film can be obtained by choosing the appropriate cell and substrate temperature which will be addressed in detail in Chapter 4 .

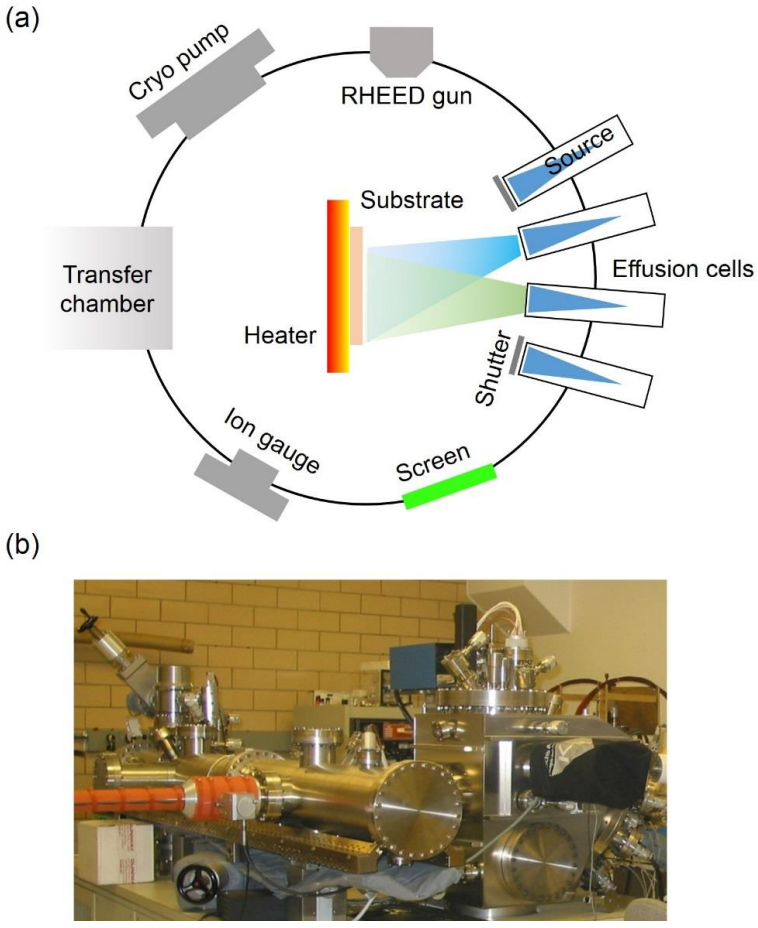

Figure 2.1 Molecular Beam Epitaxy (a) Schematic picture of MBE vacuum chamber (b) Picture of MBE used in this work

The second zone is where beams from different sources intersect each other and the vaporized elements mix together creating a gas phase contacting the substrate areas. The heater and substrate can be considered as the third zone where crystallization process takes place.

During growth, the source materials are heated to a certain temperature, then by opening the shutter in front of the effusion cells, molecular beams evaporate into vacuum chamber and arrive at the substrate surface. Therefore, the evaporation rate is important because it controls the composition of grown epilayers. The growth rate maintained at 1μm/h is low enough that surface migration. Therefore, the surface of the grown film is very smooth. The RMS roughness can maintained lower than 1 nm in the present work.

Although the van der Waals gap between quintuple layers makes less requirements of lattice matching with substrate in TI thin film growth, I still find mica susbtrate gives the best quality thin film compared to Si and GaAs. Figure 2.2 shows the mica substrate and mica crystal structure. It is a layer-by-layer structure. Before mounting the substrate on holder, a new fresh surface of mica can be cleaved which is easier than Si substrate standard cleaning procedure. Figure 2.3 (e) shows my TI sample on a 2 inch diameter mica substrate.

There are mainly three aspects that make MBE superior to other deposition methods including the ultra-high vacuum (UHV) chamber during growth, the significantly more precise control of the beam fluxes and *in-situ* characterization methods. The definition of Ultrahigh Vacuum is the pressure $p \leq 10^{-9}$ Torr (1.33×10^{-7} Pa). In our experiments, the chamber base pressure is always maintained at $p = 10^{-10}$ Torr and $p = 10^{-9}$ Torr during growth. Since growth is carried out in such a high vacuum, the growth processes, far from thermodynamic equilibrium, is governed mainly by the kinetics of the surface processes. This is different from

other epitaxy such as liquid phase epitaxy or vapor phase epitaxy which is carried out under a thermodynamic equilibrium state around the substrate.

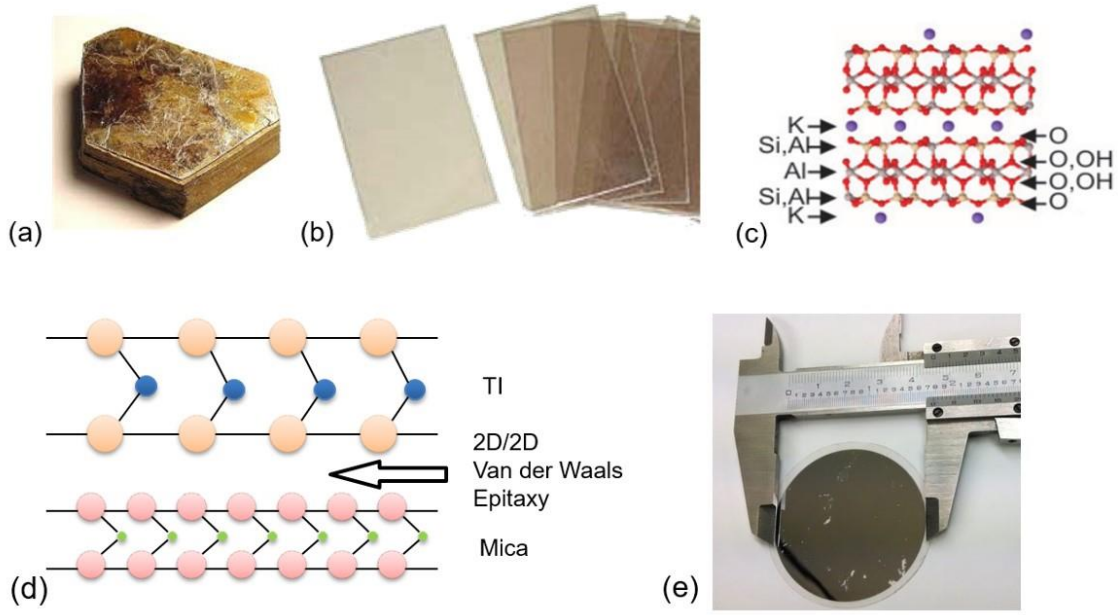

Figure 2.2 Mica crystal(a) and mica substrate(b). Mica crystal structrure(c). Schematic picture of van der Waals epitaxy of TI on mica(d) and sample on mica in present work(e).

Another advantage of MBE compared to other deposition techniques is the surface and crystal structure of the as-grown film can be in-situ diagnose by Reflection High-Energy Electron Diffraction (RHEED). The process of RHEED is a high energy beam of electrons (5-40keV) is directed at a low angle (1° - 3°) to the substrate surface. The penetration of the beam into the surface is low and is restricted to the top several atomic layers, as the surface roughness is different due to the different deposition condition. The diffraction process in RHEED is also different. On rough surfaces, the process is dominated by the electron beam transmission into some part of the surface and then reflection which always leads to a spotty feature pattern, whereas, for the electron beam that undergoes true reflection diffraction, in which the beam

leaves the scatter from the same surface where the incident beam entered, the diffraction pattern is in the form of elongated streaks as shown in Figure 2.3.

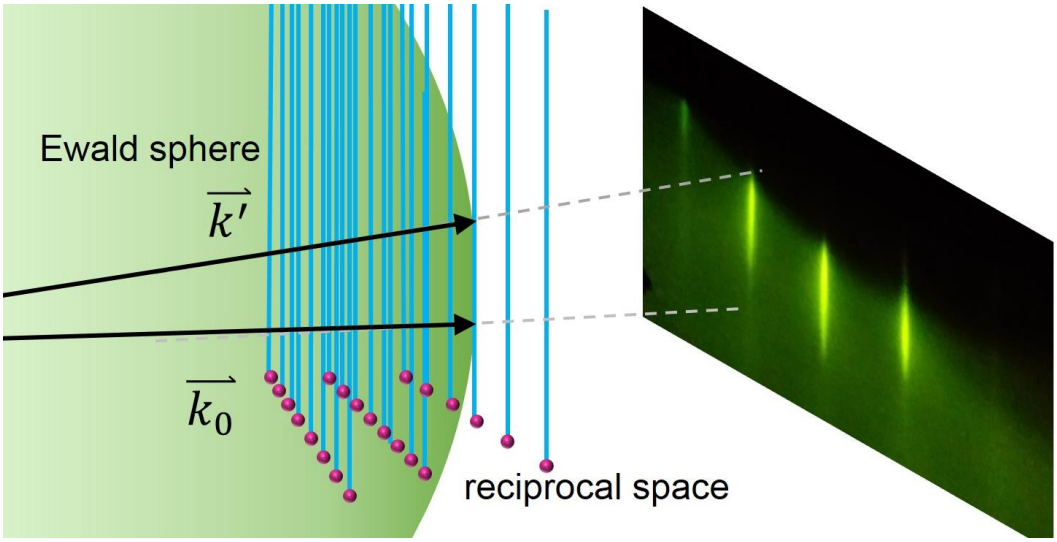

Figure 2.3 Schematic showing an Ewald sphere with radius k_0 cutting into the surface reciprocal rods, leading to a diffraction pattern.

This is because electrons interacting with the epitaxial growth layers with a smooth surface can be considered as electrons interacting with a two-dimensional atomic layer. The third dimension can be neglected. Therefore, the surface layer in reciprocal space can be defined as rods perpendicular to the sample surface. Moreover, the magnitude of the wave vector $\overrightarrow{k_0}$ of the incident electron beam, also known as the radius of the Ewald sphere, can be calculated using this equation: $\left|\overrightarrow{k_0}\right| = \frac{2\pi}{\lambda} \approx 2\pi \frac{\sqrt{V(1+10^{-6}V)}}{12.247}$ where V is the accelerating voltage. In our experiment, the accelerating voltage is 20 keV. The corresponding magnitude of radius is $\left|\overrightarrow{k_0}\right|$ = 5 nm, which is over ten times larger than the distance between reciprocal rods. Figure 2.3 shows the schematic picture of an Ewald sphere with radius k_0 cutting into the surface rods in reciprocal space leading to a streaky diffraction pattern. Note that, in order to prevent the

scattering of electron beams by gas molecules in the chamber, RHEED must be performed at UHV chamber.

2.2 Hall Sensor Fabrication by Plasma Etching and E-beam Lithography

To demonstrate, a Hall effect sensor based on topological insulator thin films, Hall bars were fabricated using a plasma etching method. It is a kind of dry etching used widely in microfabrication process in semiconductor industry. It is superior to conventional wet etching methods in many aspects including no chemical consumption, no photoresist adhesion problems and anisotropic etching. The purpose of dry etching is to create an anisotropic etch and a unidirectional etch. An anisotropic etch is critical for high-fidelity pattern transfer.

A schematic picture of common plasma etching setup is shown in Figure 2.4(a). A plasma etching system consists of a vacuum chamber, two electrodes that create an electric field for accelerating ions towards the surface of the samples. What is between the two electrodes is plasma, which is generated with an radio frequency (RF) powered electromagnetic field applied to the bottom electrode. Plasma contains both positively and negatively charged ions in equal quantities. The plasma etching requires a high vacuum level, for which the base pressure reach the value of 10^{-6} Torr in my experiment. Ar gas is used to generatre an Ar plasma. Ar gas enters through the top of the chamber and exits to the turbo pump system through the bottom for several times to make sure the chamber is filled with Ar gas. Then, a plasma can be initiated by applying an RF EM field with 100W in my experiment. After a few cycle of an EM field, the electrons are absorbed into the two electrodes leaving the relative massive Ar^{+}. The electron accumulated charge in the wall generates a high voltage between two electrodes. The positive ions accelerated in the electric field, causes them to collide with the surface of the sample surface.

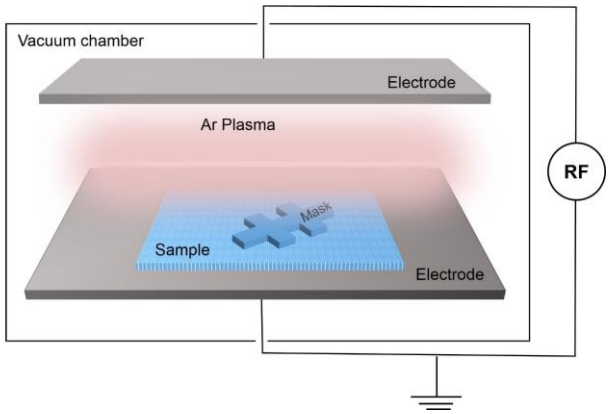

(a)

(b)

Figure 2.4 Schematic picture of plasma etching for Hall sensor fabrication (a) and equipment in use for this work (b).

The interaction of the surface and ions depends on the type of plasma with different principles including volatility, adsorption, chemical affinity and ion-bombardment. In my case, most of the etching happens in a physical process through ion-bombardment. The area covered by the Hall bar mask remains while other areas of the sample will be etched away. The etching rate depends on several aspects such as the electron source, pressure in the chamber and the gas species. Carefully adjust parameters regarding to the above aspects provides clean sharp interfaces after etching. The equipment I used is shown in Figure 2.4(b).

Electron beam lithography method is used to fabricate small size sensor. The process flow chart is shown in Figure 2.5 (a). After epitaxy growth of TI thin film on mica, photoresist was applied. The Raith e-beam lithography [(Figure2.5(b)] is used to writing the feature on the thin film. Then developing the sample to transfer the feature on to photoresist. Then etching away TI and remove the photoresist.

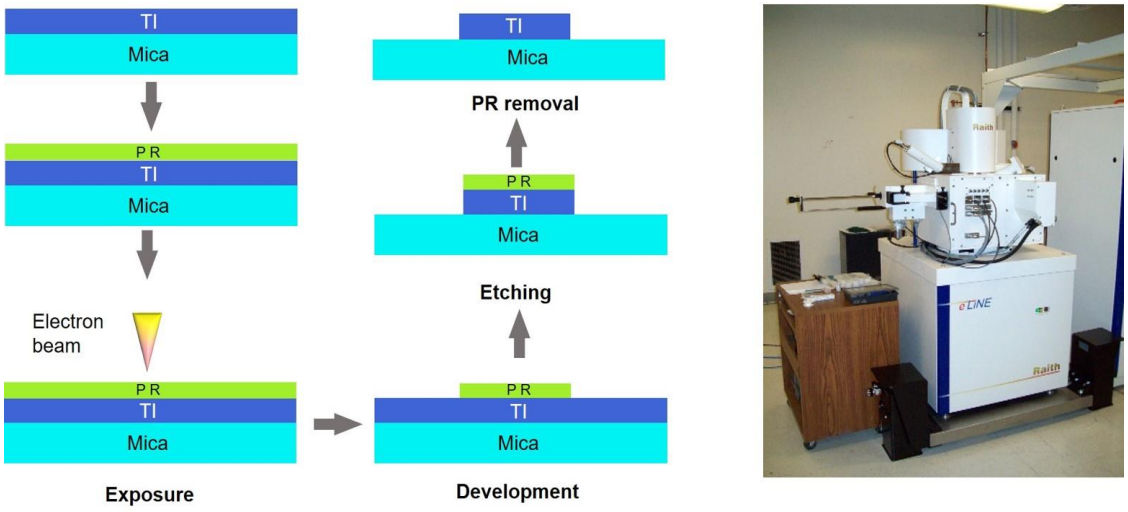

Figure 2.5 Electron beam lithography process of sensor fabrication. Flow chart of Hall sensor fabrication (a) and Raith e-beam lithography (b).

The above sessions introduced sample preparation and sensor fabrication methods in my experiment. Since sensor design and device performance largely depend on the material properties, for example, in my study, magnetization, piezoelectricity, magnetostriction of multiferroic materials and carrier density, mobility of topological insulators, the characterizations play an important role for future device testing. The following sessions are characterization methods after sample fabrication including X-ray diffraction and atomic force microscopy. After that, sensors made from an ME composite and TI thin films will be tested under various external fields.

2.3 X-ray Diffraction Measurement (XRD)

X-ray diffraction is a method of investigating the crystal structure and atomic spacing of materials. The measurement is based on constructive interference between a monochromatic X-ray and a crystal sample. An X-ray diffraction pattern can be used as a “fingerprint” to identify the crystal structure since every crystalline solid has its unique features of atom

arrangement. An X-ray is generated in ab X-ray tube which contains a cathode, an anode target. By applying high voltage to the cathode, the electron is "kicked" out of the cathode and hits the target, emitting X-ray. The generated X-rays are filtered by a matching material with particular absorption characteristics in front of the X-ray source to produce monochromatic radiation. Then the X-rays are collimated to concentrate, and directed toward the sample. The diffracted rays are then received by a detector. Figure 2.6 depicts schematically the X-ray diffraction machine used in our experiments (Siemens D500) which is equipped with an X-ray tube, the sample under test and a detector to pick up the diffracted X-rays. The left part is the X-ray generator, the right part is the detector to receive rays reflected from the samples. In the middles is the sample and holder.

The schematic picture of incident rays interacting with a sample is shown in Figure 2.6(b). The path difference between the two waves is $2d\ sin\theta$. For constructive interference between these waves, the path difference must be an integral number of wavelength (λ). This leads to the Bragg equation: $n\lambda=2d\ sin\theta$; where n is an integer, λ is the wavelength of incident rays, d is the spacing between the planes in the atomic lattice, and θ is the angle between the incident rays and the scattering planes. A diffraction pattern is obtained by measuring the intensity of scattered waves as a function of scattering angle (2θ). Certain crystal structure has its own diffraction pattern which can be researched in PDF card.

In my work, an X-ray diffraction measurement is used for the following two purposes. First, it is used in detecting different phases during the process of fabricating a cobalt ferrite/barium titanate based composite sensor. Because cobalt ferrite has a spinel structure while barium titanate is tetragonal at room temperature, it is easy to use X-rays to detect these two phases in the composite.

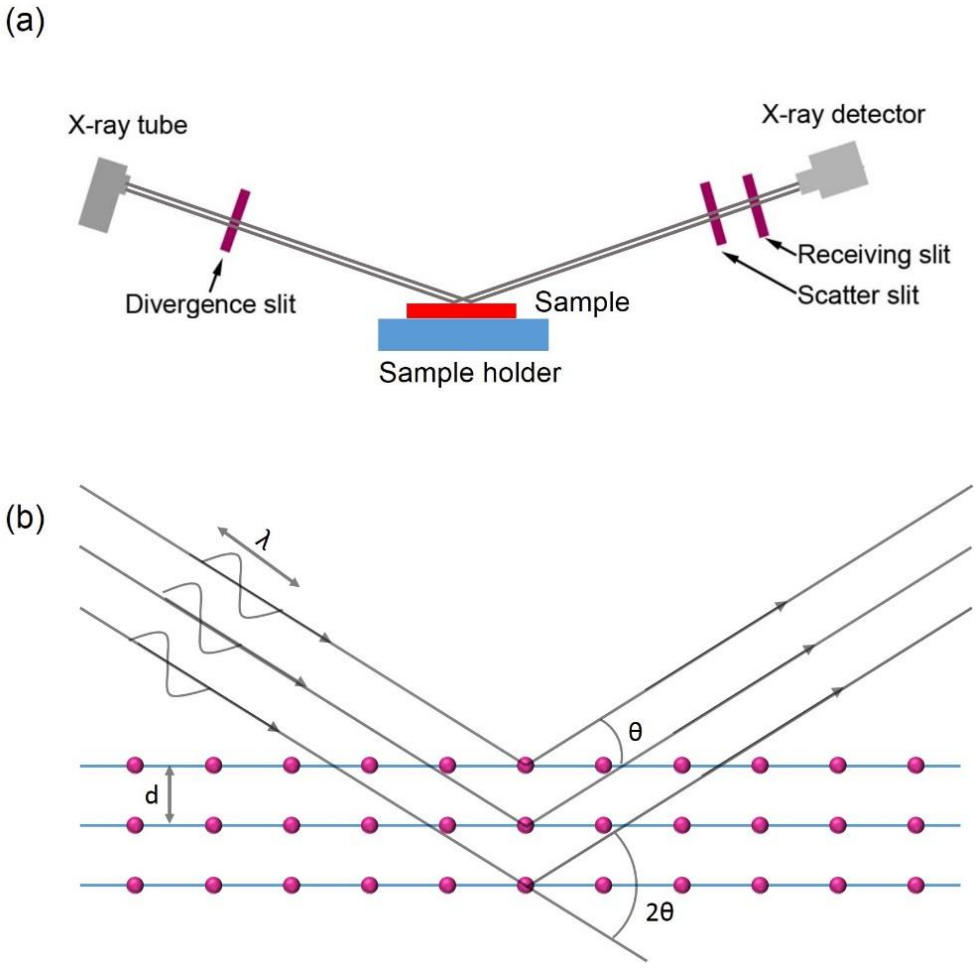

Figure 2.6 Schematic picture of (a) X-ray diffraction machine setup (b) incident X-rays with a certain wavelength interact with a crystal producing constructive interference.

At the same time, extra phases can be detected if other peaks appear in the diffraction pattern. Second, the lattice spacing in a topological insulator along the *c* axis can be determined by X-ray diffraction. Since topological insulator epitaxy thin films are highly anisotropic with a single crystal structure in the x-y plane while epitaxy along c-axis, only diffraction peaks from the [55] family planes can be observed. The detailed analysis of an X-ray diffraction pattern will be discussed in each result sections in following chapters.

2.4 Atomic Force Microscopy (AFM)

Atomic Force Microscopy (AFM) is one of the Scanning Probe Microscopy family which is used to investigate the surface properties of materials from micron to atomic level. The invention of AFM open the door for studying the surface of poorly conducting materials. This field were prohibited due to the problem of surface charging when using the conventional surface detecting techniques. AFM probes the surface with a sharp tip, which is several microns long and less than 10nm in diameter. As shown in Figure 2.7, the tip is located at a free end of a cantilever about 100-200μm long. During experiment, the piezoelectric stick force the cantilever to vibrates near its resonant frequency. Forces of the interaction between the surface atom and tip caused the cantilever bend. The bending is monitored by a detector, in most cases, an optical lever. It operates by reflecting a laser off the cantilever. The reflected laser beam strikes a position-sensitive photo-detector consisting of four-segment photodetector. The differences between the segments of photodetector of signals indicate the position of the laser spot on the detector and thus the angular deflections of the cantilever. Several forces contribute to the bending of cantilever. The most commonly associated force is van der Waals force.

During experiment, I use the tapping mode of Veeco MultiMode SPM. This is a non-contact mode which means the cantilever is held on the order of tens to hundreds of angstrom from the sample surface. The force between the cantilever and surface is attractive according to the relationship between interatomic force and distance. The space between the tip and sample also protected sample being contaminated through the experiments. Besides the AFM image, for the device application concerning, RMS surface roughness is another important

parameter. In order to achieve high performance sensor, the rms roughness should be less than 1nm to prevent the scattering of electrons by the surface in topological insulator epitaxy films.

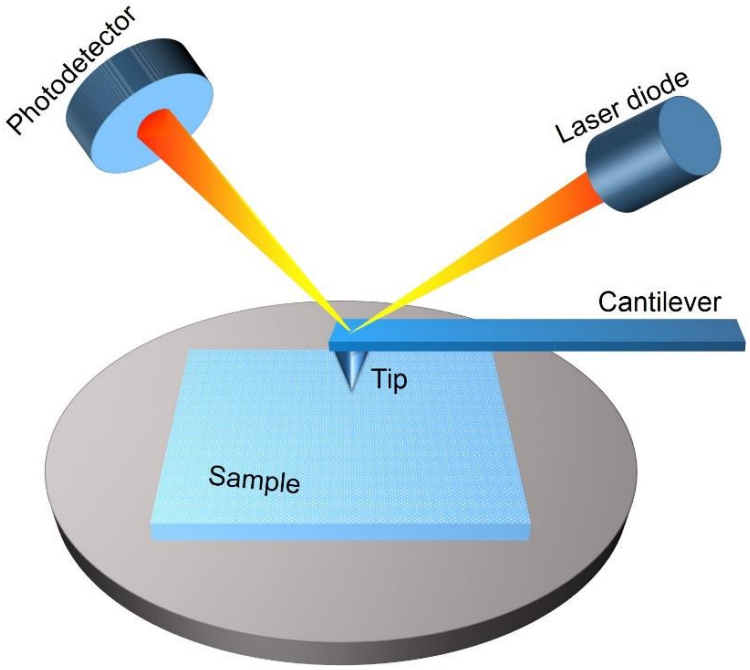

Figure 2.7 Schematic picture of atomic force microscopy (AFM).

2.5 Composite Sample Preparation Procedures

In this work, the ME sensor is based on a composite made from cobalt ferrite, a high magnetostrictive compound, and barium titanate, a typical piezoelectric compound. I used solid state reaction method to fabricate cobalt ferrite and barium titanate separately and then mix the powder of each and sintering them into composites. The sample preparation flow chart is shown in Figure 2.8. The raw materials are first weighed according to the stoichiometric formula of composition desired, for example, the fabrication of cobalt ferrite include high purity Co_3O_4(99.9%) and Fe_3O_4 (99.9%). And then, the weighted materials are put in a ball stainless steel milling jar and are mixed with 25g stainless steel balls. Then the jars are fixed on a ball milling machine, which can rotate at a specific speed (300r/min) and so as to mix the

powder to homogeneous state. The balls are used to increase the milling efficiency. It takes about six hours for mixing. Then, the mixture were pressed into lumps and then calcined in ambient air at certain temperature to carry out the chemical reaction and gain certain crystals. For pure $CoFe_2O_4$, the calcining temperature is ~1000°C. With adding dopants such as Ga into $CoFe_2O_4$, the calcination temperature varies dependent on the concentration of dopants. Since the calcination temperature has a great influence on density and other properties of final products, it is very important to control it to a narrow range.

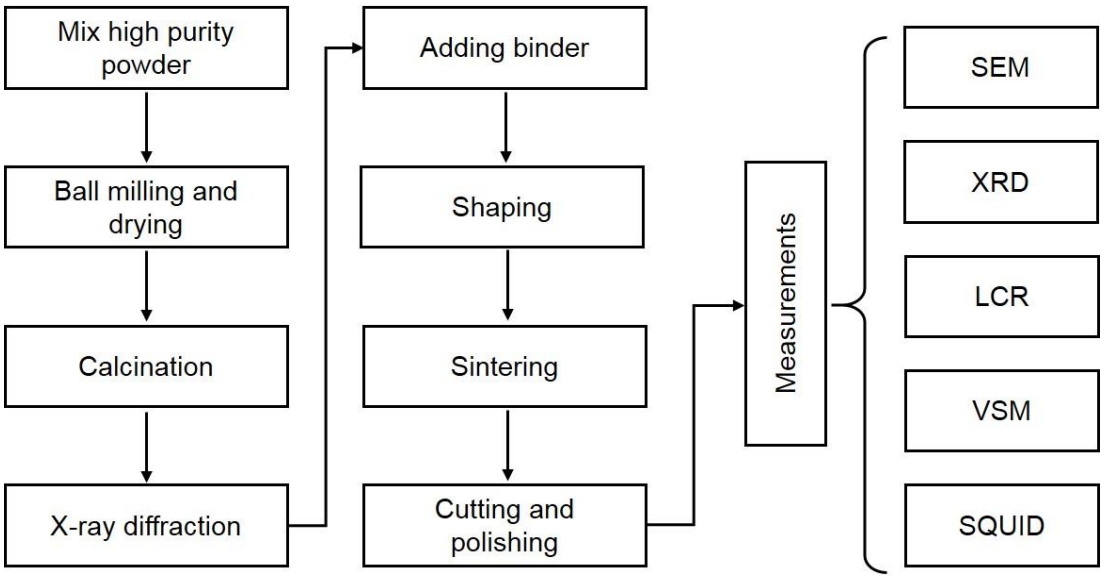

Figure 2.8 Sample fabrication and characterization flow chart of magnetoelectric multiferroic sensor

After that, products will be a bulk material, which need to be grinded again to a convenient particle size by ball milling. After above process, PVA bender were added into the powder for sintering. The effect of the binder is to bind crystalline grains together and make the flakes easy to form. Grinding is needed to make sure the binder distributed in the sample homogenously. The granules are pressed into disk shape which will be used as the sensor during the following test. The samples were heated very slowly to 500°C and kept at this

temperature for one hour to remove any binder. After the binder burned out, the samples are taken to a higher temperature for sintering. The sintering temperature and time should be optimum for proper densification to occur without abnormal grain growth. The sintering of oxide ceramics must be carried out in an oxidizing atmosphere or in air. After sintering, the sensor are ready to be tested under different external fields such as temperature, electric field and magnetic field. The sensitivity can be calculated after the experiments. Chapter 8 will introduce magnetoelectric multiferroic sensor based on Ga doped cobalt ferrite and barium titanate composites.

CHAPTER 3. TOPOLOGICAL INSULATOR GROWTH AND CHARACTERIZATION

Since three-dimensional topological insulators were theoretically predicted and experimentally verified, they are by far the most studied TIs that could be applied to the microelectronics and spintronics. Among these groups, bismuth and antimony based binary and ternary compounds attract most attentions. Therefore, growth of these TI crystals are crucial toward the implementation of devices based on TI. Previous researches focus mainly on two aspects, reducing defects concentration in crystal and increasing the surface area to volume ratio, in order to suppress the proportion of bulk electrons from the surface electrons which enable the unique surface conduction differentiated from the bulk. Moreover, in order to lower the bulk conduction due to the position of Fermi level, doping element between different TI systems allows manipulating relative position of Fermi level and band gap to achieve the ideal band structure of TI. In this chapter, I will focus on the TI thin film growth and characterizations which is the basic for the following chapters and device applications.

3.1 Introduction

The newly discovered and developed three-dimensional topological insulator draws an increasing attention due to their unique surface states, which leads to the exotic surface conductivity comparable to graphene. Among these 3D TI systems, V-VI semiconductor compounds are most studied because their relative simple surface band structure and relatively large bulk gap. These systems are based on bismuth (Bi), antimony (Sb) and tellurium (Te) binary and ternary compound including Bi_2Te_3, Sb_2Te_3, Bi_2Se_3, $Bi_xSb_{2-x}Te_3$, $Bi_xSb_{2-x}Se_3$. Although the bulk materials of these systems has been used as superior thermoelectric application due to its high thermoelectric figure of merit at room temperature, the application

regarding to topological surface state behavior requires much higher quality of crystals in order to reduce electron scattering and bulk electrons concentration. Many methods were reported on crystal growth of above systems both in bulk and nanostructure. Single crystal bulk topological insulator based on Bi_2Te_3, Sb_2Te_3, Bi_2Se_3 alloy were grown by the Bridgman method and self-flux techniques in many laboratories world-wide. The experimental observations of the exotic electronic states has been observed on the cleaved surfaces of bulk single crystals. However, with the explosion of interest in nanostructures such as nanoplates and nanoribbons of TIs since the surface properties are dominant due to large surface to volume ratio, most experimentalists works on exploring the nano sized, low dimensional TI crystals. Chemical vapor deposition (CVD), solvothermal synthesis, vapor-liquid-solid (VLS), vapor-solid method (VS), sputtering, paulse laser deposition (PLD) and molecular beam epitaxy (MBE) are most popular techniques to synthesis TI nanostructure. Among all these methods, MBE growth gives the best quality crystals due to its layer-by-layer epitaxy growth mechanism. Moreover, TI thin film growth by this method allow us to precisely control thickness and doping element concentration. The surface roughness of thin film by MBE could reach lower than 1nm which enables them to be used as nano size electronic device with enhanced surface carrier mobility. In this work, all the sample are grown using MBE method. The properties of thin film can be influenced by parameters such as the source material temperature and flux rate, substrates, substrate temperature, growth rate and time, which will be addressed in the following parts.

3.2 Source Material Temperature and Flux Rate Control

In this work, MBE is used to grow TI thin films because of its deposition rate (typically less than 100 nm per min) that allows the films to grow atomic layer by atomic layer. These

deposition rates require proportionally ultra-high vacuum (UHV) to achieve the same impurity levels as other deposition techniques. The absence of carrier gases as well as the UHV environment result in the highest achievable purity of the grown films. Typically, the source material was heated up based on their vapor pressure shown in Figure 3.1.

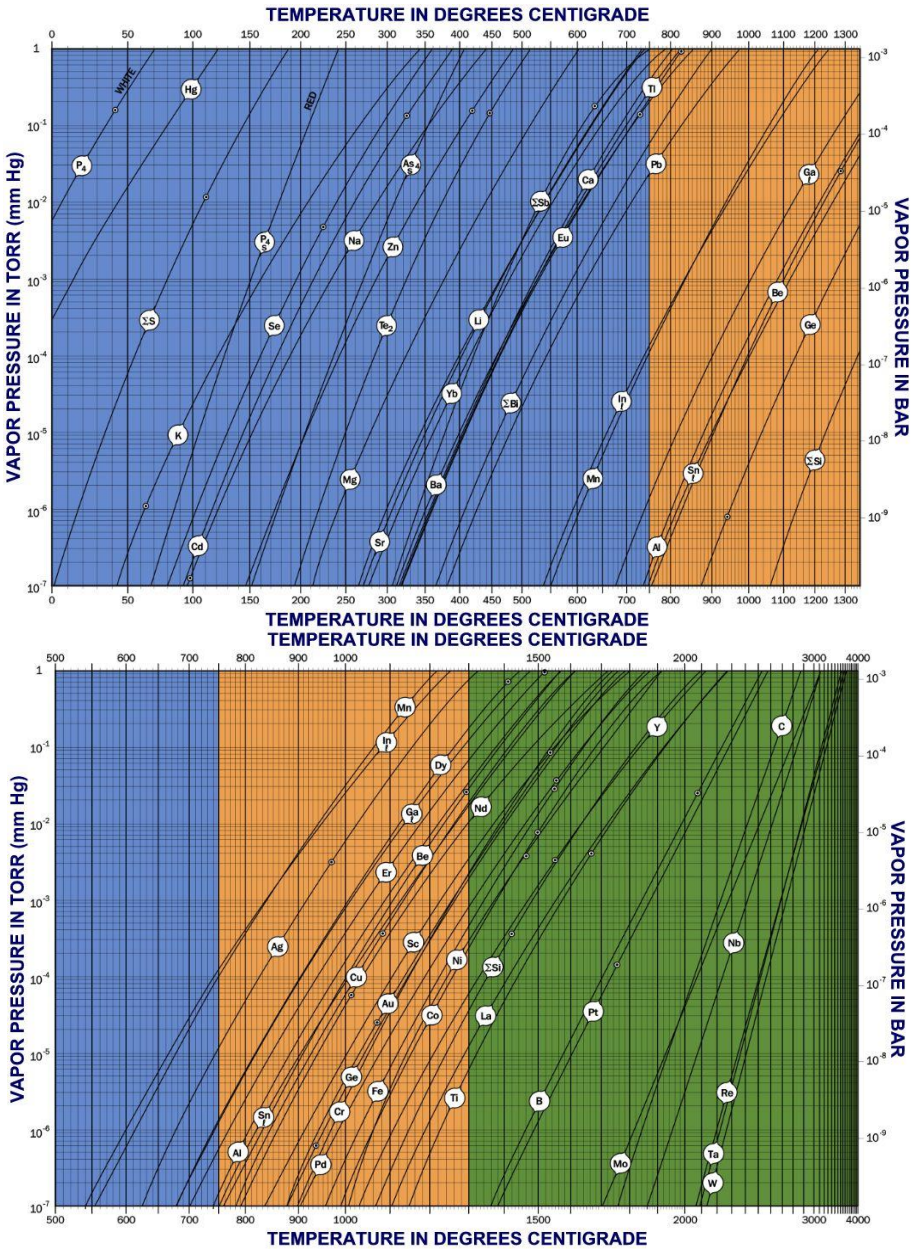

Figure 3.1 Vapor pressure curves of solid elements [56].

In order to monitor the flux of source materials Sb and Te, several different temperatures of Sb and Te were chosen and grow separately on substrates. High quality thin film sample of Sb_2Te_3 requires the source material flux ratio of Te to Sb ratio approach 10 to 1 during the growth. This is because Te molecules (Te_2) tends to evaporate easier than atom Te, which will lead to low concentration in the chamber during growth, which results in lower quality film because of Te vacancy. During the same growth time period, the thickness of the sample with only Sb and Te respectively will reflect the source material flux during the growth.

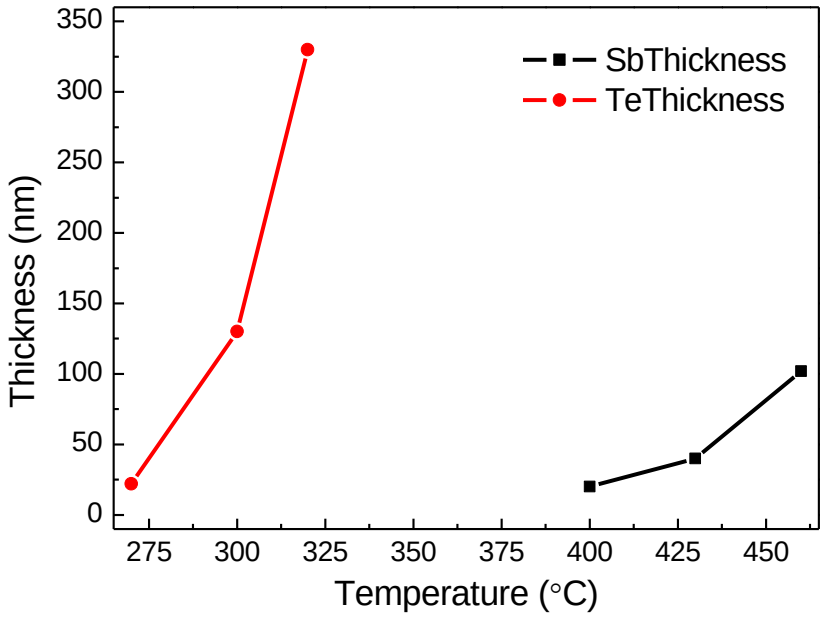

Figure 3.2 Thickness of Te and Sb thin film as a function of source temperature when substrates were at room temperature

Figure 3.2 shows summary of the thickness results as a function of source material temperature. When Te temperature at about 300°C and Sb at between 400°C to 425°C, the thickness ratio of Te and Sb is 10:1. Further increasing temperature will speed up the deposition rate and destroy the epitaxy process. Overall, material flux rate is controlled by the

heating temperature of source material. To get high quality film, not only the flux rate of different source should collaborate but also the heating temperature should maintained in a level keeping the epitaxy growth.

3.3 Substrates Selection for Device Application

As introduced in the previous chapter, V_2VI_3 based TI are rhombohedral structure at room temperature, which can also be described in a hexagonal unit cell with layered atoms known as quintuple layer (QL). QLs are held together with Van der Waals bond, which lead to crystal anisotropy in a certain direction similar to MoS_2 and graphite. The crystal structure of TI determine the epitaxy mechanism is different from other material typically grown by MBE such as GaAs. The epitaxy of TI thin film on substrate displaying no dangling bonds and only weak van der Waals like forces act across interface of thin film and substrate, which is known as Van der Waals epitaxy (VDWE). This kind of epitaxy growth relaxes the lattice matching condition allowing a large variety of substrates such as sapphire, Si, InP, BaF2, GaAs. In this work, I also grow TI on different substrates, which are, Si, GaAs and Mica. The following parts will describe the problems during growth on different substrates and then compare the film quality on different substrates.

GsAs (111) has been used as substrate to grow Sb_2Te_3. In the couples of samples I grew on (111) GaAs substrate before deoxidation process of the substrate, none of them have roughness below 1nm which is the level of roughness we generally get on good quality TI film on mica substrate. Figure 3.3(a) shows the AFM image of Sb_2Te_3 film on (111) GaAs with Sb temperature at 390°C, Te temperature at 300°C and substrate temperature at 235°C. The overall roughness in a 5μm by 5μm scanning area is 16.72nm. Some other samples shows more or less similar roughness. Figure 3.3(b) shows the surface morphology of sample after

deoxidation with the same growth parameter as Figure 3.3 (a), which is heating up substrates to 600°C and cool down before starting growth. The roughness dramatically decrease to 0.9nm in a 5μm by 5μm scanning area. However, the terrace structure is not clear and sharp. This may cause by the non-smooth surface of GaAs after heating up to high temperature.

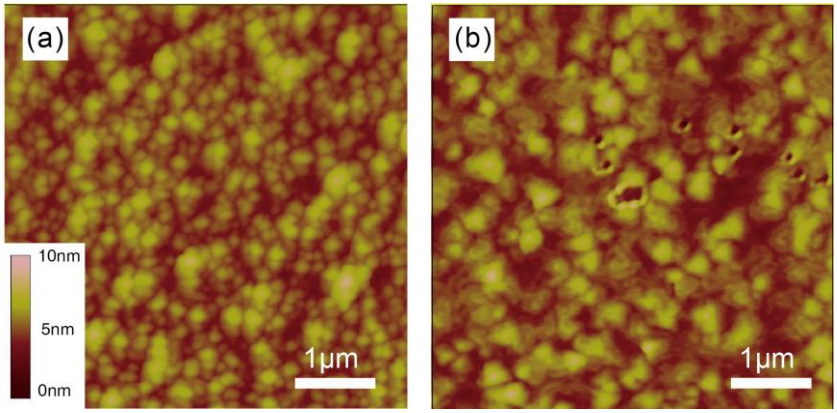

Figure 3.3 AFM image of Sb_2Te_3 film on <111> GaAs (a) before deoxidation and (b) after deoxidation at 600°C.

Another substrate, Mica, is also used to grow TI thin films. Representative surface profile of Sb_2Te_3 thin film grown on mica is shown in Figure 3.3. It is found that over large length scale (5×5 μm^2), the thin film possesses a terrace structure, which indicates the layer-by-layer growth mechanism on mica substrate. The 2D-nature of the surface is also revealed by the streaky RHEED pattern shown in the inset of Figure 3.3(a). The root-mean-square (RMS) roughness of the sample was measured to be 0.73 nm. Note that the present thin film possesses quite low surface roughness compared with MBE grown Bi_2Se_3 thin films on sapphire [57], Bi_2Se_3 thin films on flat Si (111) substrate [58], Bi_2Se_3 thin films on InP (111) substrates [59], and Sb_2Te_3 thin films on GaAs (111) substrates [60]. Our results indicate that mica substrate is a good candidate for the growth of TI thin films in terms of its atomic smooth surface, chemically inert nature, thermally stable state, highly transparent, flexibility, and perfect insulate. Therefore, results in following chapters are all based on TIs on mica.

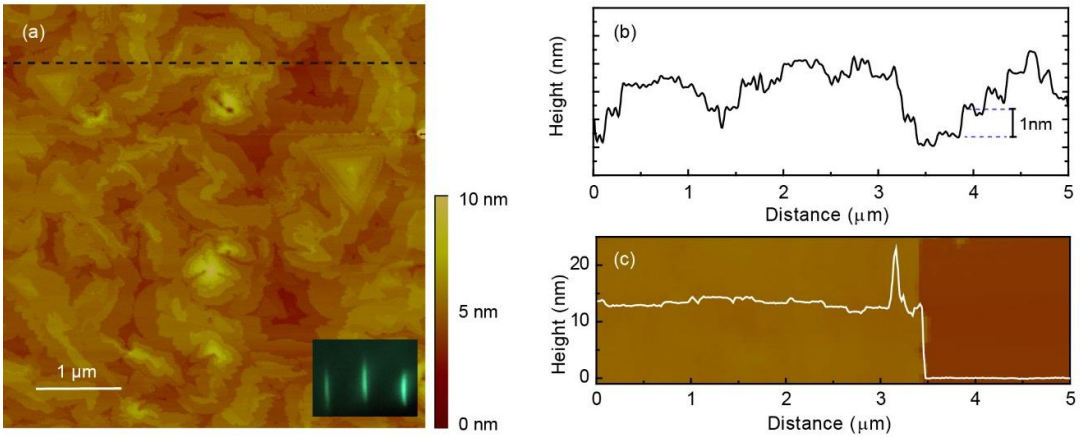

Figure 3.4 (a) AFM image of a Sb_2Te_3 thin film deposited on mica substrate. Inset shows its streaky RHEED pattern, indicating the 2D-growth of thin film. (b) Topography of Sb_2Te_3 thin film along the dashed line, displays the quintuple-layer structure. (c) Thickness profile of Sb_2Te_3 thin film.

Topography of the thin film marked with dashed line is shown in Figure 3.4(b). This result demonstrates the terrace growth of thin film in a large area. For instance, at the distance of 4 μm ~ 4.5 μm, five quintuple layers can be observed with thickness of each quintuple layer being ~ 1 nm. Thus, this result further confirms the layer-by-layer epitaxial growth of thin films. The topography of the scratched film and the height information are shown in Figure 3.4(c). It is found that a steep edge is formed by scratching. The light color region on the left and the dark region on the right indicate TI thin film and mica substrate respectively. The white line indicates the height profile along the horizontal axis. The sudden drop of the black line reveals the thickness of thin film is ~ 12 nm. Considering 30 minutes growth time, the growth rate was maintained as 0.4 nm/min. Figure 3.5 shows Sb_2Te_3 growth on different substrates. We can see that Sb_2Te_3 growth on mica shows the largest area of terraces, the most sharp interfaces and lowest roughness according to AFM. Also, mica is cheaper and easier to prepare compared to Si and GaAs. Moreover, mica is also transparent in the visible light wavelength,

together with its flexibility, TI thin film on mica substrate could potentially used in optoelectronics.

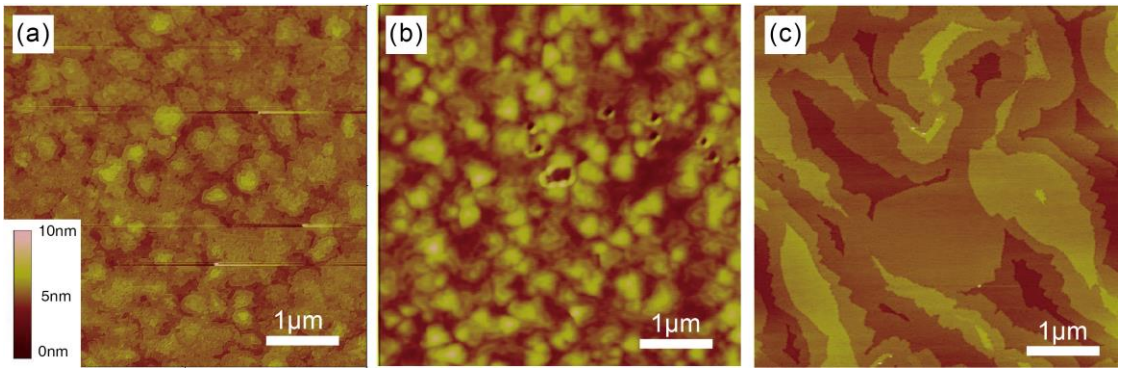

Figure 3.5 Surface morphology of Sb_2Te_3 film on (a) <111> Si (b) <111> GaAs (c) mica substrate.

3.4 Substrate Temperature Effect on Film Quality

Substrate temperature is an important parameter that influence film quality. If the substrate temperature is too low, when atom deposited on substrate, there is not enough kinetic energy for the atoms to move around. Therefore, even if the flux ratio of the source is sufficient, inefficiency in the reaction exist between the atoms. We carried out a systematically study on the substrate temperature effect of thin film on mica shown in Figure 3.6. As shown in Figure 3.6(a), the thin film surface shows elongated nano pillars when the substrate temperature is at 170°C. However, if the temperature is too high, screw islands appear as shown in Figure 3.6(e). Only within a narrow temperature window, the film shows large terraces and epitaxy growth with low roughness. In this set of sample, the best substrate temperature is between 230°C to 235°C. As shown in Figure 3.6(d) both nano pillars and screw islands disappear, only large terraces with 0.3nm RMS roughness observed in this substrate temperature. Since the surface state is the key to the unique property of topological insulator, low surface roughness plays crucial role in determining the success of thin film growth. The roughness of film with different

substrate temperature is summarized in Figure 3.6(f) which shows first decreasing and then decreasing tendency upon heating.

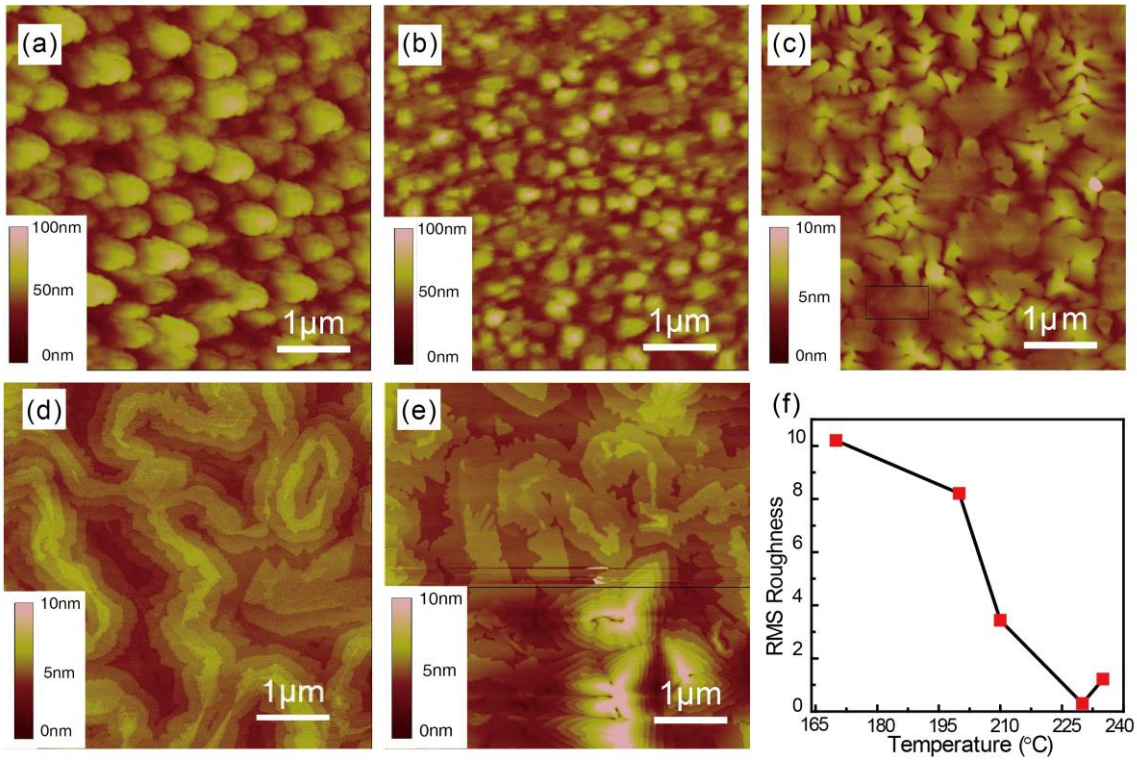

Figure 3.6 Surface morphology of Sb_2Te_3 film on mica substrate with different substrate temperatures (a) 170°C (b) 200°C C (c) 210°C (d) 230°C (e) 235 °C; (f) RMS roughness of above samples.

3.5 Element Doping in Thin Film Growth

Doping is a common method to control the properties of semiconductors. Similarly, doping element in TI results to interesting properties. As introduced above, Sb_2Te_3 is a p-type semiconductor while Bi_2Te_3 is naturally a n-type semiconductor. Doping Bi into Sb_2Te_3 will increase electron concentration so that tuning the Fermi level and band structure. Moreover, doping magnetic impurities in TI system destroy time reversal symmetry of the surface state and open a small surface gap which leads to quantum anomalous Hall effect. Therefore, to

maintain high quality while adding dopant into TI is important to gauge the possible application of device application of TI.

In the present work, the concentration of Bi in $(Sb_{1-x}Bi_x)_2Te_3$ is adjusted by controlling the cell temperature, and measured by EDS. Since large amount of signals came from mica substrate for 12 nm thin films in EDS measurement, we grew films with 60 nm in thickness to get a convincible composition analysis. Figure 3.7 shows the EDS analysis of $(Sb_{1-x}Bi_x)_2Te_3$ thin film. All the EDS of $(Sb_{1-x}Bi_x)_2Te_3$ on mica substrate share the same feature. Therefore, we take $(Sb_{1.82}Bi_{0.18})_2Te_3$ as an example to show the analysis. The EDS spectrum in Figure 3.7(a) confirms the chemical composition of the thin films. The elements such as O, Na, K, Si, Al are from mica substrate. The ratio of different elements in $(Sb_{1-x}Bi_x)_2Te_3$ thin films can be measured, and the composition of $(Sb_{1-x}Bi_x)_2Te_3$ as a function of the Bi cell temperature during MBE growth is shown in Figure 3.7(b). In this work, Bi started to appear in $(Sb_{1-x}Bi_x)_2Te_3$ with Bi temperature higher than ~ 430 ^oC (Bi concentration, x = 0.014). The highest doping concentration is x = 0.29 with Bi temperature ~ 500 ^oC. The Bi concentration in $(Sb_{1-x}Bi_x)_2Te_3$ as a function of cell temperature can be fitted well with exponential equation [shown in Figure 3.7(b)], which indicates the doping of Bi is a thermally activated process controlled by the evaporation of Bi from the diffusion cell.

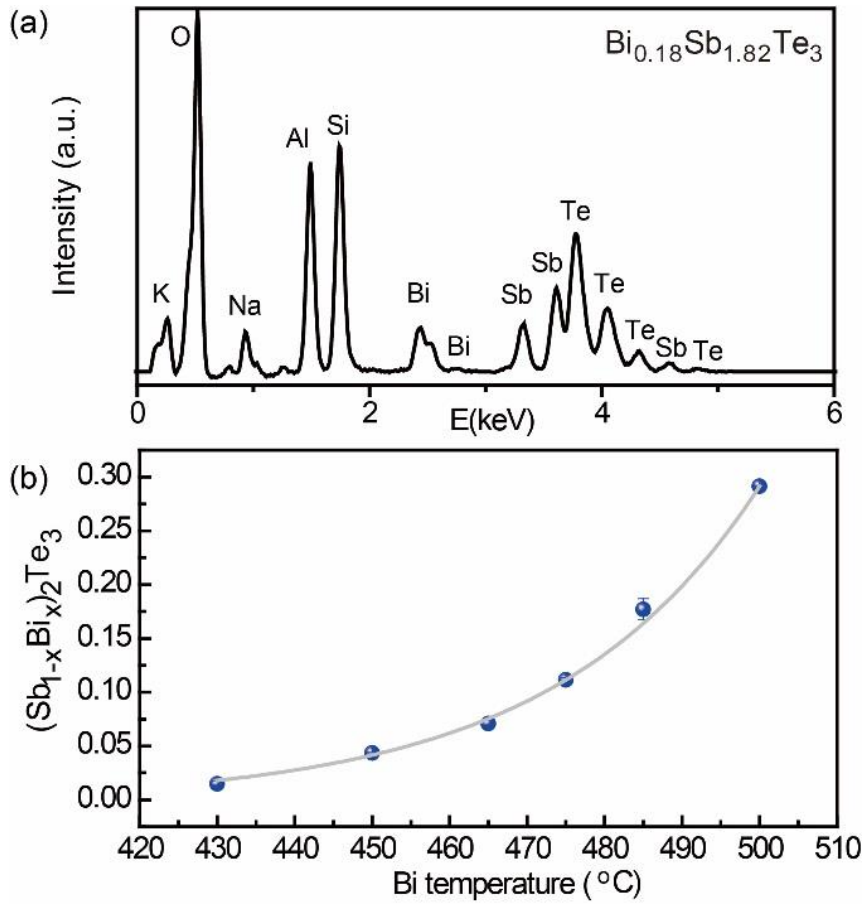

Figure 3.7 Composition and structure analysis of $(Sb_{1-x}Bi_x)_2Te_3$. (a) The EDS spectrum of $(Sb_{1-x}Bi_x)_2Te_3$ with x = 0.18. (b) Bi concentration of $(Sb_{1-x}Bi_x)_2Te_3$ as a function of Bi diffusion cell temperature.

In order to monitor the surface morphology and roughness of thin film after doping Bi, AFM experiments are carried out. Figure 3.8 demonstrates the evolution of morphology of thin films with Bi concentration in $(Sb_{1-x}Bi_x)_2Te_3$. When the Bi is doped into $(Sb_{1-x}Bi_x)_2Te_3$ samples, the surface roughness begins to increase. It is shown in Figure 3.8(a) to (c) that with doping Bi concentration as x = 0.02 to 0.07, the surface is generally flat and the overall roughness remains below 2 nm. Pyramidal-shape terrace over ten quintuple layers can be observed but rarely. With increasing the Bi concentration from x = 0.07 [Figure 3.8(c)] to x = 0.11 [Figure 3.8(d)], the size of the pyramidal-shape terrace becomes larger and the volume

fraction of it also increases. Correspondingly, the surface roughness of thin film jumps to 2.81 nm. The surface morphology of thin films shows quite high density of the pyramidal-shape terraces with further increases in Bi doping level x = 0.18 to 0.29.

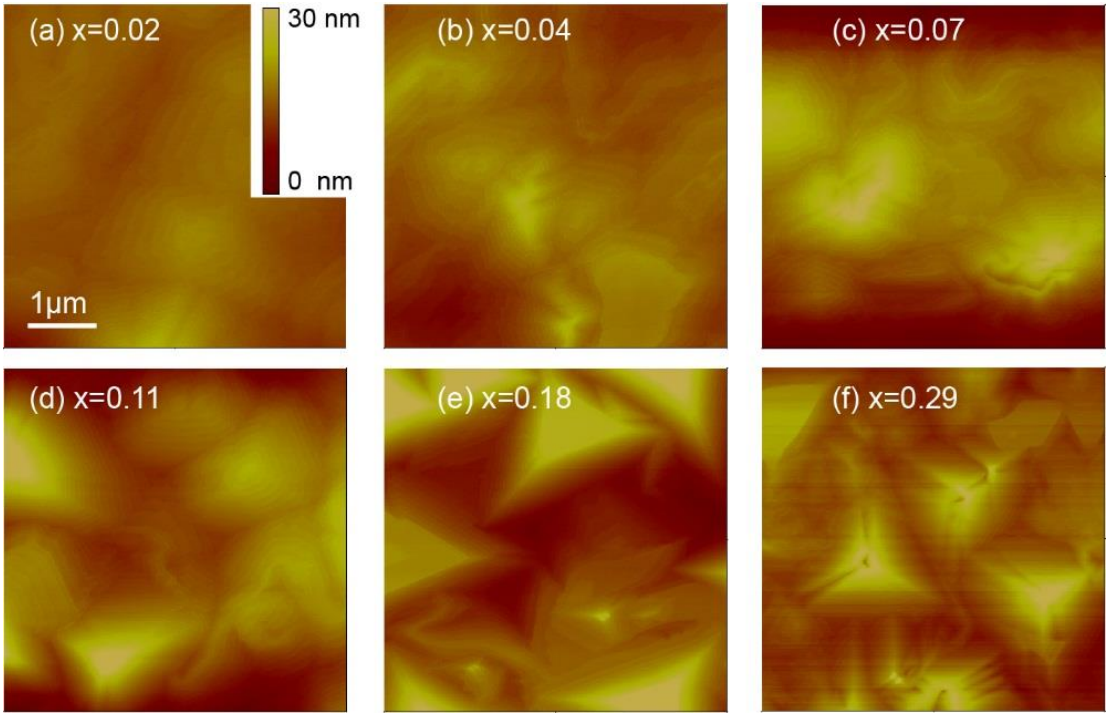

Figure 3.8(a) ~ (f) AFM images of $(Sb_{1-x}Bi_x)_2Te_3$ thin film as a function of Bi concentration x. Large amount of pyramidal-shape terraces over ten quintuple layers can be observed when x > 0.11.

3.6 Characterization on Phase Formation of TI

Reflection High-Energy Electron Diffraction (RHEED) is a tool for real-time characterization of surface and crystal structure of thin film. It is frequently found on ultrahigh vacuum systems such as MBE. RHEED patterns result from and contain detailed information about the crystal properties of surface. The typical setup of RHEED is an electron beam impinges onto film surface at a nearly grazing angle and is reflected onto the screen. It is a surface sensitive technique that the high energy electron beam only probe topmost atomic

layers. Therefore, a streaky RHEED pattern indicates single crystal with smooth surface. As the surface becomes rough but still single crystal, the streaks changed to spotty structure results from the scattering of the electrons through the roughness islands or terraces. Figure 3.9 shows a comparison of two Sb_2Te_3 thin film sample with different substrate temperature. The spotty like structure of RHEED pattern [Figure 3.9(a)] indicating a rough surface while the roughness of thin film with streaky like pattern in Figure 3.9(b) shows roughness about 0.5nm. Therefore, the RHEED provides real-time information of thin film quality, hence enables a quick determination of optimized growth parameter.

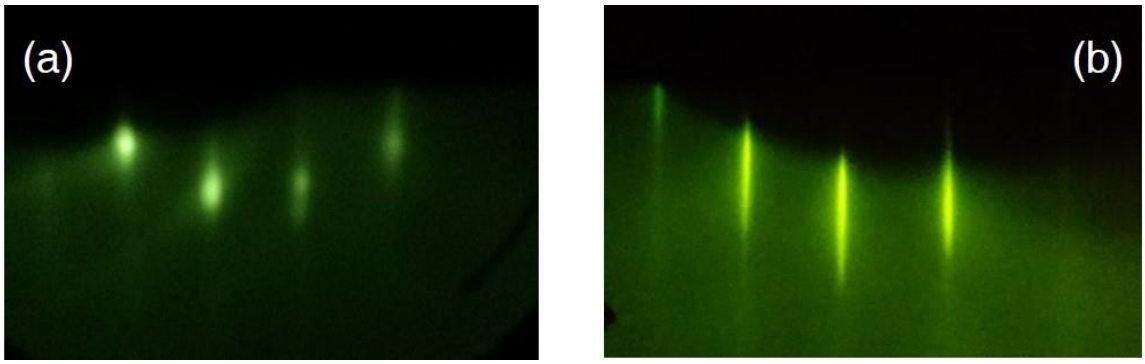

Figure 3.9 Reflection High-Energy Electron Diffraction (RHEED) as real-time tool to monitor the surface of TI thin film

We further use X-ray diffraction method to characterize the crystallographic properties of films. The crystal quality and orientation of deposited Sb_2Te_3 thin film on mica were determined by XRD. It is found that the mica substrate is characterized as sharp (001) family diffraction peaks, which indicates its clave plane as *c*-axis. The (003) family diffraction peaks of Sb_2Te_3 are observed, which suggests that the deposited thin films preferentially align alone its *c*-axis. Moreover, no extra peaks are observed indicating that no secondary phase appears. We determined that its *c* lattice parameter is 30.42 Å from the diffraction pattern, being consistent with its bulk value.

CHAPTER 4. MAGNETOTRANSPORT STUDY OF TOPOLOGICAL INSULATOR THIN FILM ON MICA SUBSTRATE

To analyze the exotic surface electronic property of TI thin film, we deposit high quality $(Sb_{1-x}Bi_x)_2Te_3$ thin films on mica substrate by molecular beam epitaxy and investigate their magnetotransport properties. It is found that the average surface roughness of thin films is lower than 2 nm. Moreover, a local maxima on the sheet resistance is obtained with x = 0.043, indicating a minimization of bulk conductivity at this composition. For $(Sb_{0.957}Bi_{0.043})_2Te_3$, weak antilocalization with coefficient of -0.43 is observed, confirming the existence of 2D surface states. Moreover Shubnikov-de Hass oscillation behavior occurs under high magnetic field. The 2D carrier density is then determined as 8.08×10^{16} m^{-2}, which is lower than that of most TIs reported previously, indicating that $(Sb_{0.957}Bi_{0.043})_2Te_3$ is close to ideal TI composition of which the Dirac point and Fermi surface cross within the bulk bandgap. Our results thus demonstrate the best estimated composition for ideal TI as $(Sb_{0.957}Bi_{0.043})_2Te_3$ and will be helpful for designing TI-based devices.

4.1 Introduction

Topological insulators (TIs), due to its dispersionless surface state[14, 19] are promising candidates for nano-electronics, spintronics, and magnetic sensors [15, 61, 62]. The reason for this nontrivial surface state is the bulk band inversion which arises from the strong spin-orbit coupling [19]. This surface state of TIs protects the electrons from back scattering which may lead to ultra-high conductivity [63]. Experimentally, the topological surface state has been found in 3D TI materials such as Bi_2Te_3 and Sb_2Te_3. To reduce the surface crystalline defect and obtain high bulk resistivity, TIs are grown on various substrates such as sapphire and GaAs.

Among these substrates, muscovite mica which enables van der Waals epitaxy shows advantages in the growth of TI with low crystalline defect and high electrical properties [24]. Moreover, the mechanical flexibility and transparency of mica enable the application of TIs in flexible optoelectronics [64].

The ideal TIs require both Dirac cone and Fermi level lying inside the bulk bandgap where all the electrical conductivities are attributed by the TI surface [19]. However, TIs such as Bi_2Te_3 and Sb_2Te_3 are reported as n-type and p-type band structure respectively [65]. Therefore, their band structures are required engineered to achieve ideal TI. Due to the structural compatibility of Bi_2Te_3 and Sb_2Te_3, it is possible to tune the Fermi level and Dirac cone by doping Bi into Sb_2Te_3 to make an ideal TI. Moreover, since the band structure of TIs can be affected by the epitaxial constraint from the substrate [66], it is still necessary to study the growth of $(Sb_{1-x}Bi_x)_2Te_3$ on mica substrate and experimentally locate the ideal TI composition for the practical applications.

In this chapter, $(Sb_{1-x}Bi_x)_2Te_3$ thin films were deposited on mica substrate with varying Bi concentration, aiming to study the structural characterize of thin films on mica substrate and locate the ideal TI composition. The magneto transport responses of $(Sb_{1-x}Bi_x)_2Te_3$ near ideal TI composition will be studied in detail to understand the electron properties of its surface state.

4.2 Experiment

$(Sb_{1-x}Bi_x)_2Te_3$ thin films with thickness of 12 nm were deposited on mica substrate by molecular beam epitaxy. The quality of the thin films during growth was monitored with reflection high energy electron diffraction (RHEED). The concentration of Bi in $(Sb_{1-x}Bi_x)_2Te_3$ thin films was modulated by the cell temperature of Bi. X-ray diffractometer (XRD) were used to characterize structural information thin films. The surface morphology and thickness of thin

films were characterized by atomic force microscope (AFM). The composition of thin films was analyzed with the FEI Quanta FE-SEM. Room temperature sheet resistance of thin films was measured using four-point probe method. The magnetotransport response of thin film at low temperature was performed in physical properties measurement system.

4.3 Results and Discussion

4.3.1 Structure of $(Sb_{1-x}Bi_x)_2Te_3$ thin films deposited on mica substrate

Surface morphology of Sb_2Te_3 thin film grown on mica is shown in Figure 4.1(a). Over large length scale (5×5 μm^2), the thin film possesses a terrace-like structure. Along dashed line of Fig. 1(a), the surface shows stepwise increase of its height [Figure 4.1(e)] with a value of ~ 1 nm (i.e. one quintuple layer)[60] which indicates the 2D growth of thin films on mica substrate. With doping Bi into Sb_2Te_3 [Figure 4.1(b), 1(c), and 1(d)], pyramidal-shape terrace gradually appears. As a result, the surface roughness increases. The highest surface roughness is ~ 1.9 nm with x = 0.07. However, this value is still low when compared with TIs grown on substrates such as InP (111) and GaAs (111) (roughness ~ 8 nm) [59, 60], which demonstrates the feasibility of mica substrate on growth of $(Sb_{1-x}Bi_x)_2Te_3$ with varying Bi concentration. Representative XRD profile of $(Sb_{1-x}Bi_x)_2Te_3$ with x = 0.043 is shown in Figure 4.1(f). Diffraction peaks from the [55] family planes of $(Sb_{0.957}Bi_{0.043})_2Te_3$ are observed, which suggests that thin films are grown along its *c*-axis.

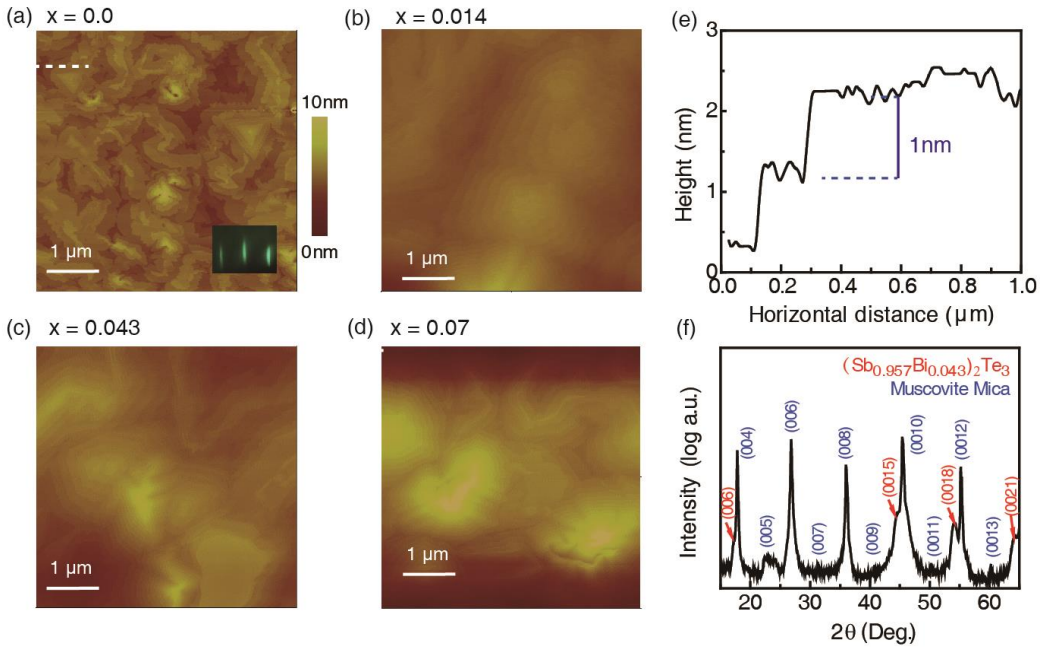

Figure 4.1 Characterization of topological insulator thin films (a) ~ (d) AFM image of thin films $(Sb_{1-x}Bi_x)_2Te_3$ grown on mica substrate, where (a) x = 0.0, (b) x = 0.014, (c) x = 0.043, and (d) x = 0.07. RHEED pattern of thin film (Sb_2Te_3) during growth is shown in (a) inset. (e) Height profile of Sb_2Te_3 thin film along the dashed line in (a). (c) XRD profile of $(Sb_{1-x}Bi_x)_2Te_3$ thin film with x = 0.043.

4.3.2 Effect of Bi on sheet resistivity of $(Sb_{1-x}Bi_x)_2Te_3$ thin films

To locate the ideal TI composition in $(Sb_{1-x}Bi_x)_2Te_3$ grown on mica substrate, sheet resistivity of thin films were studied. Based on previous results [67] for Sb_2Te_3 [Figure 4.2(a1)], the DP locates in the bulk bandgap while the FL lies in the valence band; while for Bi_2Te_3 [Figure 4.2(a3)], the DP is inside the valence band with FL cutting the conduction band. The band structure of Sb_2Te_3 and Bi_2Te_3 thus suggest a low value of their sheet resistivity. Doping of Bi gradually shifts up the FL and pushes down the DP [67]. As a result, an ideal TI with FL and DP cross within the bulk bandgap can be formed [Figure 4.2(a2)]. With extremely reducing bulk carrier density, the $(Sb_{1-x}Bi_x)_2Te_3$ near ideal TI should show obvious increase in sheet

resistivity [67]. Moreover, the energy difference between DP and FL of Sb_2Te_3 (~ 0.01 eV) is much smaller than that of Bi_2Te_3 (~ 0.3 eV) [67]. Thus, the ideal TI composition is expected close to Sb_2Te_3 terminal. Based on above analysis, sheet resistance measurement was performed on $(Sb_{1-x}Bi_x)_2Te_3$ with x = 0.014, 0.043, and 0.07 at room temperature. As Figure 4.2(b) shows, with doping Bi, a peak in sheet resistivity is observed in $(Sb_{1-x}Bi_x)_2Te_3$ at x = 0.043. The sheet resistivity decreases with deviating from this composition. Such experimental observation is consistent with the schematic picture in Figure 4.2(a1) ~ 2(a3). It is indicated that $(Sb_{1-x}Bi_x)_2Te_3$ with x = 0.043 is close to ideal TI. This doping value is also consistent with previous work suggesting the ideal TI composition as x = 0.04 ~ 0.06 [67], indicating that epitaxial constraint generated by mica substrate is weak on determining the composition of ideal TI in $(Sb_{1-x}Bi_x)_2Te_3$.

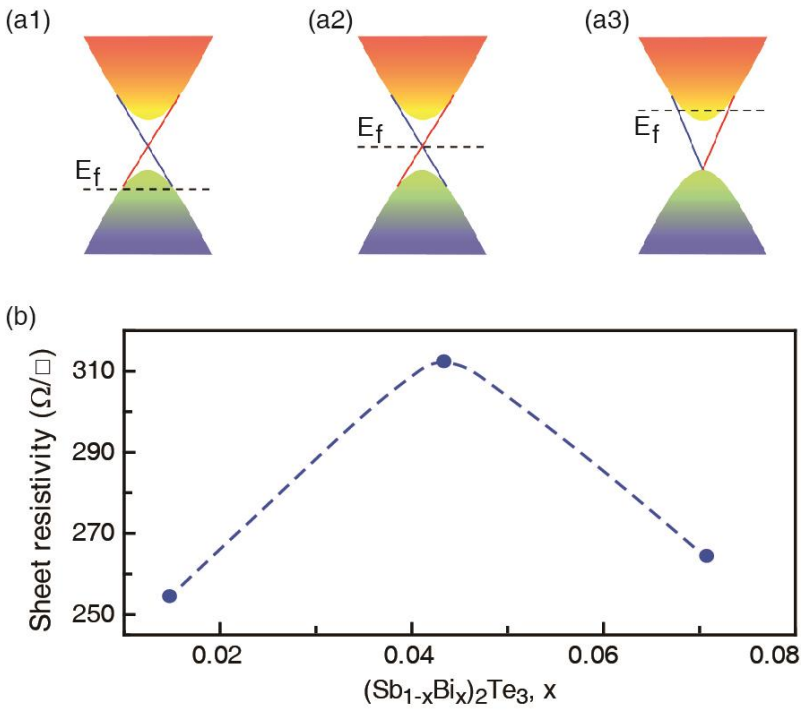

Figure 4.2 (a1) ~ (a3) Schematic illustrations on tuning the Fermi level and surface Dirac point of $(Sb_{1-x}Bi_x)_2Te_3$ with increasing Bi concentration. (b) Sheet resistivity of $(Sb_{1-x}Bi_x)_2Te_3$ thin films at room temperature.

4.3.3 Weak antilocalization of $(Sb_{0.957}Bi_{0.043})_2Te_3$ thin films under low magnetic field

To study the topological surface state near ideal TI composition, magnetotransport responses of $(Sb_{1-x}Bi_x)_2Te_3$ (x = 0.043) at low temperature were studied under low magnetic field. At T = 2.5 K [Figure 4.3(a)], $\Delta G_{xx}(B)$ shows sharp upward cusps shape near zero magnetic field, demonstrating a weak antilocalization effect (WAL) [24, 68, 69]. Such behavior originated from the suppression of deconstructive interference of π Berry's phase with applying magnetic field provide a clear signature on the existence of topological surface state [69]. At T = 7.5 K and 10 K, the WAL is weakening indicating the decrease of phase coherence length with increasing thermal noise.

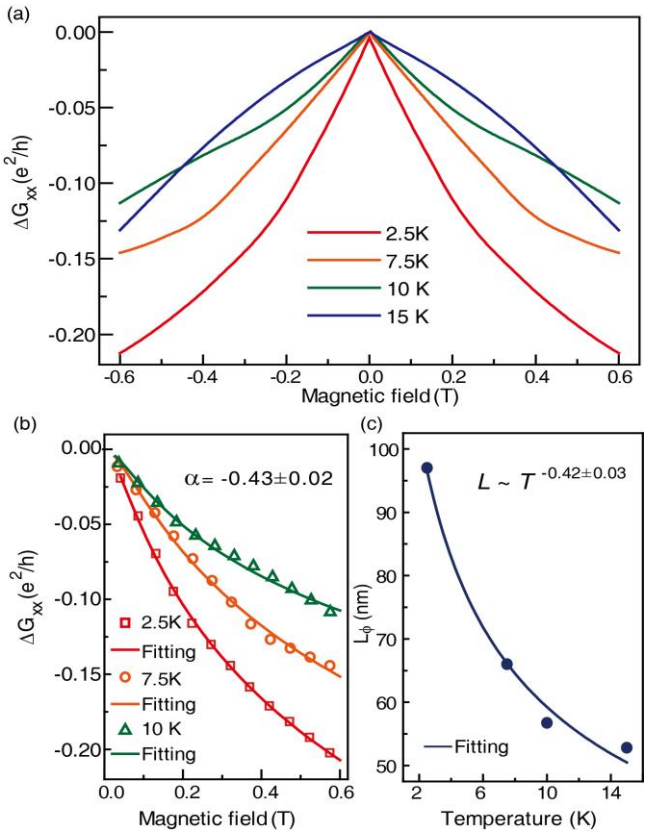

Figure 4.3 (a) Magnetoconductance of $(Sb_{1-x}Bi_x)_2Te_3$ with x = 0.043 at low magnetic field. (b) Fitting of conductance change with Hikami-Larkin-Nagaoka (*HLN*) model. (c) Phase coherence length as a function of temperature, fitted with power law $L_\Phi \sim T^{\beta}$.

The WAL of TI can be described with Hikami-Larkin-Nagaoka (*HLN*) equation as $\Delta G(B)=-(\alpha e^2/\pi h)\bullet[\Psi(0.5+h/8e\pi L_\Phi^2)-\ln(h/8e\pi L_\Phi^2)]$, where α is WAL coefficient, e is electron charge, h is Planck's constant, Ψ is digamma function, and L_Φ is phase coherence length[70]. The best fitting at various temperature [Figure 4.3(b)] yields α = -0.43, confirming the 2D character of WAL since theoretically α should equal to -0.5 for 2D surface state[71]. Figure 4.3(c) shows that the L_Φ decreases from 97 nm to 53 nm with increasing temperature. The temperature dependent of L_Φ is further fitted with a power law $L_\Phi \sim T^\beta$ with β = -0.42. Since β is equal to -1/2 for 2D electron system[72], the present WAL result confirms the existence of 2D topological surface state in $(Sb_{1-x}Bi_x)_2Te_3$ (x = 0.043) thin films deposited on mica substrate.

4.3.4 Quantum oscillation of $(Sb_{0.957}Bi_{0.043})_2Te_3$ thin films under high magnetic field

To study the surface state near ideal TI composition in detail, magnetotransport responses of $(Sb_{0.957}Bi_{0.043})_2Te_3$ were further studied under high magnetic field. As shown in Figure 4.4(a), Hall resistance of sample demonstrates obvious Shubnikov-de Hass (SdH) oscillation at 2.5 K [63]. The dR_{xy}/dB shows periodical oscillations with $1/B$ [Figure 4.4(a) inset]. The oscillation frequency is extracted by fast Fourier transform as F_{SdH} = 33.3 T. The oscillation frequency is related with the area of Fermi surface A_F as $F_{SdH} = [h/4\pi^2 e]A_F$. Assuming a circular area, the Fermi surface can be expressed as $A_F = \pi k_F^2$, where k_F is Fermi vector [63, 73]. The 2D carrier density n_{2D} can then be determined as $n_{2D} = k_F^2/4\pi$ [73]. For $(Sb_{0.957}Bi_{0.043})_2Te_3$, the Fermi vector and 2D carrier density are calculated as k_F=3.18×10^8 m^{-1} and n_{2D}=0.81×10^{16} m^{-2}. SdH oscillation is also observed in normalized magnetoconductance [Figure 4.4(b)], of which the amplitude decreases with increasing temperature [Figure 4.4 (c)].

The temperature dependence of oscillation amplitude can be described by Lifshitz-Kosevich (LK) model as $\Delta\sigma_{xx}(T)= \sigma_{xx}(0)\bullet\lambda(T)/\sinh[\lambda(T)]$ and $\lambda(T)=2\pi^2 k_B T m_{cyc}/(\hbar eB)$ where

m_{cyc} is cyclotron mass [63]. The effective cyclotron mass is obtained as m_{cyc}= 0.086 m_e, where m_e is mass of free electron. Compared with the surface state reported previously (for Bi_2Te_3, n_{2D}~1.2×10^{16} m^{-2}, k_F ~ 4×10^8 m^{-1} , and m_{cyc} ~ 0.15 m_e),[24] the 2D carrier density, cyclotron mass, and Fermi vector of $(Sb_{1.96}Bi_{0.04})_2Te_3$ thin film show lower values. It is indicated that the relative position between Dirac point and Fermi surface are close, being consistent with Figure 4.2(b). Our results therefore demonstrate that $(Sb_{1-x}Bi_x)_2Te_3$ with x = 0.043 grown on mica substrate approach the ideal TI [Figure 4.2(a2)].

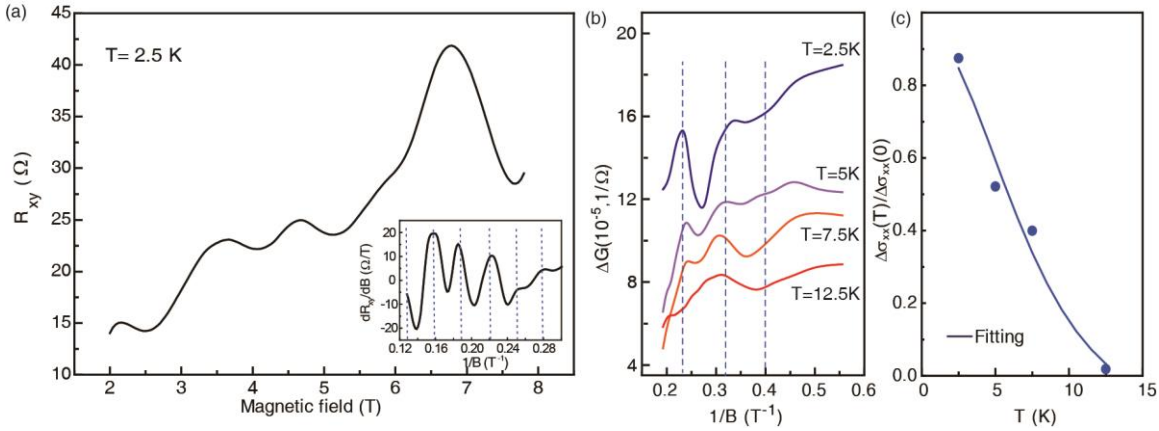

Figure 4.4 (a) Shubnikov-de Hass (SdH) oscillation of Hall resistance for $(Sb_{1-x}Bi_x)_2Te_3$ with x = 0.043 at 2.5 K. Inset shows the periodical oscillation of dR_{xy}/dB with $1/B$. (c) SdH oscillation behavior of its magnetoconductance as various temperatures. (d) Normalized conductivity amplitude, fitted with Lifshitz-Kosevich (LK) model.

4.4 Conclusion

In this work, high quality epitaxial $(Sb_{1-x}Bi_x)_2Te_3$ thin films with 0 < x < 0.07 were grown on mica substrate successfully. The surface roughness of the thin films increases with doping Bi, but keep lower than 2 nm. When Bi concentration is x = 0.043, the sheet resistance shows a local peak, indicating that it is close to ideal TI composition. Weak antilocalization effect with coefficient of -0.43 and phase coherence length of > 70 nm is observed when the

temperature is lower than 10 K, confirming the existence of 2D surface state. Under high magnetic field, $(Sb_{1-x}Bi_x)_2Te_3$ with x = 0.043 demonstrates clear Shubnikov-de Hass (SdH) oscillation behaviors and shows a low value of 2D carrier density, cyclotron mass, and Fermi vector. Our results thus demonstrate that the relative position between Dirac point and Fermi surface are close in $(Sb_{1-x}Bi_x)_2Te_3$ with x = 0.043 on mica substrate. Our results on growth of $(Sb_{1-x}Bi_x)_2Te_3$ thin film and location of ideal TI composition will be helpful for the application of TIs in flexible optoelectronics, spintronics, and magnetic sensors.

CHAPTER 5. STUDY ON MAGNETICALLY DOPED TOPOLOGICAL INSULATOR

As stated in the previous chapters, ferromagnetic phase can be introduced by using element doping in topological insulators. This time-reversal symmetry breaking process allows the formation of an energy gap on the surface state. Therefore, it is interesting to investigate the effect of magnetic dopants in TI thin films. In this chapter, we systematically investigated the effect of magnetic doping on magnetic and transport response of Bi_2Te_3 thin films. $Cr_xBi_{2-x}Te_3$ thin films with x=0.03, 0.14, and 0.29 were grown epitaxially on mica substrate with low surface roughness (~ 0.4 nm). It is found that Cr is a n-type doping element in Bi_2Te_3, and increases the magnetic response of $Cr_xBi_{2-x}Te_3$. When x=0.14 and 0.29, long range ferromagnetism appears in $Cr_xBi_{2-x}Te_3$ thin films, where anomalous Hall effect and weak localization of magnetoconductance were observed. The ferromagnetic transition temperature, coercive field, and remnant Hall resistance of thin films increase with increasing Cr concentration. The Arrott-Noakes plot for $Cr_xBi_{2-x}Te_3$ demonstrate that the critical mechanism of the ferromagnetism can be described better with 3D-Heisenberg model than with mean field model. Our work may benefit for the practical applications of ferromagnetic TI with opened surface band gap in spintronics and magnetoelectric devices.

5.1 Introduction

Topological insulators (TIs) with gapless surface state attract attentions both for fundamental science and potential applications. The reason of this nontrivial surface state is their bulk band inversion and massless Dirac-cone-like surface state arising from the strong spin-orbit coupling [19]. This surface state is protected by the time reversal symmetry which

prohibits the backscattering on non-magnetic impurities, and induces a weak antilocalization of Dirac fermions [74].

The surface state of TIs protected by time reversal symmetry can be broken by a proximity effect with interfacing an insulating ferromagnetic material or introducing magnetic impurities [75, 76]. Consequently, magnetic impurities in TIs can cause the opening of the surface band gap which can induce phenomena such as the quantized anomalous Hall effect and magnetoelectric effect [16, 77]. Due to the magnetic doping, it is shown that a weak localization (WL) behavior emerges and competes with the weak antilocalization effect (WAL) [78]. Theoretically, introducing of transition metal ions can lead to ferromagnetism by either Van Vleck mechanism or Ruderman-Kittel-Kasuya-Yosida (RKKY) exchange mechanism [20, 76, 79]. However, the critical property of ferromagnetism in magnetic TIs is not well studied. Moreover, introducing magnetic impurities may roughen the surface of thin films and result in an increasing of carrier concentration, which prohibits the appearance of quantized anomalous Hall state [80]. Thus, to realize practical applications of the nontrivial state in TIs, extensive understanding of magnetically doped TIs is still required.

In this chapter, we report the effect of magnetic impurity on manipulating the magnetic and transport response of $Cr_xBi_{2-x}Te_3$ thin films with low surface roughness. We will show that Cr atoms increase the magnetization and establish ferromagnetism in $Cr_xBi_{2-x}Te_3$ thin films. Moreover, the Arrott and Arrott-Noakes plot [81, 82] for $Cr_xBi_{2-x}Te_3$ indicate that the critical mechanism of ferromagnetism in $Cr_xBi_{2-x}Te_3$ can be described better with 3D-Heisenberg model than mean field model.

5.2. Experiments

$Cr_xBi_{2-x}Te_3$ thin films were grown on mica substrate using molecular beam epitaxy with base pressure as ~ 5×10^{-10} Torr. The temperature of Bi and Te source materials was adjusted to obtain a Te-rich environment. The growth rate was kept as 0.3 nm/min. The surface topography of the thin films was characterized by atomic force microscope (AFM). Root mean square (RMS) surface roughness was then quantitatively calculated. Thin films with thickness of 12 nm were deposited. The thickness was determined by measuring the height of a scratch made carefully on thin films with AFM in tapping mode [83]. The composition analysis was carried out at the FEI Quanta FE-SEM. The magnetic property measurement was performed using a SQUID magnetometer. The thin film was fabricated into 1 mm wide Hall bar geometry by plasma etching. The transverse and longitudinal resistances under applied magnetic field were measured with physical properties measurement system. The applied AC current was 0.01 mA, with the frequency as 19 Hz.

5.3. Results and Discussion

5.3 1 Structural characterization of $Cr_xBi_{2-x}Te_3$ thin films

The surface morphology of $Cr_xBi_{2-x}Te_3$ with x = 0.00, 0.14, and 0.29 are shown in Figure 5.1(a). Without doping Cr, the Bi_2Te_3 shows large scale terraces. The height of a terrace is ~ 1 nm (i.e. one quintuple layer of Bi_2Te_3). When x = 0.14 and 0.29, large scale terraces cannot be found. The surface morphology of thin films changes with an obvious reduction of terrace width, which may due to the competition between Bi atoms and Cr atoms at Bi site.[84] Although the width of terraces decreases with doping Cr, layer-by-layer epitaxial growth of thin films remains. Based on the AFM images, we calculated the surface RMS roughness of

thin films. As Figure 5.1(b) shows, a low surface roughness for all samples (~ 0.4 nm) is found. The roughening of the flat surface with doping Cr reported previously[80] is not observed in the present thin films, which may result from a low growth rate here.

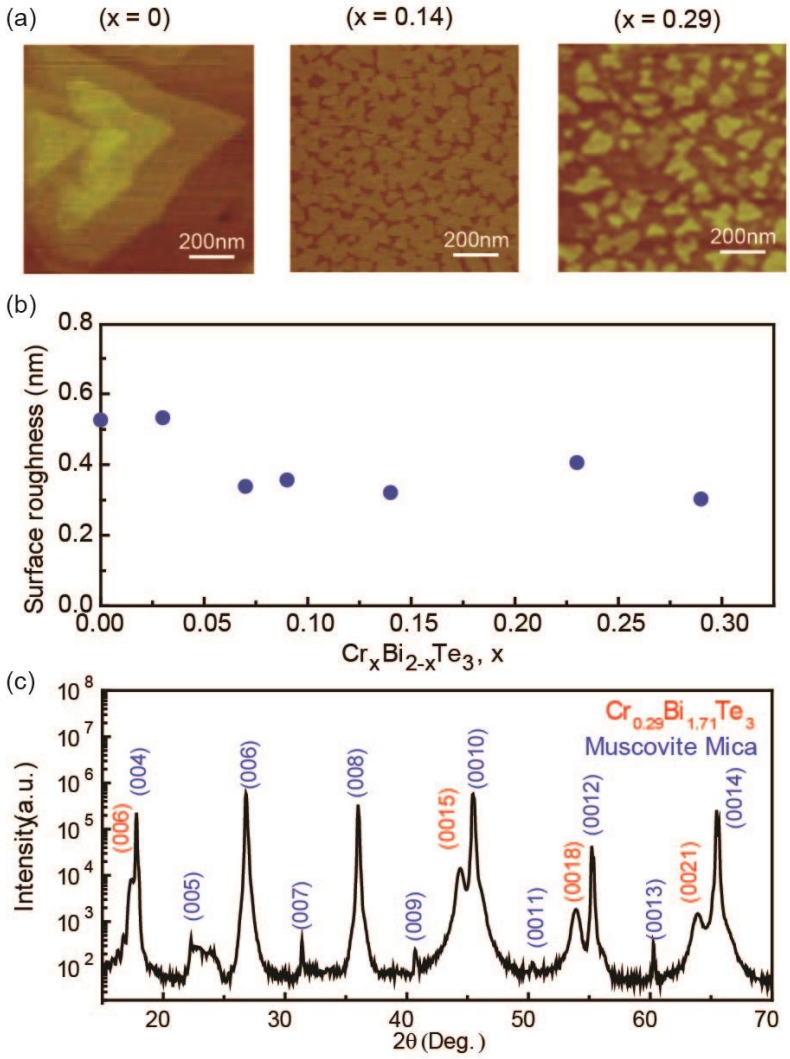

Figure 5.1 Structural characterization of $Cr_xBi_{2-x}Te_3$ thin films. (a) AFM images of $Cr_xBi_{2-x}Te_3$, with x = 0.00, 0.14, and 0.29. (b) Surface RMS roughness as a function of Cr concentration in $Cr_xBi_{2-x}Te_3$. (c) XRD pattern of $Cr_xBi_{2-x}Te_3$ with x = 0.29 grown on mica substrate

The crystal quality and orientation of thin films were studied by x-ray diffractometer (XRD). Figure 5.1(c) shows the XRD spectrum of $Cr_xBi_{2-x}Te_3$ with x= 0.29. The mica substrate

is characterized as [85]amily diffraction peaks, indicating its cleavage plane as the *c*-axis. The diffraction peaks from family of the [55] planes of $Cr_xBi_{2-x}Te_3$ are observed, which suggests the thin films preferentially align along their *c*-axis. From the diffraction pattern for $Cr_xBi_{2-x}Te_3$ with x=0.29, we determine that its *c*-axis lattice parameter is 30.59 Å, which is higher than that of Bi_2Te_3 (30.49 Å in *c*-axis lattice parameter with interlayer spacing as 2.56 Å) [86]. Because the ionic radius of Cr is smaller than that of Bi, the increase of *c*-axis lattice parameter indicates that Cr not only substitutes Bi atoms but also locates in the Van der Waals gaps between quintuple layers, which is similar to the doping mechanism of Cu in Bi_2Se_3 [87].

5.3.2 Magnetization of $Cr_xBi_{2-x}Te_3$ thin films

To investigate the magnetic properties of $Cr_xBi_{2-x}Te_3$, the out-of-plane magnetic moment of the thin films with surface area as 0.0789 cm^2 were measured. As Figure 5.2(a) shows, when x = 0.03, the magnetization of the thin film keeps as negative during cooling, indicating that the Bi_2Te_3 with slightly Cr doping is still a diamagnetic material. When x = 0.14, the magnetization of the thin film increases. Its value becomes positive. Moreover, the magnetization of the thin film increases with cooling below ~ 25 K. The saturation of magnetization with further cooling is not observed. $Cr_xBi_{2-x}Te_3$ with x = 0.29 shows higher magnetization in the whole temperature window. The magnetization of the thin film starts to increase below ~ 50 K. The increase of the magnetization with increasing Cr concentration indicates that the magnetic moment of the samples are easier to be polarized out-of-plane, which is similar to previous report on Fe-doped Bi_2Se_3 that the *c*-axis is the magnetic easy axis [88].

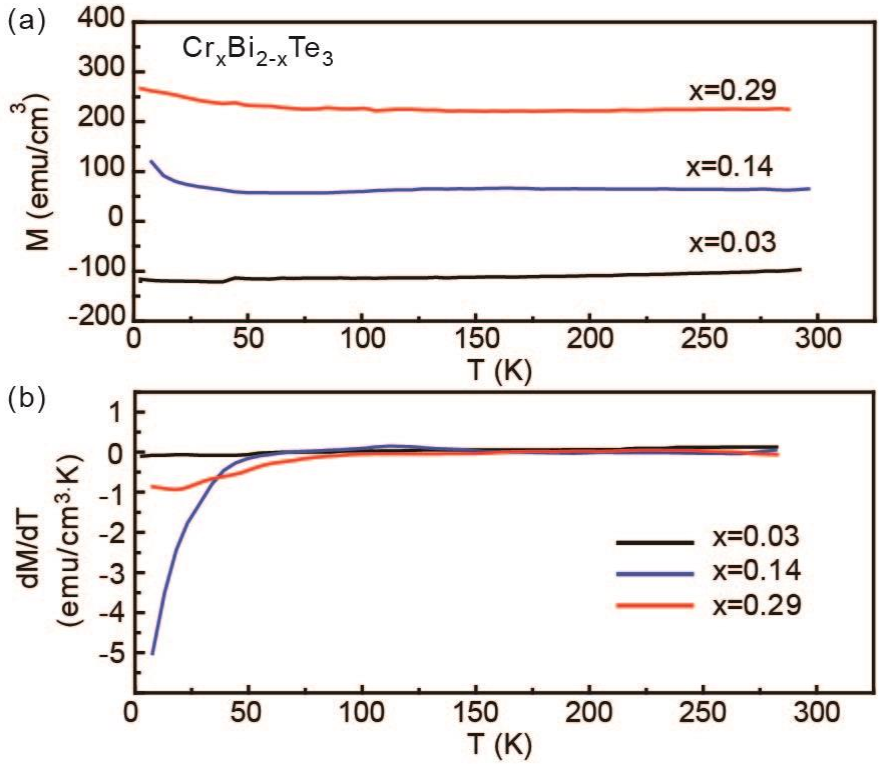

Figure 5.2 (a) The temperature dependence of magnetization under 0.05 T for $Cr_xBi_{2-x}Te_3$ with x=0.03, 0.14, and 0.29. (b) The corresponding d*M*/d*T* vs. *T* curves.

The d*M*/d*T* - temperature curves of samples are shown in Figure 5.2(b). It is found that the temperature where the d*M*/d*T* curve starts to deviate from linear one increases with increasing Cr concentration. Moreover, the d*M*/d*T* ~ *T* curve for x=0.29 shows a small peak at ~ 20 K, indicating that there may be a magnetic transition. However, due to the low net magnetic moment of the samples and the thin film effect [89], this peak is not measured as clearly as it should be in bulk ferromagnetic materials; and the behavior of magnetization above the peak temperature deviates from that of a paramagnet. As a result, the existence of ferromagnetism in $Cr_xBi_{2-x}Te_3$ is difficult to be concluded here. In the following section, we investigate the magnetic properties of $Cr_xBi_{2-x}Te_3$ by measuring the magnetic field dependence of electrical transport properties [90, 91].

5.3.3 Electrical transport and anomalous Hall effect of $Cr_xBi_{2-x}Te_3$ thin films

The Hall resistance and magnetoconductance (MC) of $Cr_xBi_{2-x}Te_3$ are shown in Figure 5.3. As Figure 5.3(b1) shows, when x=0.03 the WAL behavior of MC cannot be observed. Instead, a WL behavior is shown at 2.5 K. By heating up to 7.5 K, the WL behavior changes into a classical parabolic dependence of magnetic field without observing the WAL, indicating the dominance of WL behavior. Moreover, when x=0.03, Hall resistance does not show any hysteresis with magnetic field.

With increasing the Cr concentration, features of ferromagnetism are observed. As shown in Figure 5.3(a2) and (a3), the Hall resistance of $Cr_xBi_{2-x}Te_3$ with x=0.14 and 0.29 shows hysteretic behavior resulting from the anomalous Hall effect, suggesting an occurrence of magnetic ordering. As in regular ferromagnetism, the coercive field and remnant Hall resistance increase with cooling. With increasing Cr, higher coercive field and remnant Hall resistances are observed; the hysteresis of Hall resistance also vanishes at a higher temperature. It is indicated that with increasing Cr concentration, ferromagnetism in $Cr_xBi_{2-x}Te_3$ is stabilized; and enhanced anomalous Hall effect can be obtained.

The MC of $Cr_xBi_{2-x}Te_3$ with x= 0.14 and 0.29 consistently show the appearance of ferromagnetism in thin films. As Figure 5.3(b2) and (b3) show, the MC of $Cr_xBi_{2-x}Te_3$ with x=0.14 and 0.29 shows WL behavior at 2.5 K as a non-monotonic increase of MC with increasing magnetic field. Moreover, the hysteresis loop of MC shows a butterfly shape, indicating the existence of ferromagnetism. Even though it is important to directly measure the hysteresis loop of magnetization with applied magnetic field to further confirm the ferromagnetism in thin films, we have verified by both MC and Hall resistance that ferromagnetism is established in $Cr_xBi_{2-x}Te_3$ with x=0.14 and 0.29.

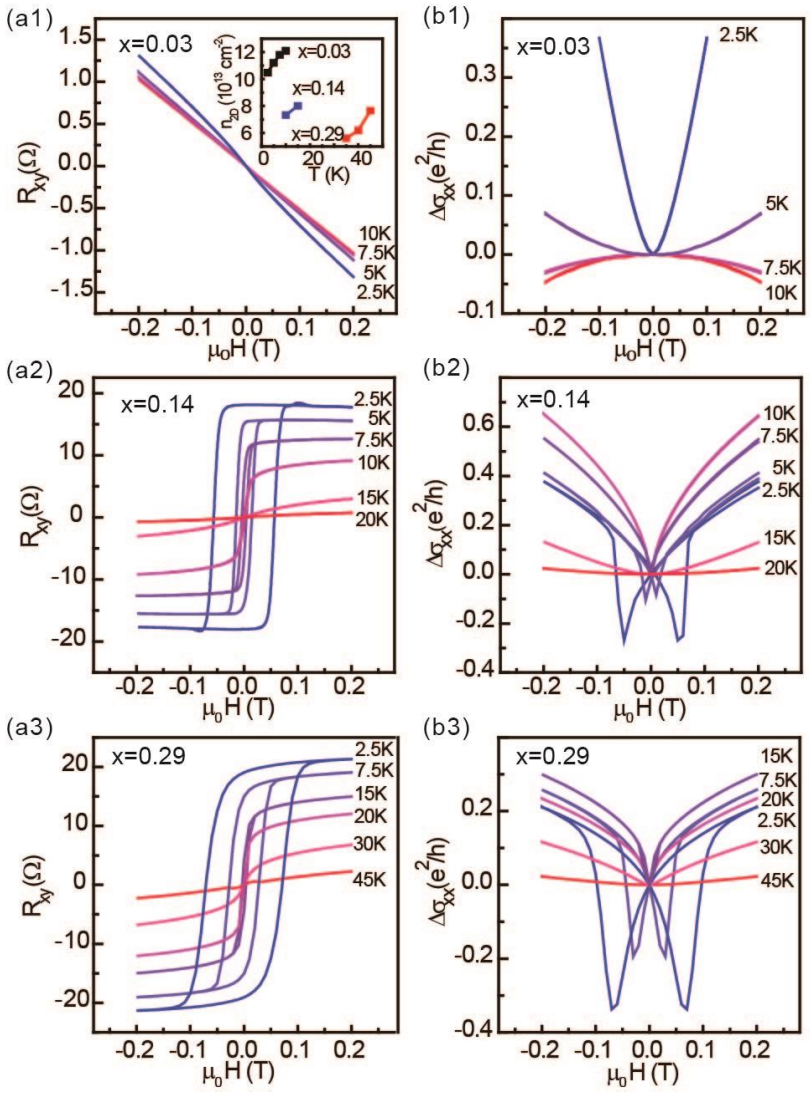

Figure 5.3 (a1), (a2), and (a3) Hall resistance curves at low magnetic field for $Cr_xBi_{2-x}Te_3$ with x = 0.03, 0.14, and 0.29 respectively. (b1), (b2), and (b3) Corresponding normalized magnetoconductance curves. The temperature dependent carrier concentration of $Cr_xBi_{2-x}Te_3$ is shown in (a1) inset.

Comparing Figure 5.3(a1), (a2), and (a3), the sign of Hall coefficient changes with incorporating Cr in Bi_2Te_3. For $Cr_xBi_{2-x}Te_3$ with x=0.03, Hall coefficient shows a p-type conductivity. When x=0.14 and 0.29, the sign of Hall coefficient becomes positive demonstrating an n-type conductivity, indicating the Cr is an electron donor in Bi_2Te_3. We extracted the carrier concentration using Hall coefficient $|R_H|=1/en$ by examining the Hall

resistivity at large field where the relation between resistivity and field is linear, where *e* is the electron charge and *n* is the carrier concentration. As Figure 5.3(a1) inset shows, carrier concentration of $Cr_xBi_{2-x}Te_3$ decreases with introducing Cr, indicating that Cr reduces free carriers of p-type Bi_2Te_3. The increasing of carrier concentration by doping Cr in samples with high surface roughness (~1 nm) [80] is not observed in this work, suggesting that the growth of low surface roughness samples helps to reduce the bulk carrier concentration.

5.3.4 Critical property of the ferromagnetism in $Cr_xBi_{2-x}Te_3$ thin films

The critical property of the ferromagnetism in $Cr_xBi_{2-x}Te_3$ were studied by Arrott plot[81] and Arrott-Noakes plot [82] techniques, where the Curie temperature was also determined. The Arrott plots at various temperatures for $Cr_xBi_{2-x}Te_3$ x = 0.14 and 0.29 were calculated from Figure 5.3(a2) and (a3). As Figure 5.4(a) and (c) show, the R_{xy}^2 is not linear related to $\mu_0 H/R_{xy}$ at high magnetic field, indicating the ferromagnetic transition in heavily doped $Cr_xBi_{2-x}Te_3$ deviates from mean field model. Thus, it is difficult to extract Curie temperature from Arrott plot.

It was predicted that the ferromagnetism in TIs may result from RKKY interaction of magnetic impurities consisting of Heisenberg-like, Ising-like, and Dzyaloshinskii-Moriya-like terms [79]. Thus, we calculated the Arrott-Noakes plot at various temperatures for $Cr_xBi_{2-x}Te_3$ x=0.14 and 0.29 from Figure 5.3(a2) and (a3) by assuming β = 0.36 and γ = 1.386 (3D-Heisenberg model). As Figure 5.4(d) shows, the $R_{xy}^{1/\beta}$ remains almost linear with respect to $(\mu_0 H/ R_{xy})^{1/\gamma}$ close to 22.5 K, indicating that the critical mechanism of ferromagnetism in $Cr_xBi_{2-x}Te_3$ can be described better with 3D-Heisenberg model than with mean field model. Based on Arrott-Noakes plot, we extract the Curie temperature of $Cr_xBi_{2-x}Te_3$ with x=0.14 and

x=0.29 as ~12.5 K and ~23.8 K, being consistent with the magnetic measurement shown in Figure 5.2.

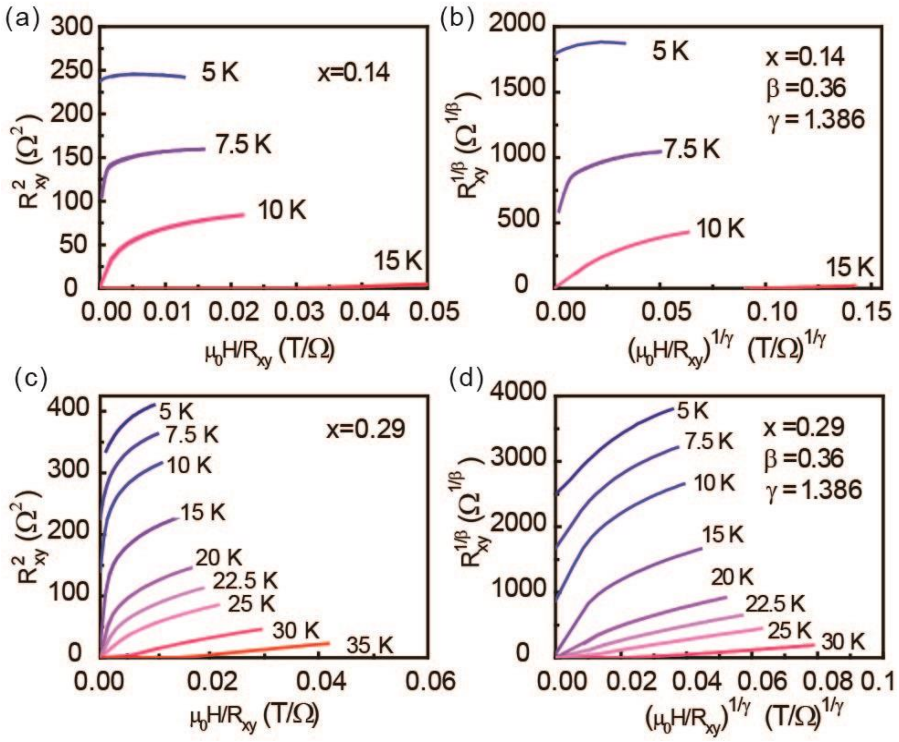

Figure 5.4 (a) and (c) Arrott plot at various temperatures for $Cr_xBi_{2-x}Te_3$ with x= 0.14 and 0.29 respectively. (b) and (d) Arrott-Noakes plot at various temperatures for $Cr_xBi_{2-x}Te_3$ with x= 0.14 and 0.29 respectively, assuming β = 0.36 and γ = 1.386.

5.4 Conclusion

In this work, the effect of magnetic impurities on $Cr_xBi_{2-x}Te_3$ thin films with x=0.03, 0.14, and 0.29 was studied. Thin films with low surface roughness (~0.4 nm) were deposited on mica substrate. We found that Cr is an electron donor which reduces the carrier concentration of Bi_2Te_3. Magnetization of thin films increases with increasing Cr concentration. The ferromagnetism in $Cr_xBi_{2-x}Te_3$ appears at x=0.14 and 0.29, where hysteretic anomalous Hall effect and weak localization of magnetoconductance are observed. Our work

is useful for achieving the gapped surface state of TIs with magnetic doping and their practical applications in magnetoelectric devices.

CHAPTER 6. HALL EFFECT SENSOR BASED ON TOPOLOGICAL INSULATORS

After investigation on unique surface states of TI and magnetic element doped TI in the previous chapters, we begin to design and implement magnetic sensor based on TI thin film. Hall effect (HE) sensor is a widely used and highly sensitive magnetic sensor. Most HE sensor nowadays utilize high carrier mobility semiconductor such as GaAs. However, due to the high resistance of conventional semiconductor, a low energy consumption, high sensitivity Hall sensor are highly demanding. In this chapter, HE sensors based on high quality Mn doped Bi_2Te_3 topological insulator thin films have been systematically. Improvement of Hall sensitivity is found after doping magnetic element Mn into Bi_2Te_3. The sensors with low Mn concentrations, $Mn_xBi_{2-x}Te_3$, x =0.01 and 0.08 show linear behavior of Hall resistance with sensitivity about 5 Ω/T. And their Hall sensitivity shows weak dependence on temperature. For sensors with high Mn concentration (x=0.23), the Hall resistance with respect to magnetic field shows a hysteretic behavior. Moreover, its sensitivity shows almost 8 times as high as that of HE sensors with low Mn concentration. The highest sensitivity can reach 43 Ω/T at very low magnetic field. This increase of Hall sensitivity is caused by the occurrence of anomalous Hall effect (AHE) after ferromagnetic phase transition. Our work indicates that magnetic element doped topological insulator with AHE are good candidates for Hall effect sensors.

6.1 Introduction

Hall effect (HE) sensors are used widely in areas including position sensing, DC current transformers, and fuel level indicator due to their low costs, high reliability, free of contact bounce, and immune to environmental contaminants [92]. However, the low measuring

accuracy and sensitivity comparing to fluxgate magnetometers limit their applications. As a result, improving the sensitivity becomes a crucial problem for HE sensors. Key factors controlling sensitivity as well as the power consumption of HE sensors are carrier density and carrier mobility. Therefore, semiconductors such as GaAs and InAs with higher carrier mobility and lower carrier density than metals are often utilized [93]. In addition, anomalous Hall effect (AHE), which generates extra voltage across the current-carrying magnetic material due to spin-polarized electrons, is also used to make Hall sensors because of its improved Hall sensitivity.

Recently, a new kind of semiconductor was discovered as topological insulators (TIs), which can possess an ultra-high carrier mobility at the surface, while keep insulating in bulk [15]. The reason of high carrier mobility is that TIs have spin-polarized massless Dirac surface state. Such state, protected by time reversal symmetry, suppresses the backscattering of charge carriers upon non-magnetic impurities. Moreover, Fermi level of TIs can be tuned to the surface Dirac point to reduce the density of charge carriers [31]. As a result, the ultrahigh mobility and low density of charge carriers enable TIs suitable materials for developing HE sensors. In addition, introducing magnetic impurities such as Fe [94], Cr [80, 95, 96], and Mn [97-100] into TIs can induce ferromagnetism and open a surface energy gap, which leads to interesting behaviors including magnetoelectric effect and quantized AHE [24]. As a result, TIs can also be considered as good candidates for AHE-based sensors by changing them into magnetic materials through incorporating magnetic impurities.

Bi_2Te_3 has been found as one of 3D TI in the previous experiment work. The surface state of both pure Bi_2Te_3 and Sn doped Bi_2Te_3 were confirmed by ARPES and magneto-transport measurements [4, 17]. Moreover, the AHE of Cr and Mn doped Bi_2Te_3 was reported

in previous researches [7, 11, 14]. However the application and properties of Mn doped Bi_2Te_3 TI as Hall effect sensors are not well studied. In this work, we fabricate Hall effect sensors based on Mn-doped Bi_2Te_3 TI thin films. Both HE and AHE of sensors are systematically studied by varying Mn concentration. The influence of Mn concentration on sensitivity of $Mn_xBi_{2-x}Te_3$ HE sensors will be discussed.

6.2 Experiment

$Mn_xBi_{2-x}Te_3$ thin films with Mn concentration in range from 0 to 0.25 were grown by Perkin-Elmer 430 molecular beam epitaxy (MBE) system on mica substrate. When $x > 0.25$, the Mn doping tends to breakdown the epitaxial growth. Mica substrate was cleaved freshly before depositions. Source materials (Mn, Bi, and Te) with high purity were loaded in Knudsen effusion Cells. The base pressure during growth was kept as ~ 8×10^{-9} Torr. HE sensors were fabricated with two major steps. First, the as-grown thin films were fabricated into 1 mm wide Hall bar geometry [Fig 6.2(d)] by reactive-ion etching method. The composition analysis of sensors was carried out at the FEI Quanta FE-EDX. The Mn concentrations were confirmed and three different Mn doping levels in $Mn_xBi_{2-x}Te_3$ were selected as $x = 0.01$, 0.08 and 0.23. The crystal structure of sensors was studied by X-ray spectrometer (Siemens D500 XRD system). The topography of sensors was characterized by atomic force microscopy (AFM) in a tapping mode. The magneto-transport properties of sensors were characterized in Quantum Design physical properties measurement system.

6.3 Results and Discussion

6.3.1 Crystal structure of $Mn_xBi_{2-x}Te_3$ Hall effect sensors

Figure 6.1 shows the XRD profiles of $Mn_xBi_{2-x}Te_3$ HE sensors. Two sets of diffraction peaks are observed. One set of these diffraction peaks can be indexed as the [85] family plane of mica substrate; while (0015), (0018) and (0021) diffraction peaks are obtained from $Mn_xBi_{2-x}Te_3$ thin films with rhombohedral structure. The visibility of diffraction peaks from mica substrate in all samples is due to the low thickness of thin films (~15 nm) in comparison with the penetration depth of X-rays. This diffraction pattern indicates that mica substrate is cleaved along its *ab* plane, while $Mn_xBi_{2-x}Te_3$ thin film is preferentially deposited along its *c*-axis. Moreover, except {001} family peaks, no extra peaks from $Mn_xBi_{2-x}Te_3$ thin films are observed in three doping levels, indicating that thin films being utilized to fabricate sensors are grown epitaxially and highly orientated. The *c*-axis lattice constant of $Mn_xBi_{2-x}Te_3$ thin films with x = 0.01, calculated from the (0018) diffraction peak in Figure 6.1 (a), is 30.54 Å. Comparing with un-doped Bi_2Te_3 (c = 28.84 Å) [97], the *c* lattice constant of Mn doped thin films increases. Moreover, with Mn concentration increasing to x = 0.23, the *c* lattice constant of $Mn_xBi_{2-x}Te_3$ increases to 30.61 Å. Since the ionic radius of Mn is smaller than Bi, the changes in lattice constant with doping Mn shows that Mn not only substitutes into the Bi site but also is trapped in the Van de Waals gap between quintuple layers [101]. In Figure 6.1 (c), the (0021) diffraction peak of $Mn_xBi_{2-x}Te_3$ with x = 0.23 becomes slightly broad compared with less doped samples. This may also results from the lattice distortions induced by Mn atoms.

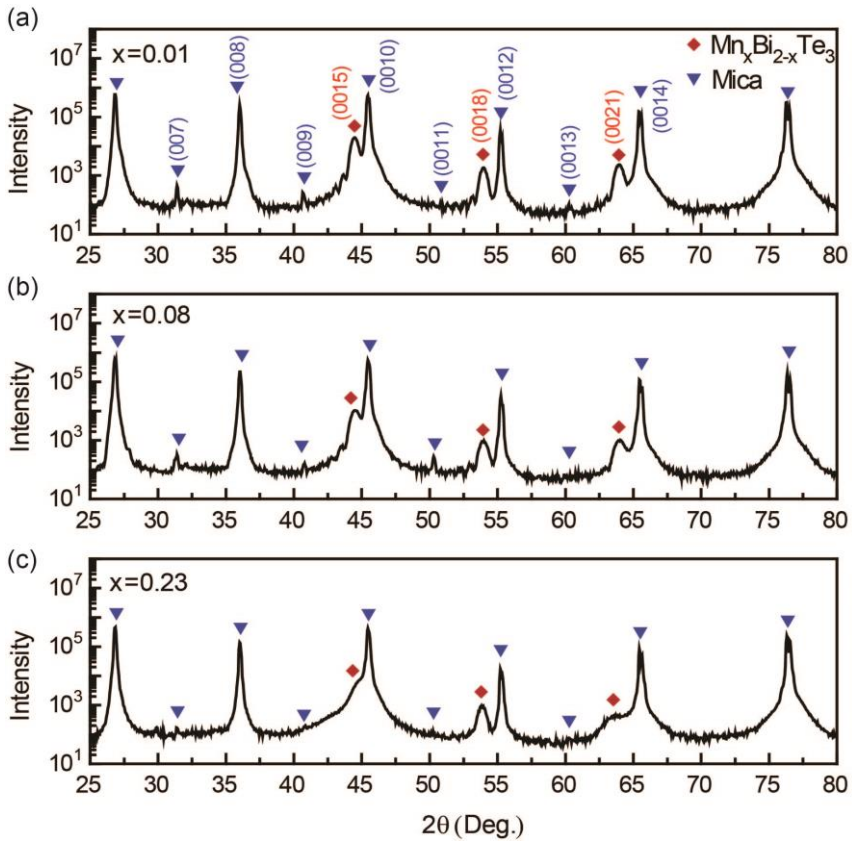

Figure 6.1 X-ray diffraction patterns of $Mn_xBi_{2-x}Te_3$ Hall effect sensor fabricated on mica substrate with (a) x = 0.01, (b) x = 0.08, and (c) x = 0.23, where diffraction peaks from mica substrate and $Mn_xBi_{2-x}Te_3$ thin film are indexed in blue and red, respectively.

6.3.2 Surface morphology of $Mn_xBi_{2-x}Te_3$ and $Cr_xBi_{2-x}Te_3$ Hall effect sensors

Figure 6.2 shows AFM images of $Mn_xBi_{2-x}Te_3$ thin film HE sensors with x = 0.01, 0.08, and 0.23. With low Mn concentration x = 0.01 [Figure 6.2(a)], the sample shows terrace structure with the terrace width range from 200 nm to 500 nm. Moreover, the height of each terrace is ~ 1 nm, which is same as the thickness of one QL of $Mn_xBi_{2-x}Te_3$. These large surface terraces therefore indicate a layer-by-layer growth mechanism of Mn-doped Bi_2Te_3 on mica substrate.

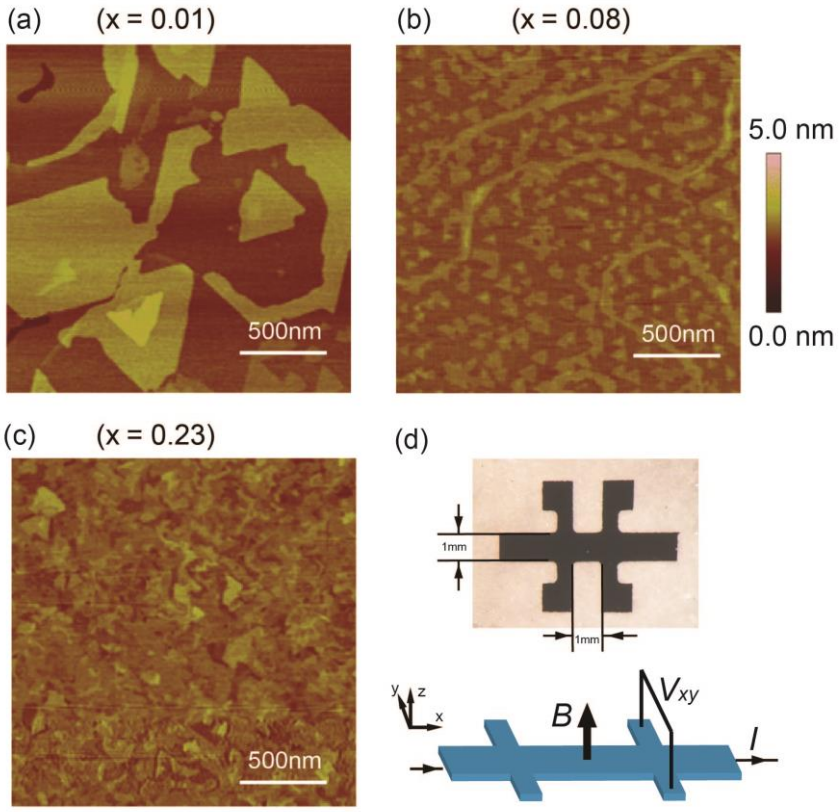

Figure 6.2 (a), (b), and (c) Surface morphology of $Mn_xBi_{2-x}Te_3$ thin films with x= 0.01, x=0.08, and x=0.23, respectively, (d) Hall effect sensor fabricated with $Mn_xBi_{2-x}Te_3$ thin films, and geometry of Hall effect measurement.

With increasing Mn concentration to x = 0.08 and 0.23 [Figure 6.2(b) and (c)], terrace structure still exists. Moreover, streak lines were observed for all samples in the *in-situ* RHEED patterns. It is indicated that thin films with high Mn concentration retain epitaxy. Figure 6.2(a) – (c) further show that with increasing Mn concentration the width of surface terraces decrease. The reducing of surface terrace and slightly roughening of the sensor surface may result from the chemical disorder due to competition of Mn and Bi atoms at Bi site as well as the lattice distortions due to Mn atoms trapped in QL gaps. The root mean square (RMS) surface roughness of sensors shows low values for all samples. The highest RMS roughness of sensors

is 0.2 nm when Mn concentration is x = 0.23, which is much smaller than previous report of Cr doped Bi_2Te_3. The low roughness and high quality of $Mn_xBi_{2-x}Te_3$ thin films consolidates the following results of electric transport properties of sensors.

6.3.3 Electric transport properties of $Mn_xBi_{2-x}Te_3$ and $Cr_xBi_{2-x}Te_3$ Hall effect sensors

The transport responses of $Mn_xBi_{2-x}Te_3$ HE sensors with (x = 0.01, 0.08, 0.23) are shown in Figure 6.3. Hall resistance for all three sensors with different Mn concentration shows tendency of decrease with increasing magnetic field. The negative slope of Hall resistance indicates the Mn doped Bi_2Te_3 sensors remain n-type. The carrier density of sensors at 30 K is calculated by using: $n = (|R_H|e)^{-1}$, where R_H is the Hall coefficient and e is the electron charge. The calculated carrier density decreases from 9.5×10^{19} cm^{-3} to 7.5×10^{19} cm^{-3} at 30 K as Mn concentration increases from x = 0.01 to 0.23, reflecting the downward motion of Fermi level (E_F). The relative large carrier density of sensors compared with ideal TIs indicates that the sensors are heavily donor-doped. As a result, E_F is far above the surface Dirac point. Such band structure is consistent with other TIs such as $Sb_xBi_{2-x}Te_3$ [18]. The carrier mobility of $Mn_xBi_{2-x}Te_3$ sensor was calculated by using: $\mu = {}^{\sigma_{xx}}/_{ne}$, where σ_{xx} is the longitudinal conductivity. The mobility value calculated at 30 K varies with changing Mn concentration. At low doping level (x = 0.01) the carrier mobility is 473.5 cm^2/Vs. The carrier mobility decreases to 72.4 cm^2/Vs in highly doped sensors with x = 0.23. The lower carrier mobility in $Mn_xBi_{2-x}Te_3$ sensors than the reported value in pure Bi_2Te_3 (5800 cm^2/Vs) [83] indicates that the incorporation of Mn destroys the massless surface state of topological insulators. We will show in the following that AHE is also induced in heavily doped $Mn_xBi_{2-x}Te_3$.

At low doping level with x = 0.01 [Figure 6.3(a)], the sensor shows ordinary HE. The overlap of straight lines of Hall resistance at different temperatures indicates the temperature

independence of HE for this composition. For the sensor with Mn concentration x = 0.23 [Figure 6.3(c)], temperature dependence of Hall resistance becomes more obvious than others, and AHE occurs during cooling. At high temperature, Hall resistance shows linear dependence on magnetic field same as previous sample. However, the Hall resistance exhibits hysteresis when the temperature is lower than 12.5 K, indicating the occurrence of a ferromagnetic phase transition [102]. Simultaneously, the Hall resistance of sensors under magnetic field of – 0.2 T increases. Moreover, the hysteresis in Hall resistance increases with further cooling, being similar to the temperature dependence of ferromagnetic materials [103]. The corresponding coercive field H_c as a function of temperature is shown in Figure 6.3(d). H_c abruptly increase around 12.5 K indicating that the ferromagnetic transition temperature T_c of sensors is near 12.5 K, which is in the same temperature range as previous researches [99, 100]. The temperature dependence of longitudinal resistance (R/R_{30K}) of sensors at various Mn concentrations is further depicted in the inset of Figure 6.3(d). Typical metallic behavior can be observed for x = 0.01. But the resistance curve of sensor with x = 0.23 shows a dip around 15 K, similar to its curie temperature T_c. With the temperature lowering than 15 K, the sensor shows similar resistance behavior as semiconductors. For x = 0.08, a broad dip could be observed in R/R_{30K} [inset Figure 6.3(d)] at about 10 K. Below 10 K, the Hall resistance [Figure 6.3(b)] starts to show a nonlinear behavior. However, there is no ferromagnetic phase transition since no hysteresis behavior is observed. This indicates that Mn concentration is not sufficient to induce the long-range-ordered ferromagnetic transition.

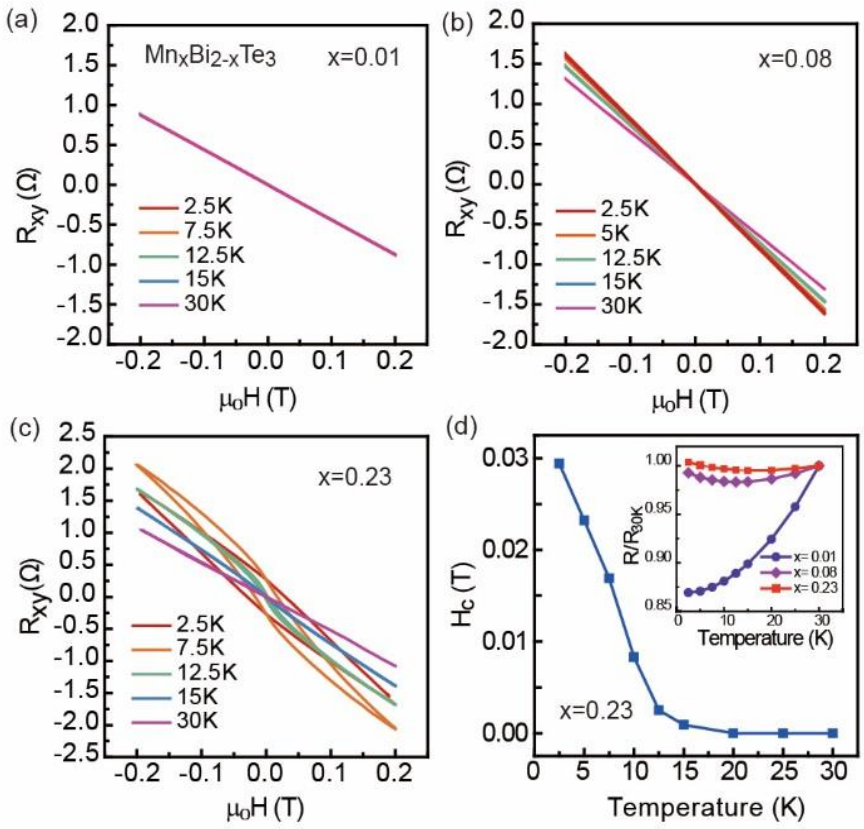

Figure 6.3 Temperature dependence of Hall resistance curves under low magnetic field for $Mn_xBi_{2-x}Te_3$ HE sensor with (a) x=0.01, (b) x = 0.08, and (c) x=0.23. (d) Temperature dependence of coercive field for $Mn_xBi_{2-x}Te_3$ HE sensor with x=0.23. Inset shows the temperature dependence of longitudinal resistance (R/R_{30K}) of sensors at various Mn concentrations.

6.3.4 The effect of temperature and Mn concentration on sensitivity of $Mn_xBi_{2-x}Te_3$ Hall effect sensors

Sensitivity is the most important figure of merit for Hall sensor. For the linear behavior of ordinary HE, Hall resistivity of sensors is expressed as $\rho_{xy} = R_H H$. For AHE, Hall resistance is described as $\rho_{xy} = R_H H + R_{AH}(M)$, which is composed of both ordinary Hall resistivity $R_H H$ and anomalous Hall resistivity $R_{AH}(M)$. The sensitivity of HE sensors can be defined as $S = d\rho_{xy}/dH$. Based on the magneto-transport properties shown in Figure 6.3,

sensitivity of sensors close to 0 T is calculated using the above equation for $Mn_xBi_{2-x}Te_3$ sensors.

Figure 6.4 shows sensitivity of sensors near zero magnetic field as a function of temperature and Mn concentration. Sensitivity of sensors with Mn concentration x = 0.01 and 0.08 is about 5 Ω/T, being a nearly flat line at various temperatures. For sensors with Mn concentration x = 0.23, sensitivity increases to 43 Ω/T when the temperature is lower than T_c. And this sensitivity is higher than most ultrathin metals such as Ni and Co [104]. Moreover, Figure 6.3 and Figure 6.4 show that the increase in sensitivity of sensors is due to AHE caused by the occurrence of ferromagnetic phase transition in strongly Mn doped sensors. Figure 6.4 further shows that highest sensitivity can be obtained around 7.5K. The relative low sensitivity together with high carrier density in these sensors implies that the bulk carriers in TI significantly contribute to Hall resistance [18]. The error due to the hysteresis loop of Hall resistance reduces the resolution of sensors. For sensors with x = 0.23, the error of the Hall sensor, i.e. $2H_c$, ranges from 28 mT to 0.15 mT, which is comparable to that of commercial product.

Although the hysteretic behaviors associated with AHE in the sensors is often undesirable for applications, it is possible to further increase the sensitivity and reduce the hysteresis by adjusting the concentration of Mn [12]. Though the sensors show improved sensitivity at lower temperatures, it is desirable to have further improvements for higher temperature applications. Nevertheless, this low temperature Hall effect sensor can be used as cryogenic magnetic field measurements, research of superconducting materials and low temperature magnetometry measurements. The possible room temperature application could be facilitated by applying the high frequency excitations to the sensors [20].

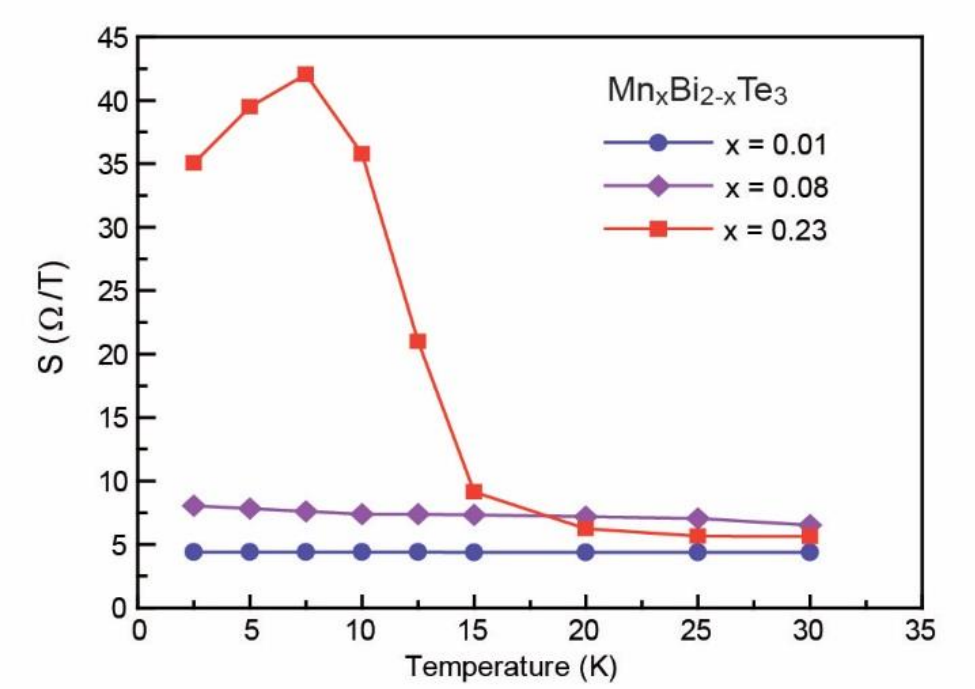

Figure 6.4 The effect of temperature and Mn concentration on Hall sensitivity of $Mn_xBi_{2-x}Te_3$ HE sensor with x = 0.01, 0.08, and 0.23.

6.4 Conclusion

In summary, a detailed study on the influence of Mn concentration on transport response and sensitivity of $Mn_xBi_{2-x}Te_3$ HE sensors are presented. Surface and crystal characterizations show that the sensors are fabricated with high quality $Mn_xBi_{2-x}Te_3$ thin films. For heavily Mn doped sensors with x = 0.23, AHE is observed when cooling to 12.5 K. As a result, an improvement on Hall sensitivity is found. The Hall sensitivity of sensors with $Mn_xBi_{2-x}Te_3$ x = 0.23 is 43 Ω/T, about 8 times higher than that of sensors with x = 0.08 and 0.01. Our work will be helpful to design TI based low temperature Hall sensors.

CHAPTER 7. ANOMALOUS HALL EFFECT SENSOR BASED ON TOPOLOGICAL INSULATOR

In the previous chapter, Mn doped TI thin film has been proved to be a promising candidate for Hall effect sensor. However, the sensitivity remains lower than the commercial ones. Nevertheless, it provides an important clue that the induced ferromagnetic TI by doping Mn in Bi_2Te_3 can increasing the Hall sensitivity due to anomalous Hall effect (AHE). This discovery broadens the family of Hall sensors. In this chapter, AHE sensors based on Cr doped Bi_2Te_3 thin films are studied with two thicknesses (15 nm and 65 nm) because their more stable ferromagnetic property. It is found in both cases that ultrahigh Hall sensitivity can be obtained in Cr doped Bi_2Te_3. Hall sensitivity reaches 1666 Ω/T in sensor with 15nm TI thin film which is higher than that of the conventional semiconductor Hall effect sensor. The anomalous Hall effect of 65 nm sensors is even stronger, which causes the sensitivity increasing to 2620 Ω/T. Moreover, after comparing Cr doped Bi_2Te_3 with previously studied Mn doped Bi_2Te_3 TI Hall sensor, the sensitivity of present AHE sensor shows about 60 times higher in 65 nm sensors. The implementation of AHE sensors based on magnetic doped TI thin film indicates that the TIs are good candidates for ultra-sensitive AHE sensors.

7.1 Introduction

Since the discovery of the Hall effect (HE), its scientific meaning as well as practical application has always been an interesting topic to researchers. Most commercial used Hall sensor nowadays are semiconductor material based on it low carrier density and high carrier mobility such as GaAs [93]. However, the high resistance and low response frequency of semiconductor limit its application in industry [92]. Besides using Lorenz force causing charge accumulation to achieve Hall in semiconductor, there is a emergent developing field known as

spin-dependent HE including quantum Hall effect (QHE), anomalous Hall effect (AHE) and spin Hall effect (SHE) [3]. Ultrahigh AHE sensitivity has been reported in different metallic heterostructure and metal-oxide interfaces [105-107]. Already achieved sensitivity of the AHE-based devices exceeds 1000 Ω/T, which surpasses the sensitivity of semiconducting Hall sensors [105]. It is believed that the AHE is an alternative approach to largely increase the Hall sensitivity and response frequency while keeping the low power consumption.

Recently, quantum AHE has been experiment observed in Topological insulator which broadens the horizon of the AHE sensor. TI is a kind of quantum material which possesses an ultra-high carrier mobility at surface while insulating in the bulk because of spin-polarized massless Dirac surface state [95]. Moreover, after introducing magnetic element into TI, quantum anomalous Hall effect (QAHE) appears in ferromagnetic TI system because the suppression of one spin channel [24, 108, 109]. The discovery of TIs broadens spin-dependent electronics and devices[110, 111]. Bi_2Te_3, Bi_2Se_3, Sb_2Te_3 were reported as 3D TI which confirmed by ARPES and magneto-transport measurements [67, 102]. It has been reported that in Mn doped TI, the Hall sensitivity increase 8 times caused by QAHE [62]. However, the sensitivity of Mn doped TI AHE sensor is much lower than other AHE sensor reported. Previously work on Cr doped Bi_2Te_3 shows that Cr introduces much stronger magnetization in the system than Mn indicating that the sensitivity of AHE sensor based on it will be very high. In order to seek a much higher sensitivity AHE senor based on TI, in this work, we fabricate Hall effect sensors based on Cr-doped Bi_2Te_3 TI thin films. The sensitivity, Hall resistivity, coercivity, electrical property, and temperature dependence of sensors will be studied.

7.2 Experiment

$Cr_xBi_{2-x}Te_3$ thin films were deposited on preheated mica substrate by Perkin-Elmer 430 molecular beam epitaxy. Mica substrate was heated to 235^oC and wait until stable. Two sets of samples with the same atom fraction (x) of 0.14 have been grown with 30min and 2hour growth time. High purity source materials (Cr, Bi and Te) was placed in the effusion Cells and heated during the growth. The flux ratio of Te per Bi was set to approximately 10 in the growth chamber to maintained Te-rich environment in order to reduce the Te vacancies. Cr concentration was controlled by adjusting the cell temperature. Crystalline structure of the as-grow thin films were characterized by X-ray Diffractometer (Siemens D500 XRD) at room temperature. Atomic force microscopy (AFM) was used to demonstrate the surface morphology and roughness of sensors. The concentration of Cr concentration was determined by FEI Quanta FE-EDX. Hall bar geometry was defined by reactive-ion etching (RIE) method with Ar gas and measured by a Quantum Design Physical Property Measurement System (PPMS).

7.3 Results and Discussion

7.3.1 Surface morphology and crystal structure of $Cr_{0.14}Bi_{1.86}Te_3$ Hall effect sensors

Figure 7.1(a) and (b) shows the surface morphology of $Cr_xBi_{2-x}Te_3$ topological insulator thin film for the sensor with different growth duration. The AFM image shows triangle terrace-like surface for both samples indicating a layer-by-layer epitaxy mechanism. However, different terrace width can be detected between two samples. The terrace width of sensor with 2hour growth time is about 300nm which is about 10 times larger than 30min growth time. The thickness of the two samples can also be obtained by scratching the surface

and scanning by AFM. The results are shown in Figure 7.1(c) and (d). The dark regions indicate the film been removed and the step in the curve shows the thickness is approximate 15 nm and 65 nm for a 30min and 2 hour sample respectively. The growth rate then can be calculated to be 0.52nm/min. The RMS roughness for both samples is under 1nm indicating the good quality of sample for device applications.

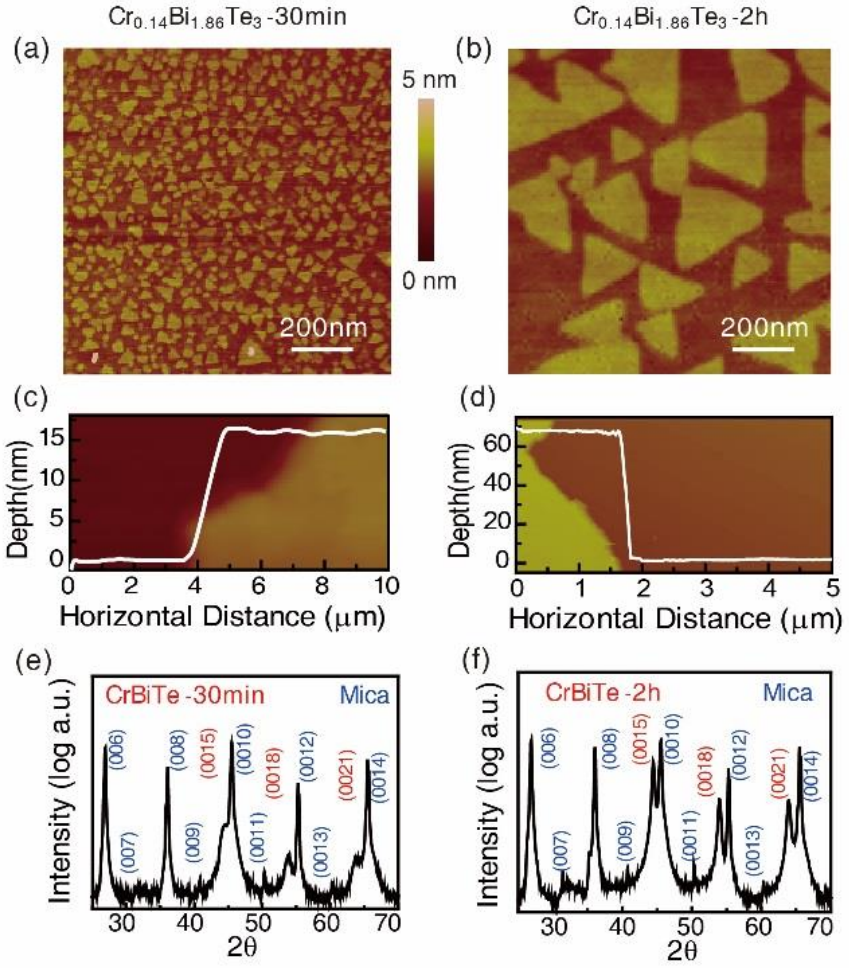

Figure 7.1 Characterization of $Cr_{0.14}Bi_{1.86}Te_3$ based sensors with different deposition duration. (a) and (b) surface morphology; (c) and (d) thickness; (e) and (f) X-ray diffraction patterns of sensors with 30min and 2hour growth, respectively.

The crystal structure analysis was shown in Figure 7.1(e) and (f). Two sets of diffraction peaks are observed for both samples. One set of these diffraction peaks can be

indexed as mica substrate; while (0015), (0018) and (0021) diffraction peaks are obtained from $Cr_{0.14}Bi_{1.86}Te_3$ thin films with rhombohedral structure. Since the low thickness of thin films, the X-ray penetrates the thin film and detected both mica substrate and sample. It is noticed that the intensity of thicker sample is higher than that of the thinner sample. No extra peak is observed in both samples indicating the thin film is highly orientated. To summary, all the characterization results demonstrate that the $Cr_{0.14}Bi_{1.86}Te_3$ thin film with thickness of 15nm and 65nm are in high quality and suitable candidate for HE sensors.

7.3.2 Magneto-transport properties of $Cr_{0.14}Bi_{1.86}Te_3$ Hall effect sensors

After characterizing thin films, HE sensors are fabricated and magneto-transport measurements are carried out. Figure 7.2 shows Hall resistivity results at different temperatures from 20K to 2.5K. At 20K, the Hall resistivity (ρ_{xy}) varies between sensors with different thicknesses. The 15nm thin film sensor shows linear behavior of ρ_{xy} and almost temperature independence. Whereas the 65nm thin film sensor shows nonlinear behavior in ρ_{xy} and a positive slope of ρ_{xy} regarding to temperature, indicating the sample has similar HE as a p-type semiconductor and it is difficult to observe QAHE in present samples. The appearance of nonlinearity in ρ_{xy} at large magnetic field indicates Cr appears to substitute in Bi site and a net magnetization is generated in the thick sample at this temperature.

With decreasing the testing temperature to 10K [Figure 7.2(b)], both 15nm and 65nm sample show hysteresis behavior with small coercivity which indicates that AHE happens at this temperature due to a paramagnetic to ferromagnetic phase transition [77]. As can be observed that ρ_{xy} saturated at a certain magnetic field. The saturation Hall resistivity (ρ_{xy}^{s}) of

65nm sample is much larger than that of 15nm sample. The Hall resistivity shows more obvious hysteresis behavior when temperature drops further down to 7.5K and 2.5K.

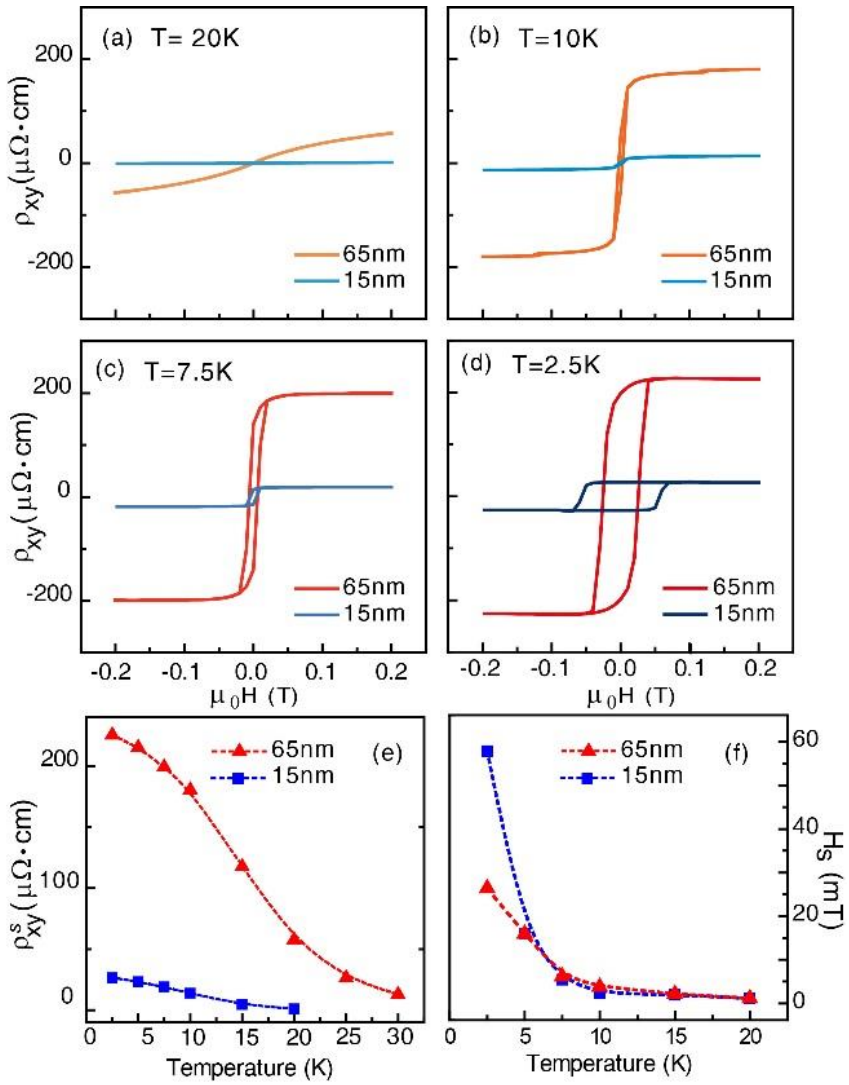

Figure 7.2 Temperature dependence of Hall resistance curves for $Cr_xBi_{2-x}Te_3$ HE sensor with different thickness. (a) T = 20K, (b) T = 10K, (c) T = 7.5K, and (d) T= 2.5K. (e) temperature dependence of saturation field for $Cr_xBi_{2-x}Te_3$ HE sensor and (f) saturation Hall resistivity at zero magnetic field. The dashed lines in (e) and (f) are guides to the eye.

At lowest testing temperature in present work (T = 2.5K), the hysteresis behavior with relative large coecivity can be observed both in thick and thin sensors[Figure 7.2 (d)]. For AHE, Hall resistance is described as $\rho_{xy} = R_H H + R_{AH}(M)$, which is composed of both ordinary

Hall resistivity $R_{\mathrm{H}}H$ and anomalous Hall resistivity $R_{\mathrm{AH}}(M)$. Here, $R_{\mathrm{AH}}(M)$ takes the dominant role in Hall resistivity. Since the magnetization of sensors behaves hysterically, the ρ_{xy} also shows the hysteresis behavior. Obviously, in all testing temperature range in this work, the saturation Hall resistivity (ρ_{xy}^{S}) of 65nm sensor is much larger than that of the 15nm sample. This may result from the magnetic anisotropy of the thin sample is different from that of the thick samples [107].This different can be further explained by comparing ρ_{xy}^{S} of these two sensors at different temperature.

Figure 7.2(f) shows the temperature dependence saturation Hall resistivity (ρ_{xy}^{S}). Both sensors with thinner and thicker film show a rapid decrease when near 8K indicating the ferromagnetic phase transition happened around this temperature (Tc), which generate magnetization after the phase transition contribute to AHE effect in $Cr_{0.14}Bi_{1.86}Te_3$ sensors [77]. The highest saturation Hall resistivity in 15nm sensor is about 27 μΩ•cm at 2.5K which is larger than that of Mn doped Bi_2Te_3 AHE sensor. Moreover, the largest value reach to 225 μΩ•cm in 65nm sensor. The large difference between the 15nm sensor and 65nm sensor demonstrate that a magnetic easy axis in the plane when thickness is about 15nm whereas a perpendicular magnetic anisotropy (PMA) has been obtained when the $Cr_{0.14}Bi_{1.86}Te_3$ sensor thickness reach 65nm which is the similar to the AHE senor with CoFeB and PtFe thin film [55].

Another crucial characteristic of AHE sensor is the saturation field (H_s). Figure 7.2(e) is the summary of H_s as temperature varying from 2.5K to 30K. Both of the two samples show a decrease tendency of H_s when temperature increase which is similar to typical ferromagnetic materials [103]. An abrupt change of H_s can be observed at about 8K for both samples, consisting with the curie temperature (Tc) shown in ρ_{xy}^{S}. The lowest H_s for both thin film

sensors is below 10mT, which exhibit low switching field superiority for the device application [55]. The high saturation Hall resistivity and low saturation field imply the ultrahigh sensitivity in $Cr_xBi_{2-x}Te_3$ based sensor.

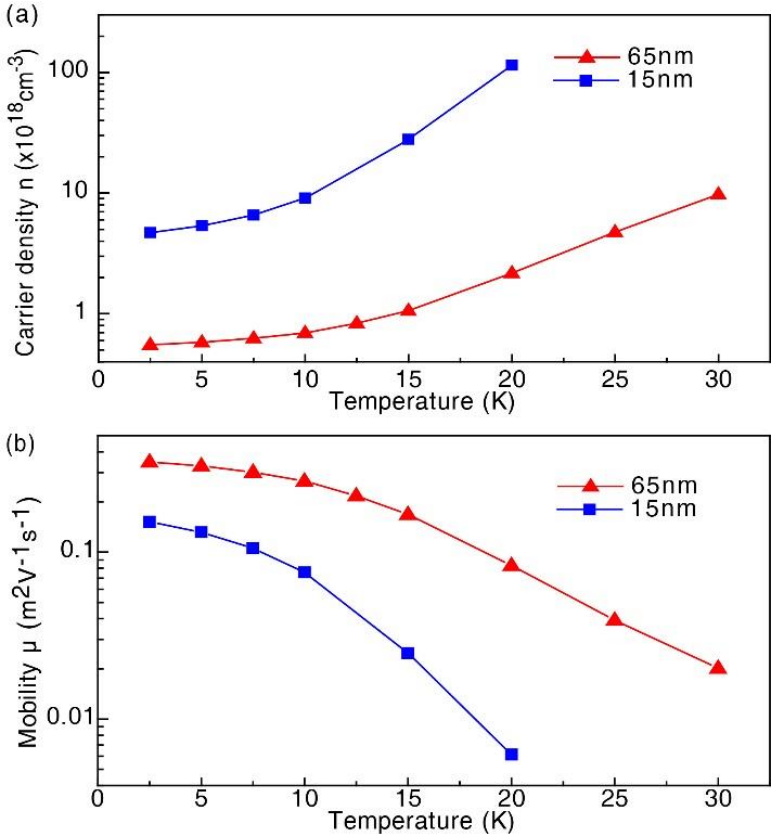

Figure 7.3 Carrier density(a) and carrier mobility(b) of TI AHE sensor with 15 nm and 65 nm thickness $Cr_xBi_{2-x}Te_3$ thin film.

The carrier density can be extracted from the Hall measurement by using: $n = (|R_H|e)^{-1}$, where R_H is the Hall coefficient and e is the electron charge. Figure 7.3 (a) shows temperature dependent carrier density. As temperature increases the carrier density also increasing. The thinner sample has higher carrier density of than the thicker sample because n is inverse proportional to ρ_{xy}. Since ρ_{xy} of thin sample is smaller than that of the thick sample, n is larger. The lowest carrier density can achieve 0.55×10^{18} cm^{-3}. The carrier mobility [Figure 7.3 (b)] of $Cr_{0.14}Bi_{1.86}Te_3$ TI sensor is calculated by using: $\mu = {}^{\sigma_{xx}}/_{ne}$, where σ_{xx} is the longitudinal

conductivity. The mobility decrease from 0.35 m^2/Vs to 0.02 m^2/Vs with temperature increase from 2.5K to 30K for 65nm sample. For the 15nm sample, similar trend can be observed with lower value of carrier mobility, ranging from 0.16 to 0.006 m^2/Vs. The highest carrier mobility are comparable to pure Bi_2Te_3 in which the effective mass of electron is almost zero[83]. The relative low carrier density and high carrier mobility are signs of high Hall sensitivity.

7.3.3 The effect of temperature on sensitivity of $Cr_xBi_{2-x}Te_3$ Hall effect sensors

The most important characteristic parameters of HE sensor is Hall sensitivity (S), which is the figure of merit for Hall sensor. The sensitivity of AHE sensors can be defined as initial Hall slope $S = d\rho_{xy}/dH$. Based on the magneto-transport properties shown in Figure 7.2, Hall sensitivity of $Cr_{0.14}Bi_{1.86}Te_3$ sensors with different thickness can be calculated. Figure 7.4 shows sensitivity of sensors within saturation field as a function of temperature and thickness. Inset of Figure 7.4 shows the schematic picture of Hall sensor under testing.

It can be observed that with temperature decreasing the sensitivity tends to increase. Below the temperature (T = 8K), sensitivity suddenly jumped to magnitude higher than that of the higher temperatures. This is because doping Cr introduces magnetization after ferromagnetic phase transition causing AHE. The thinner TI sensor (15nm) shows the highest sensitivity S = 1666 Ω/T at T = 2.5K, surpassing the highest sensitivity of semiconductor HE sensor (1000 Ω/T) [112]. At T = 2.5K, the sensitivity reached 2620 Ω/T in 65nm sensor which is twice higher than 15nm sample. Moreover, Fig. 7.4 also compares the sensitivity between Cr doped Bi_2Te_3 and Mn doped Bi_2Te_3, of which the sensitivity is in the range 5 Ω/T - 43 Ω/T [62]. The sensitivity of 65nm $Cr_{0.14}Bi_{1.86}Te_3$ AHE sensor is about 60 times higher than that of Mn doped Bi_2Te_3 AHE sensor, which may due to the more stable ferromagnetism and insulation of $Cr_{0.14}Bi_{1.86}Te_3$. It should be mentioned that in the temperature range from 2.5K to

10K, sensitivity keep higher than 2000 Ω/T. This low temperature AHE sensor can be used as cryogenic magnetic field measurements, research of superconducting materials and low temperature magnetometry measurements.

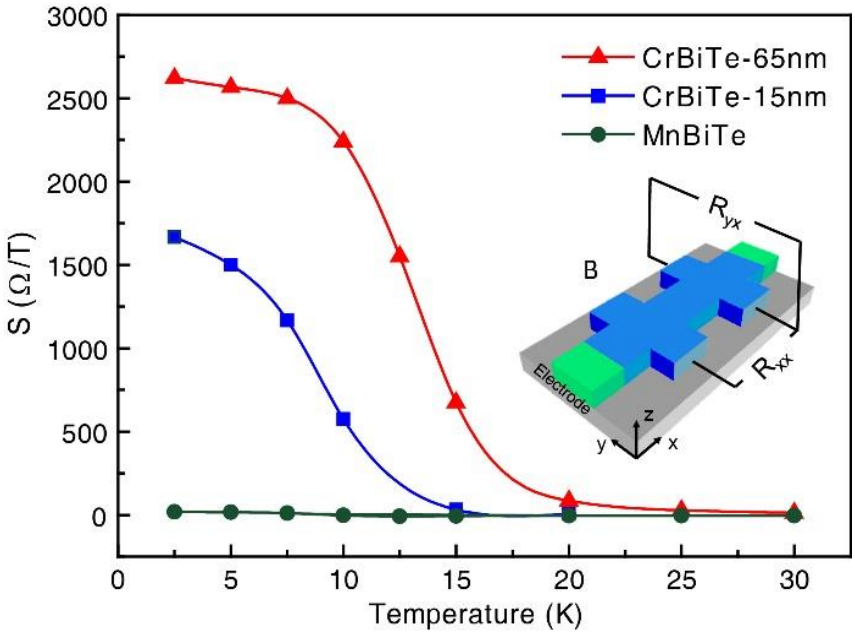

Figure 7.4 Temperature dependence of sensitivity for $Cr_xBi_{2-x}Te_3$ AHE sensor with different thickness. Inset shows the schematic picture of HE sensor under testing. The green curve shows the topological insulator thin film Mn doped Bi_2Te_3 with similar testing condition.

7.4 Conclusion

To summarize, we studied AHE sensor based on $Cr_xBi_{2-x}Te_3$ topological insulator with thickness of 15 nm and 65 nm. It is found that the sensor remains high sensitivity in both thicknesses. The giant sensitivity is found S=2620 Ω/T at 2.5K in $Cr_xBi_{2-x}Te_3$ sensor with thickness of 65 nm which is more than twice the sensitivity of semiconductor HE sensor. The high sensitivity results from Cr induced AHE in TI thin films. The $Cr_xBi_{2-x}Te_3$ sensors show high carrier mobility, which enables the application of low power consumption magnetic

sensors. Moreover, both saturation Hall resistivity and sensitivity show dependence on thickness, which indicates the variation of magnetic anisotropy with changing thickness in sensors. Our work therefore enlightens the design of low-energy consumption and high sensitivity Hall devices such as magnetic sensor and memory devices.

CHAPTER 8. MAGNETIC SENSOR BASED ON MAGNETOELECTRIC EFFECT IN COBALT FERRITE AND BARIUM TITANATE COMPOSITE

Multiferroic materials exhibit magnetoelectric coupling and promise new device applications including magnetic sensors, generators, and filters. An effective method for developing magnetoelectric (ME) materials with enhanced ME effect is achieved by the coupling through the interfacial strain between piezoelectric and magnetostrictive materials. In this study, the electrical and magnetic properties of Ga doped magnetoelectric $CoGa_xFe_{2-x}O_4/BaTiO_3$ composite are studied systematically. It is found that Ga doping improves the sensitivity of magnetoelastic response and stabilizes the magnetic phase of the composites. More importantly, Ga doping reduces the electrical conductivity of composite, as well as the dielectric loss. An enhancement of the electrostrain with doping Ga is also observed. Quantitative estimation indicates that magnetoelectric coupling is enhanced for Ga-doped $CoGaxFe_{2-x}O_4/BaTiO_3$ composites compared to a previous work with Ga-doping. Thus, the present is beneficial to the practical application of composite $CoFe_2O_4/BaTiO_3$-based multiferroic materials.

8.1 Introduction

Multifunctional devices based on magnetoelectric phenomenon require the coexistence of ferroelectricity and ferromagnetism, in addition to a strong coupling between the two ferroic orders [38]. The ferroelectric/ferromagnetic composites enable the development of magnetoelectric (ME) materials with enhanced ME effect. This can be achieved by indirect coupling through the interfacial strain between the ferroelectric and ferromagnetic materials [49-51]. Such strain mediated ME effect can be used to generate electric polarization in the ferroelectric component of the composite due to applied magnetic field in the ferromagnetic

component or magnetization in the ferromagnetic component due to applied electric field in the ferromagnetic component. The property tensor dE/dH can be given by the product of the proportionality tensor of the phases [113]:

$$\alpha_{ij} = \frac{d\lambda_{ij}}{dH_j} * \frac{dE_i}{d\lambda_{ij}}$$

where α_{ij} is defined as linear magnetoelectric coefficient, dλ/dH is the magnetostriction derivative and dE/dλ is the change in the electric field with strain. Because the ME effect in composites is extrinsic, it depends on the microstructure of the composite and the strain mediated coupling across the interface of the ferromagnetic-ferroelectric components. Studies have been done involving combinations of different magnetostrictive and piezoelectric materials such as variety of ferrites and titanites [48, 114-119]. The inevitable drawback in this application is the leakage current due to the low resistivity of the ferromagnetic phase [115]. There is therefore need to develop alternative magnetoelectric materials with low leakage current. In this study, the results of an investigation on composites of Ga-substituted cobalt ferrite ($CoGa_xFe_{2-x}O_4$) and $BaTiO_3$ are presented which also shows potentials for lower leakage current.

8.2 Experiment

$CoGa_xFe_{2-x}O_4$ (x = 0 - 0.3) was prepared by the conventional two-phase solid-state reaction using the constituent oxide powders. 50 wt.% of $CoGa_xFe_{2-x}O_4$ was mixed with 50 wt.% of an analytical reagent grade $BaTiO_3$ powder. To ensure homogenous mixture, the chemicals were milled for 6 h, calcined twice in the air at 1273 K for 4 hrs and sintered at 1473 K for 6 hrs. The sintered pellets were of 15 mm diameter.

To study the crystal structure and purity of the composite samples, room temperature X-ray diffraction (XRD) was performed using Cu K_α radiation. The microstructure and composition of the samples were studied by scanning electron microscopy (SEM) and energy dispersive X-ray spectroscopy (EDS), respectively. Fractured sample surfaces were used for the SEM analysis. Magnetic properties were studied in a vibrating sample magnetometer (VSM) with maximum applied magnetic field of 4 kOe. Magnetostriction was measured, in an electromagnet, with magnetic field applied in the direction of strain measurement using strain gauges attached to the samples. Ferroelectric workstation was used to measure the polarization as a function of the electric field and electric field induced strain.

8.3 Results and Discussion

The microstructure and crystal structures are similar in $CoGa_xFe_{2-x}O_4/BaTiO_3$ (x = 0 - 0.3). The electron images and XRD patterns in Figure 8.1 are for the composition at x = 0.3. The backscattered electron micrographs [Figure 8.1(a)] indicate that the samples have high density. The light and dark contrasts represent the $BaTiO_3$ (BT) and $CoGa_xFe_{2-x}O_4$ (Ga0.3CFO) phases, respectively. The secondary electron modal micrograph of the sample [Figure 8.1(b)] shows that the BT and Ga0.3CFO phases are distributed evenly with the Ga0.3CFO forming some angular morphology clusters. BT appear as smaller particles with irregular shapes.

The corresponding EDS elemental maps are shown in Figure 8.1(c) and (d). The light area in Figure 8.1(c) and the dark area in Figure 8.1(d) represent Ba and Ga respectively. These maps indicate Ga is doped into the CFO phases rather than BT phase in the composite. The XRD pattern in Figure 8.1(e) indexed with $BaTiO_3$ and $CoGa_xFe_{2-x}O_4$ using PDF cards shows that the composite consists of tetragonal $BaTiO_3$ phase (indexed in red fonts) and spinel $CoGa_xFe_{2-x}O_4$ phase (indexed in blue fonts). And, no secondary phases are form.

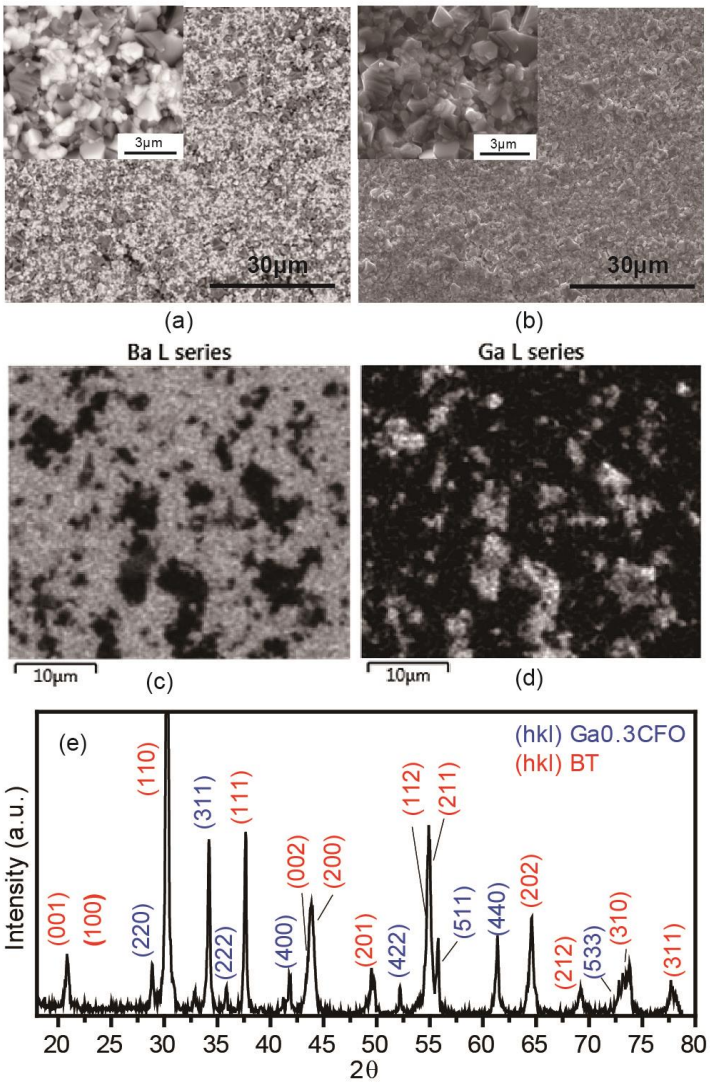

Figure 8.1 Characterization of samples used for ME sensor. (a), (b), (c), and (d) SEM image and (e) XRD pattern of $CoGa_xFe_{2-x}O_4/BaTiO_3$ (x = 0.3) and EDS images.

The magnetic hysteresis loops of the $CoGa_xFe_{2-x}O_4/BaTiO_3$ composite (x = 0, 0.1, 0.2, 0.3), showing shapes typical of soft magnetic material are presented in Figure 8.2(a).

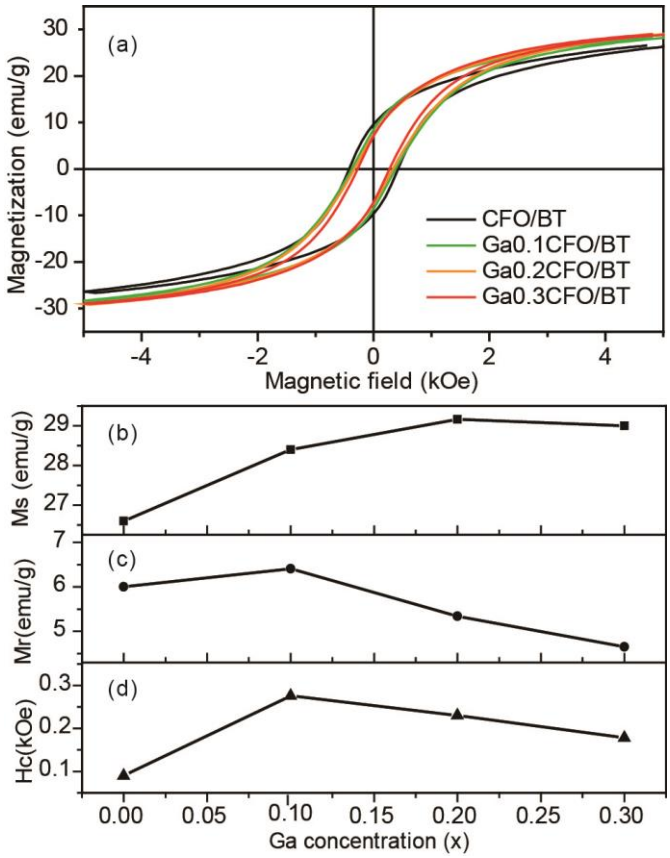

Figure 8.2 Magnetic properties of $CoGa_xFe_{2-x}O_4/BaTiO_3$ (x = 0, 0.1, 0.2 ,0.3) at room temperature: (a) magnetization curve, (b) saturation magnetization (Ms), (c) remnant magnetization (Mr), and (d) magnetic coercive field.

The saturation magnetization, remanence and coercivity are shown in Figure 8.2(b), 2(c), and 2(d) respectively. Magnetization at maximum applied field of 4 kOe increases with Ga concentration in $CoGa_xFe_{2-x}O_4$ up to x = 0.2 and decreases slightly at x = 0.3. Similar observation was previously reported in which it was stated that Ga^{3+} has A-site preference [120, 121]. Such may also results in cobalt ions being displaced into the B-sites. Since the net magnetic moment in spinel ferrites is obtained by $m = \sum m_{B-sites} - \sum m_{A-sites}$, substituting for Fe^{3+} on the A-sites and displacing more Co^{2+} into the B-sites would increase magnetic moment. $\sum m_{B-sites}$ and $\sum m_{A-sites}$ represent the net magnetic moment of the B-sites and A-

sites cations, respectively. The slight decrease at x = 0.3 may indicate the onset of some Ga ions being substituted into the B-sites as its concentration increases.

The remnant magnetization, M_r [Figure 8.2(c)] and coercive field (Hc) in Figure 8.2(d) initially increase from x = 0 to x = 0.1 but afterwards decreases. This may be a consequence of changes in magnetocrystalline anisotropy due to Ga^{3+} in the spinel phase and grain size [122, 123]. It is known that the magnetization process includes both domain wall motion and domain rotation. The small grains tend to result in low density of domain walls. Therefore, the domain rotation becomes dominant factor during magnetization rather than the domain wall motion. Since the domain rotation consumes more energy than the domain wall motion, the coercive field (Hc) increases. The trend observed here has been reported for both coercive field and magnetocrystalline anisotropy in Zn-substituted $CoFe_2O_4$ [124].

In Figure 8.3(a), similar trend in magnetostriction as a function of applied magnetic field is obtained for all composites. Generally, magnetostriction decreases in the Ga-containing composites, indicating the effect of Ga-substitution on the magnetostrictive properties of spinel cobalt ferrite phase. This decrease is related to the weakening of the exchange coupling with substitution of non-magnetic Ga^{3+} which would affect magnetostriction. A similar observation was reported in magnetostrictive properties of Ga-substituted cobalt ferrite at 300 K [120]. The observation that the magnetostriction plots do not saturate as would be obtained in only $CoGa_xFe_{2-x}O_4$ phase indicates the coupling of the strains on the BT and $CoGa_xFe_{2-x}O_4$ phases.

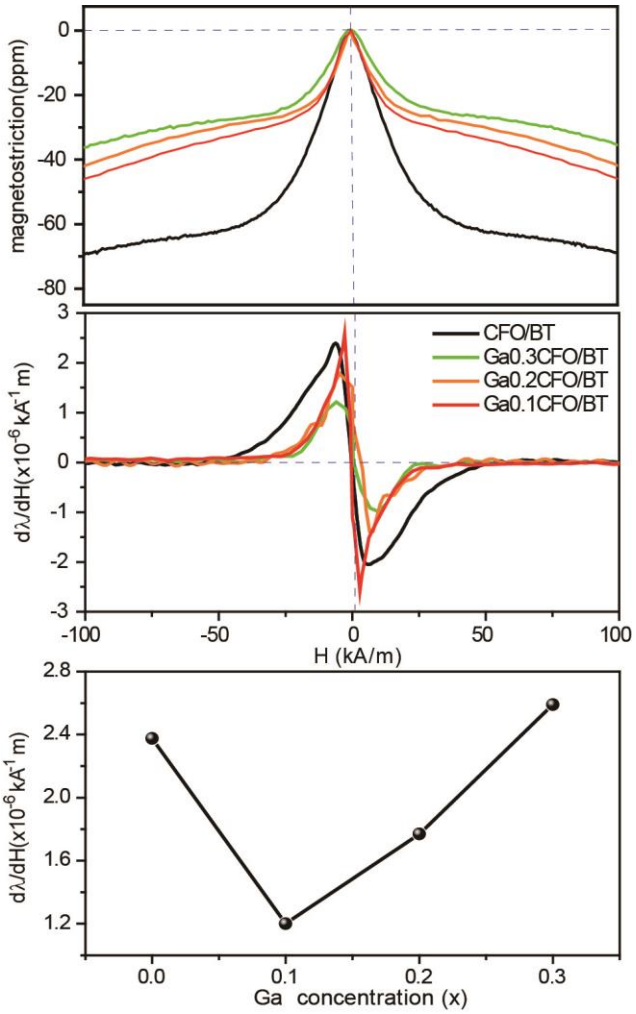

Figure 8.3 Magnetostriction (λ) vs. magnetic field (H) curves for $CoGa_xFe_{2-x}O_4/BaTiO_3$ (x = 0, 0.1, 0.2, 0.3). (b) dλ/dH as a function of magnetic field (H). (c) The maximum sensitivity of magnetostriction with respect to different Ga concentrations.

The strain derivative (dλ/dH), in Figure 8.3(b) is an important parameter which demonstrates the sensitivity of magnetoelastic response to an external field. The maximum strain derivative $(d\lambda/dH)_{max}$ in Figure 8.3(c) shows an increase with Ga concentration in $CoGa_xFe_{2-x}O_4/BaTiO_3$ composite. The highest $(d\lambda/dH)_{max}$ value is found at x = 0.3 in this study which is higher than the previous reported pure $CoFe_2O_4$ [121] as well as some other

ME composites [125]. This high strain derivative indicates possible improvement of the ME effect in CFO/BT composite.

The ferroelectric properties of the composites are shown in Figure 8.4. The polarization vs. electric field (P-E) loops obtained at room temperature, are shown in Figure 8.4(a). It can be seen that there is no saturation polarization as typically seen in P-E loops of pure $BaTiO_3$. This indicates that electrical conductivity increase with increasing the electric field, i.e the existence of leakage current. However, the electric hysteresis loops become slanted and less coercive with increasing Ga concentration in the composites, suggesting the decrease of leakage current with Ga doping. Both the remnant polarization (P_r) and coercive field (E_c) get smaller as Ga concentration increases in the $(CoGa_xFe_{2-x}O_4)/BaTiO_3$ composite, as show in Figure 8.4(b). This indicates a deviation from a typical ferroelectric behavior of BT to one in which it is coupled to the CFO phase. This deviation in the long range order behavior of electric dipoles is due to the ferrite particles with a spinel structure being incorporated into $BaTiO_3$ perovskite structure.

The improvement of the leakage current could also be observed from the plot of the loss tangent (tan δ) as a function of temperature shown in Figure 8.4(c). The loss tangent of the composites was measured at 10 kHz. It can be seen that the tan δ value is lower in Ga0.3CFO/BT than CFO/BT at all temperatures and is about one-half less at 160℃. It is likely that the increase Ga concentration in the composites reduces defects such as oxygen vacancies in the $BaTiO_3$ ferroelectric phase, which is responsible for the decrease in electrical conductivity as Ga content increases. The unipolar electric-field-induced strain S(E) curves of the composite are shown in Figure 8.4(d). It can be found that the electrostrain of $(CoGa_xFe_{2-x}O_4)/BaTiO_3$ with x = 0.3 is higher than that of x = 0.2. Moreover, the normalized strain d_{33}^*

can be calculated from the S(E) curve by S_{max}/E_{max} ratio in the unipolar strain curve. The biggest d_{33}^{*} is about 514 pm V^{-1} in present study when x = 0.3. As a result, the electrostrain of the composites also improves with Ga doping.

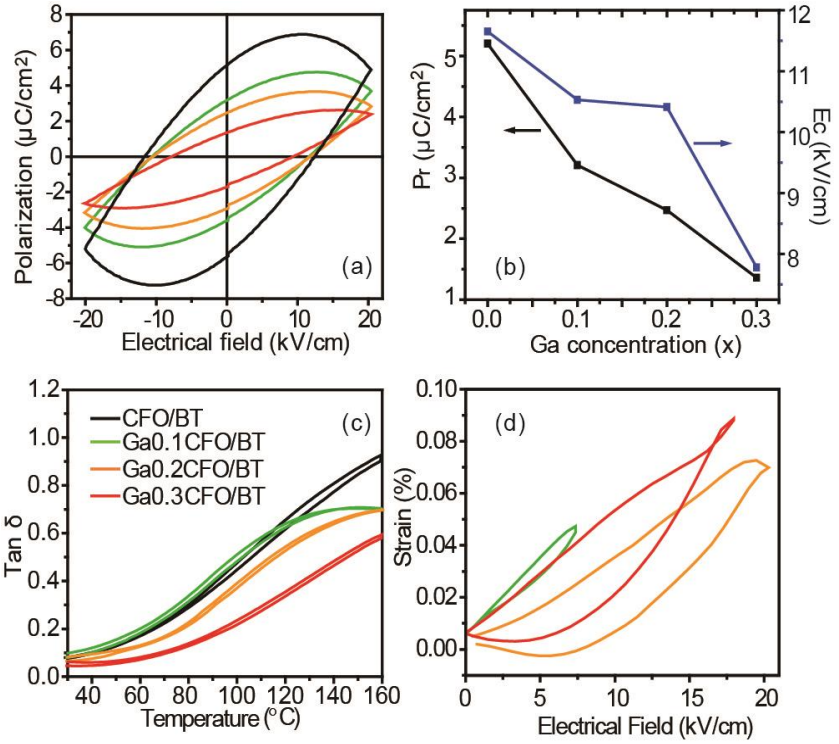

Figure 8.4 (a) Ferroelectric properties of $CoGa_xFe_{2-x}O_4/BaTiO_3$ composites (x = 0, 0.1, 0.2, 0.3). (b) Remnant polarization and electric coercive field with different Ga concentration in the ferromagnetic phase. (c) Loss tangent as a function of temperature at 10 kHz frequency. (d) The unipolar electric-field-induced strain S(E) curves.

Considering the product of the proportionality tensor of the phases described in introduction, Van den Boomgaard established a model which can be used to estimate the ME voltage coefficient, assuming comparable Young's moduli for both $CoFe_2O_4$ and $BaTiO_3$. The dielectric constant of $BaTiO_3$ is much larger than $CoFe_2O_4$ [85].

The ME voltage coefficient of the composite given by this model is $(dE/dH)_{comp} = m_v(d\lambda/dH)_{CFO} * (1 - m_v)(dE/d\lambda)_{BT}$. We used the sample with x = 0.3 (Ga0.3CFO-BT),

in which we had the maximum optimization, to estimate the coefficient. From the magnetostrictive derivative (Fig 8.3) and electrical electric field-induced strain curve (Fig. 8.4), we can get $(d\lambda/dH)_{Ga0.3CFO} = 2.6 \times 10^{-9} m/A$ and $(dE/d\lambda)_{BT} = 1.95\, V/pm$. Using 0.5 volume fraction of BT and considering the uniform distribution of the phases as previously shown in the microstructure presented in Fig 8.1, we can obtain the ME voltage coefficient of $\alpha = 1.26$ (m/A)(V/m), which is larger than previous reported for CFO/BT $\alpha = 1.19$ (m/A)(V/m) [113]. Therefore, this work demonstrates that by doping Ga in $(CoGa_xFe_{2-x}O_4)/BaTiO_3$, both magnetostriction sensitivity and electrostrain increases, indicating enhanced magnetoelectric performance for practical applications.

8.4. Conclusion

In this work, systematically studies on the ferroelectric and ferromagnetic properties of $(CoGa_xFe_{2-x}O_4)/BaTiO_3$ (x = 0.1, 0.2, 0.3) magnetoelectric bulk composites are presented. The results indicate a coupling effect of the ferroelectric and ferromagnetic phases. Although the magnetostriction decreased in amplitude with Ga concentration, the maximum strain derivative increased. The maximum strain derivative is obtained for Ga0.3CFO/BT. Moreover, the magnetostriction plots show clear indication of interaction between both phases. Also, Ga-substitution into the composite both suppresses electrical conductivity and improves the normalized strain d_{33}^*. Through model estimation, the $(CoGa_{0.3}Fe_{1.7}O_4)/BaTiO_3$ composite shows larger ME voltage coefficient than CFO/BT implying magnetoelectric coupling are enhanced after doping Ga. These results offer new insight into the ability of improving the response of magnetostrictive and controlling electrical conductivity in the CFO/BT multiferroic composite.

CHAPTER 9. ULTRAFAST OBSERVATION OF DEMAGNETIZATION IN MAGNETICALLY DOPED TOPOLOGICAL INSULATORS

9.1. Introduction

Previous chapters introduced some basic studies and sensor applications of magnetically doped topological insulators, which all put TIs in static or quasi static environments. This chapter will focus on the dynamics of magnetization, demagnetization, and relaxation in magnetically doped TIs by a cutting-edge technique, ultrafast time-resolved magneto-optical Kerr effect (MOKE) spectroscopy.

Spectroscopy is an important tool for studying the light and matter interaction. Electrons in matters are excited by the external light, which triggers the transitions between different energy states in matters. Information and properties of the matter can be detected by an emission spectrum, a plot with your interest as a function of wavelength or frequency. Ultrafast time-resolved MOKE spectroscopy based on the state of art ultrafast laser source, which can provide femtosecond (10^{-15} second) pulses with a peak power up to the petawatt level (10^{15} *W*). The ultrashort and ultrahigh power laser can drive matters to an extreme non-equilibrium state instantaneously. Thus, this provides an opportunity to study dynamic process far beyond the conventional thermal-equilibrium environments.

9.2. Ultrafast Time-Resolve Magneto-Optical Kerr Spectroscopy Setup

Magneto-optical Kerr effect describes the change of light when reflected from a magnetized matter surface. In this experiment, a polarized ultrafast laser reflects from the sample and detected by the detector. A change in Kerr rotation, ellipticity, or polarized amplitude can be converted into changes in light intensity. The experiment setup is a pump-

probe spectroscopy. The basic idea of this method is using two or more optical pulses with variable time delay between them to investigate the dynamic process. In this experiment, we use the spectroscopy built in Dr.Jigang Wang's lab. The detailed setup process can be find in reference [126]. Here I briefly show the schematic picture of the setup in Figure 9.1. The laser source comes from the Ti; Sapphire regenerative amplifier (Model: SplitFire Pro, Spectro-Physics). The center wavelength of the polarized laser source is 799 nm (1.55 eV), the repetition rate is 1 kHz. Then the output laser is split into two path, pump and probe path. The pump beam is modulated to 500 Hz, 400nm circularly polarized laser, which goes through delay stage and reach a TI sample surface. The probe beam is the same p-polarized laser focus also on sample surface. The reflective beam of probe laser is collected and measured in the polarization bridge. A TI thin film sample is placed on top of a permanent magnet which field is perpendicular to TI surface. Both sample and magnet are hold in the Cryostat chamber and will cool down to Temperature ~ 4.2K.

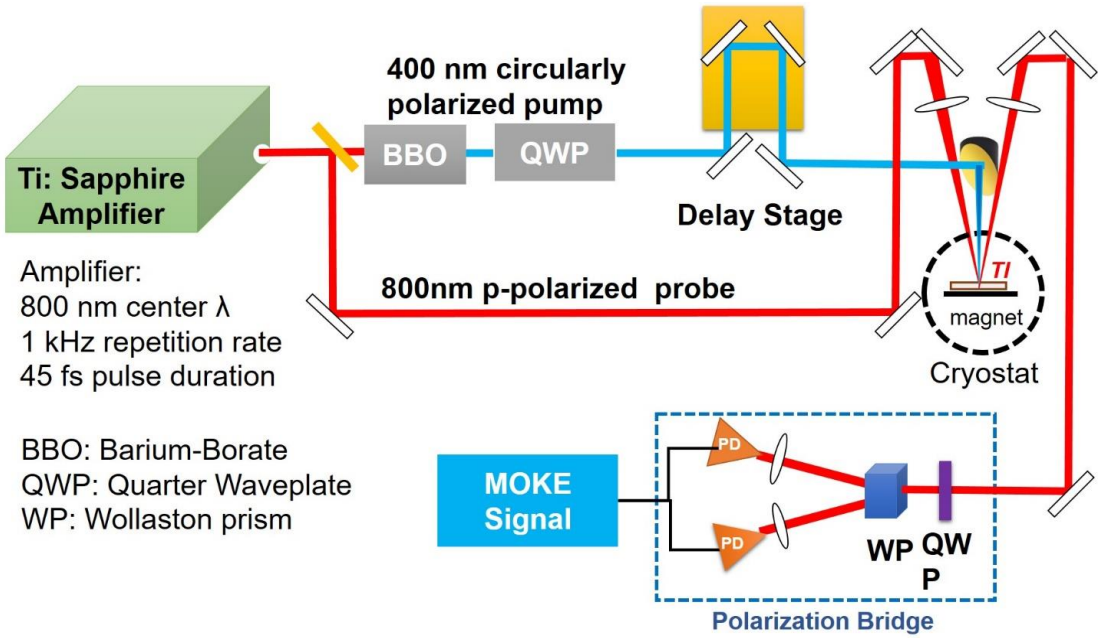

Figure 9.1 Ultrafast time-resolve magneto-optical Kerr spectroscopy setup with topological insulator samples.

9.3. Results and Discussions

The sample in the experiment is $Cr_xBi_{2-x}Te_3$, x=0.29 TI thin film. According to the previous studies, this thin film experience ferromagnetic phase transition at T_c ~30K according to magneto transport study. The magnetization saturated at $B_\perp$ ~ 0.2 T. Therefore, the magnetic field applied by the permanent magnet is $B_\perp$ ~ 0.25 T to ensure all magnetization is align along the external field.

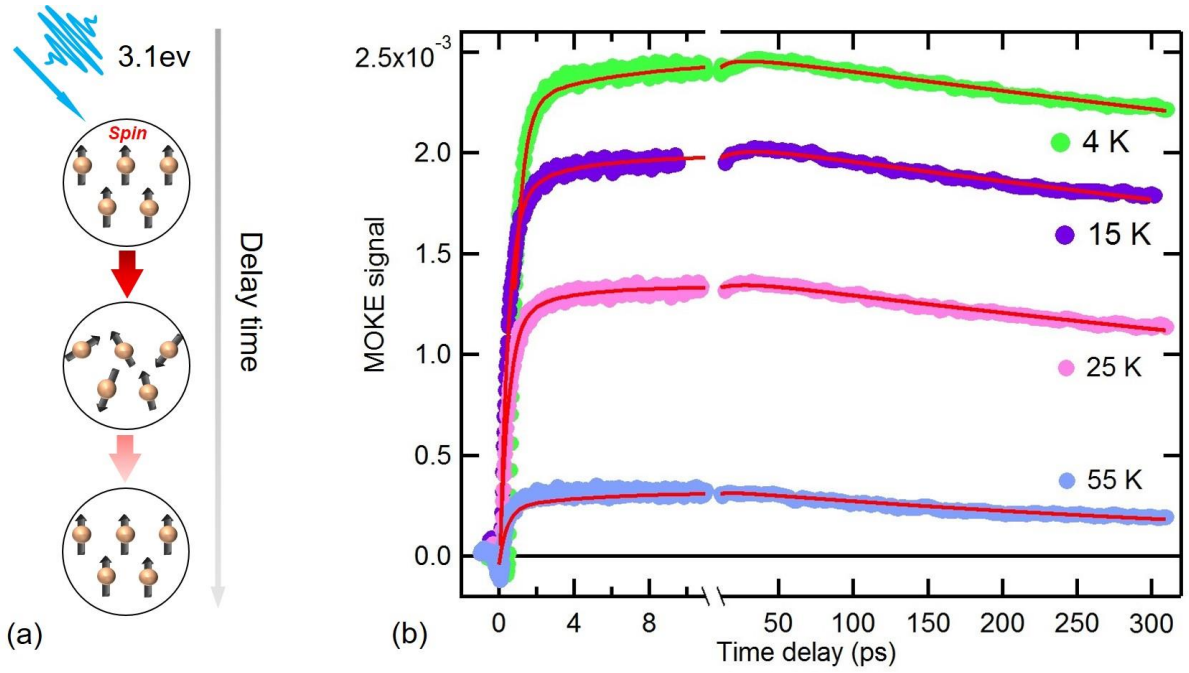

Figure 9.2 Schematic picture of pump laser interacting with magnetically doped TI thin film sample (a); Temperature dependence of the photoinduced MOKE signal first 300 ps with fitting curves in red (b).

Figure 9.2(a) shows the schematic picture of pump laser interacting with spins in Cr doped Bi_2Te_3. Before the laser pulse reaches the sample surface, because the external magnetic field, all spin is aligning in the same direction. When laser pulse reaches the surface, the photon interacting with the electrons, the electrons interaction with spins, spins begin to precession, followed by the relaxation process of the spin align to the external field. Figure 9.2(b) is the

detailed time-dependent MOKE signal change at various temperatures. There are at least two dynamics regarding to the MOKE signal: fast raising process at delay time less than 5 ps and then slow decay with long time duration. The maximum MOKE signal related to the largest demagnetization in samples. One can clearly observe that the lower the temperature, the stronger MOKE signal one can get. To further analysis this curve, we use the following equation to fit the curve:

$$F(t) = \left\{A\left[1-\left(e^{\frac{-t}{t_1}}\right)\right] + B\left[1-\left(e^{\frac{-t}{t_2}}\right)\right] + C\left[1-\left(e^{\frac{-t}{t_3}}\right)\right]\right\} e^{\frac{-t}{t_4}}$$

This model consists three exponential rising terms and a single exponential decay term, where A, B, C is the raising constants and t_1, t_2, t_3 and t_4 are the rising and decay time constants. To fit the curve with the above model, we can get the temperature dependent time constants as shown in Figure 9.3. The general tendency of four time constants is all decrease with increasing temperature. Further analysis is required to study the reason of this decreasing tendency.

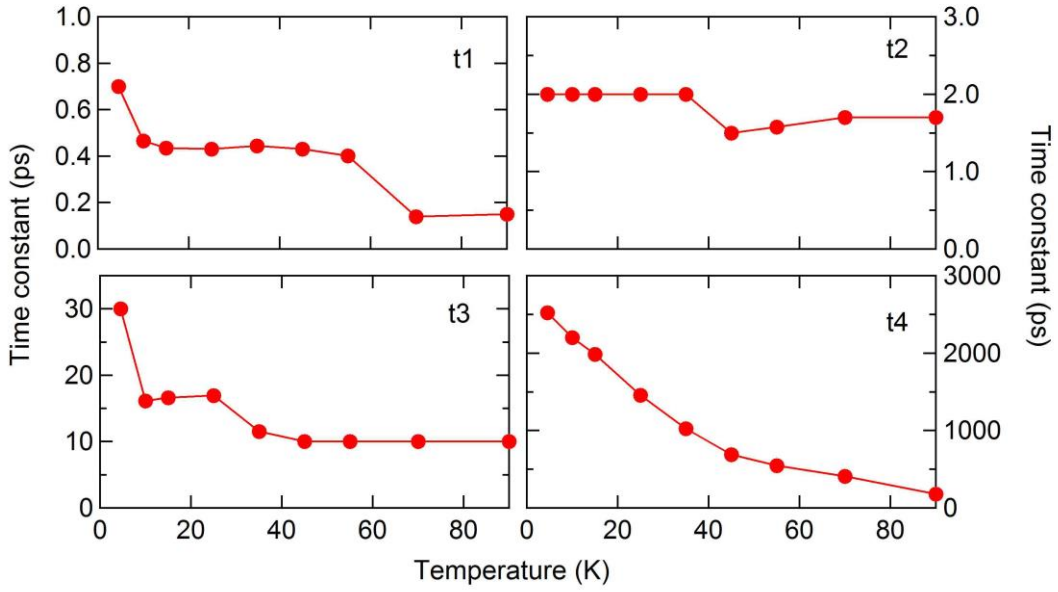

Figure 9.3 Temperature dependent rise and decay time constants.

To summarized this on-going project, temperature dependent photoinduced demagnetization and relaxation dynamics are measured. Results show demagnetization amplitude becomes larger as decreasing temperature indicating ferromagnetism sets in at lower temperature. Three demagnetization and one relaxation dynamics are observed, for which the reason needs further investigation.

CHAPTER 10. CONCLUSION

Magnetic sensors are taken up a worthy place amidst the great diversity of transducer of nonelectric domains into electronic data. Various types of magnetioresistors, Hall sensors, magnetodiodes, magnetotransducers of sophisticated design and operation have been developed. Over hundreds of papers, reviews, monographs and patents have been published on the magnetic sensor treating various aspects of the properties and operations, prototype device designs, fabrication, technology and application. However, the priority given to specific problems makes a comprehensive and balanced analysis of this field of study more difficult, especially in view of its rapid development over the past few years. The material used for magnetic sensors are also important and evolution along with the development of magnetic sensor.

The present work mainly focus on two kinds of materials, multiferroic composite and topological insulator, targeting at two magnetic sensors: magnetoelectric multiferroic sensor and Hall effect sensor.

First part of the thesis focus on magnet sensor based on a novel kind of quantum material, namely, topological insulators (TIs). These materials exist both in two dimension (2d) and three dimension (3d). They are mostly insulating in the bulk but have high carrier mobility on edge of 2d materials and surface of 3d materials. The existence of the edge states or surface states is because of the unique bulk band structure which distinguishes TIs from normal insulators. Instead of just have an energy gap which prohibit electron jumping from valence band to conduction band, the bulk band inversion of TIs creates two surface channels to link valence band and conduction band which allows electrons with different spin orientations (up or down) can transfer in these two channels in opposite directions. The bulk band inversion is

a result of a strong relativistic effect of core electron spin and its orbital momentum interaction. The two channels of electrons propagating with different directions are linearly dispersed in energy vs. momentum diagram and cross at a certain point in momentum space inducing a special point, Dirac point, where the effective mass of electrons at that state is approaching zero. Dirac cone of Surface states in TIs is very much similar to the band structure of graphene at certain points in momentum space. The electron mobility at Dirac point of TIs is as large as that of graphene, which enable them the candidates for high speed transistors. All work in present thesis focus on 3D TI systems. Compared to graphene, because of the bulk nature of 3D TIs, the problem due to the 2D nature of graphene can be neglect such how to acquire single layer and edge effect.

However, as a coin has two sides, the bulk bandgap of mostly all 3D TIs is too small to any room temperature application. What's more, most 3D TI systems, including Bi_2Se_3, Bi_2Te_3, Bi_xSb_{1-x}, Sb_2Te_3, has almost non ideal band structure which requires totally insulating in the bulk and Dirac point centered in the bulk bandgap. However, due to the naturally small band gap and defects brought into system during crystal growth, none of the existing systems fulfill all the requirements. Therefore, first part of my thesis related to TI is to grow high quality TI systems. Molecular Beam Epitaxy (MBE) method was used to grow TI thin film on different substrates. Results shows that TIs grown on mica substrate provide the lowest surface roughness, largest terrace width and lowest sheet resistance compared to those grown on Si substrates and GaAs substrates. What's more, mica is transparent and flexible substrate which enable the possible application of TI thin films on optoelectronics.

One central issue that has plagued the experimental progress with TI is the presence of bulk doping or conductance in most naturally grown crystal. Therefore, second part of TI

work is to make the ideal 3D TIs with reducing bulk conductivity. Elemental doping and composition tuning ternary compounds are used on two typical TI systems Bi_2Te_3 and Sb_2Te_3 to make $(Sb_{1-x}Bi_x)_2Te_3$ compound to tune both the Dirac cone and Fermi level into the bulk band gap. After doping Bi into Sb_2Te_3 to certain concentration, I observed a maximum in sheet resistance demonstrate presentence of Dirac point between bulk valence band and conduction band. However, the conductance and resistance measurement alone cannot differentiate electronic state on surface of TIs from other material such as graphene since it has similar behavior, so the conducting measurement is not striking. A more precise method to measure TI surface state is Hall measurement. Results show the quantum oscillation of Hall resistance and fitting curve provides a low value of 2D carrier density, cyclotron mass, and Fermi vector. Together with the previous resistance measurements, we can make a conclusion that this work provides a near ideal TI base system $(Sb_{0.957}Bi_{0.043})_2Te_3$ for further scientific research and device application. However, the most direct and convincible method to detect the surface state is to "see" trough Angle Resolved Photo Emission Spectroscopy (ARPES), which is ideal tool to measure energy dispersion of surface states of a solid $E(\overrightarrow{k_x}, \overrightarrow{k_y})$ as function of momentum $\hbar\overrightarrow{k_x}$, $\hbar\overrightarrow{k_x}$. Due to the instrument limitation, I did not get access to ARPES but there are several other research groups show ARPES results of similar system.

Another important feature that TIs have is that their robust surface state is protected by time-reversal symmetry (TRS) which suppresses the electron backscattering with impurities other than what can break TRS such as magnetic field and magnetization. When applying a magnetic field normal to the surface or by inducing a net out-of-surface magnetization in the material, TRS is broken on the surface state, creating an energy splitting between the electron with spin-up and spin-down surface bands. This opening of surface band gap is phenomenal

not only because it is the first experimental system example to observe Quantum Anomalous Hall effect but also shine the light on possible application of these material to magnetic sensor field. Therefore, the last part of thesis on TI project are mainly based on the exploration of magnetically doped TI systems and their application as magnetic sensors. Cr doped Bi_2Te_3 TI thin film are presented to study the transport properties with various magnetic element doping concentrations. As increasing magnetic doping in Bi_2Te_3, a ferromagnetic phase transition is developing over certain Cr concentration corresponding to observation of anomalous Hall effect afterwards on Hall resistance. Arrot plot shows the ferromagnetism in TIs may result from RKKY interaction of magnetic impurities consisting of Heisenberg-like, Ising-like, and Dzyaloshinskii-Moriya-like terms. Hall effect sensors and anomalous Hall effect sensors are developed based on Mn doped and Cr doped Bi_2Te_3 systems. Ultrahigh Hall sensitivity of the sensor are found due to the ferromagnetism induced anomalous Hall effect. The significance of the present work is the development of a prototype Hall sensor using this novel kind of newly discovered materials. It is the first attempt of making a micro magnetic sensor out of TIs focusing on its magnetic properties. There are other groups also working on devices such as transistor based on TIs emphasizing on their extraordinary carrier mobility.

Topological insulators is an exciting topics both in theory and practice. There are lots of theoretical developments describing the possible types of TIs, classifying them, the possible kinds of physical consequences that they may have such as quantum anomalous Hall effect. It combines mathematics, physics and chemistry in a very intimate way, it's been an exciting topic last five to ten years that this field has seen an enormous development. Experimentally, there are several approaches for the future study. First is the attempt to find new and better materials of various kinds TIs. And the second direction is for existing materials to actually

measure surface transport properties, optical properties and magnetic properties to demonstrate that the topological materials are actually behaving in the way that they are supposed to be behaving, or perhaps in surprising ways that we didn't anticipate. And then a ultimate goal is applications. In this work, we made Hall sensor out of TIs. There are certainly potential applications in other perspectives, researches are using the edge channels as wires in micro-electronic devices or for sending signals; some applications that have to do with the magneto-electric coupling; TIs are also proposed to use in quantum computing by designing qubits.

In order to realize the proposed TI based device, another interesting material which is multiferroic has been investigated in the second part of thesis. This is because we need to use electric field to control the direction of magnetizations so that through the proximity effect, the spin of magnetically doped TI can be aligned out-of- surface. Magnetoelectric multiferroic materials is a kind of novel material become striking due to its multifunctionality, displaying magnetization and dielectric polarization in the same material, for a variety of device application. The single phase multiferroic materials such as $BiFeO_3$, in which ferromagnetic and ferroelectric order spontaneous appear and couple, are rare in nature. Besides, the coupling of the two orders in bulk single phase material is too weak to utilize in device and sensors. Intensive researches are being pursued towards strengthen of magneto-electric coupling and design of new materials with stronger coupling. Another approach is to use indirect coupling of ferromagnetic and ferroelectric properties of different materials in order to get strong magnetoelectric (ME) coefficient, for example couple the two orders through induced strain in crystal lattices. This can be achieved because of the general exists of magnetostriction of ferromagnetic materials and piezoelectricity of ferroelectric materials. By combining high magnetostrictive material with high piezoelectric material into different structural composites,

the ME coefficient is expected to be higher than that of the single phase materials. By making the multi-phase multiferroic materials, the property of controlling magnetic properties by applying electric field and vice versa is expected not only be accomplished in lab researches but also been implemented in industry. Therefore, in my work, I choose the most common and cheap non rare earth ferromagnetic with highest magnetostriction ceramic, cobalt ferrite ($CoFe_2O_4$) as the ferromagnetic element in ME composite; Following the same idea, I choose barium titanate ($BaTiO_3$) which is the most common room temperature piezoelectric material with relative high piezoelectric coefficient as ferroelectric element in composite. The most widely used ceramic fabrication process, solid state reaction method, is used to combine the two into composites. I find the ME coefficient value varies with tuning the concentration of elements in the composites. By doping Ga into cobalt ferrite, the magnetostriction derivative ($d\lambda/dH$) increases in compounds. Then synthesis composite Ga doped $CoFe_2O_4$ power with $BaTiO_3$ power into composites, the overall ME coefficient are expected to increase after calculation. This results provide the new approach to enhance the ME coefficient by increasing the sensitivity of each element, magnetostriction derivative ($d\lambda/dH$) and piezoelectricity ($dE/d\lambda$) in composite. Besides that, the doping element, Ga, improves the solution of long-standing current leaking problem in ME materials. What's more, the experiment I designed using the most common materials and most easy method to fabricate the sample, which offer the opportunity to apply in a large scale industry manufacture.

Recent experimental results show a huge increase of ME coefficient in low dimensional ME materials such as thin films. This is a further step toward the implementation of micro device application, especially, as the sensors and transducer requires much smaller size, higher capability, more efficient and lower energy consumption. For the future work, I would like to

apply the current bulk material Ga doped $CoFe_2O_4/BaTiO_3$ composite to thin film samples. Paused Laser deposition (PLD) is an effective and efficient method to fabricate thin film oxidize samples. Thickness influence on ME coefficient can also be investigated. The ultimate goal is to make micro or nano electronic devices out of the current system. For example, to design a new kind of read-write head sensor for magnetic recording technique. Dr. Nan's group have demonstrated a prototype ME read heading using $CoFe_2O_4/BaTiO_3$ bilayer ME heterostructures. Their experimental results show the output voltage waveform of the ME reader can follow magnetic excitation waveform. This new kind of read head become promising because of its less power consumption, smaller size and simpler structure than the conventional magnetoresistance sensor. However, sensitivity of the current ME reading head is not as high as the Giant Magnetoresistance (GMR) sensor. What is more, the recording densities which relies on the ME heterostructure, is not large enough to apply in future high density magnetic recording techniques. Therefore, further research need to be done in improving the performance of current sensor including using much higher ME coefficient materials. To understand ME coupling in the heterostructure also plays an important role to design better ME sensors. However, the cost of the thin film material might be much higher than the conventional material regarding to the device application in industry.

REFERENCES

[1] P. Ripka, *Magnetic sensors and magnetometers*. Artech House, 2001.

[2] E. H. Hall, "On a new action of the magnet on electric currents," *American Journal of Mathematics*, vol. 2, no. 3, pp. 287-292, 1879.

[3] Y. Kato, R. Myers, A. Gossard, and D. Awschalom, "Observation of the spin Hall effect in semiconductors," *science*, vol. 306, no. 5703, pp. 1910-1913, 2004.

[4] K. v. Klitzing, G. Dorda, and M. Pepper, "New method for high-accuracy determination of the fine-structure constant based on quantized Hall resistance," *Physical Review Letters*, vol. 45, no. 6, p. 494, 1980.

[5] T. Ando, Y. Matsumoto, and Y. Uemura, "Theory of Hall effect in a two-dimensional electron system," *Journal of the Physical Society of Japan*, vol. 39, no. 2, pp. 279-288, 1975.

[6] K. Von Klitzing, "25 Years of quantum Hall effect (QHE) a personal view on the discovery, physics and applications of this quantum effect," in *The Quantum Hall Effect*: Springer, pp. 1-21, 2005.

[7] Y. Ando, "Topological insulator materials," *Journal of the Physical Society of Japan*, vol. 82, no. 10, p. 102001, 2013.

[8] M. König *et al.*, "The quantum spin Hall effect: theory and experiment," *Journal of the Physical Society of Japan*, vol. 77, no. 3, p. 031007, 2008.

[9] C. L. Kane and E. J. Mele, "Quantum spin Hall effect in graphene," *Physical review letters*, vol. 95, no. 22, p. 226801, 2005.

[10] B. A. Bernevig, T. L. Hughes, and S.-C. Zhang, "Quantum spin Hall effect and topological phase transition in HgTe quantum wells," *Science*, vol. 314, no. 5806, pp. 1757-1761, 2006.

[11] M. König *et al.*, "Quantum spin Hall insulator state in HgTe quantum wells," *Science*, vol. 318, no. 5851, pp. 766-770, 2007.

[12] A. Stern, "Fractional Topological Insulators--a Pedagogical Review," *arXiv preprint arXiv:1509.02698*, 2015.

[13] H. C. Manoharan, "Topological insulators: A romance with many dimensions," *Nature nanotechnology*, vol. 5, no. 7, pp. 477-479, 2010.

[14] C. L. Kane and E. J. Mele, "Z2 topological order and the quantum spin Hall effect," *Physical review letters*, vol. 95, no. 14, p. 146802, 2005.

[15] J. E. Moore, "The birth of topological insulators," *Nature*, vol. 464, no. 7286, pp. 194-198, 2010.

[16] K. Nomura and N. Nagaosa, "Surface-quantized anomalous Hall current and the magnetoelectric effect in magnetically disordered topological insulators," *Physical review letters*, vol. 106, no. 16, p. 166802, 2011.

[17] J. Gao, L. Shen, Y. Wang, D. Gray, J. Li, and D. Viehland, "Enhanced sensitivity to direct current magnetic field changes in Metglas/Pb ($Mg_{1/3}Nb_{2/3}$) O_3–$PbTiO_3$ laminates," *Journal of Applied Physics*, vol. 109, no. 7, pp. 074507-074507-3, 2011.

[18] D. Kong *et al.*, "Ambipolar field effect in the ternary topological insulator (Bi_xSb_{1-x}) $_2Te_3$ by composition tuning," *Nature nanotechnology*, vol. 6, no. 11, pp. 705-709, 2011.

[19] X.-L. Qi and S.-C. Zhang, "Topological insulators and superconductors," *Reviews of Modern Physics*, vol. 83, no. 4, p. 1057, 2011.

[20] C. Z. Chang *et al.*, "Thin Films of Magnetically Doped Topological Insulator with Carrier‐Independent Long‐Range Ferromagnetic Order," *Advanced Materials*, vol. 25, no. 7, pp. 1065-1070, 2013.

[21] N. Nagaosa, J. Sinova, S. Onoda, A. MacDonald, and N. Ong, "Anomalous hall effect," *Reviews of modern physics*, vol. 82, no. 2, p. 1539, 2010.

[22] K. He, "Viewpoint: The Quantum Hall Effect Gets More Practical," *Physics*, vol. 8, p. 41, 2015.

[23] S. Oh, "The complete quantum Hall trio," *Science*, vol. 340, no. 6129, pp. 153-154, 2013.

[24] C.-Z. Chang *et al.*, "Experimental observation of the quantum anomalous Hall effect in a magnetic topological insulator," *Science*, vol. 340, no. 6129, pp. 167-170, 2013.

[25] L. Fu, C. L. Kane, and E. J. Mele, "Topological Insulators in Three Dimensions," *Physical Review Letters,* vol. 98, no. 10, p. 106803, 2007.

[26] A. Nishide *et al.*, "Direct mapping of the spin-filtered surface bands of a three-dimensional quantum spin Hall insulator," *Physical Review B,* vol. 81, no. 4, p. 041309, 2010.

[27] D. Hsieh *et al.*, "A topological Dirac insulator in a quantum spin Hall phase," *Nature,* vol. 452, no. 7190, pp. 970-974, 2008.

[28] H.-J. Zhang *et al.*, "Electronic structures and surface states of the topological insulator $Bi_{1-x}Sb_x$," *Physical Review B,* vol. 80, no. 8, p. 085307, 2009.

[29] J. C. Teo, L. Fu, and C. Kane, "Surface states and topological invariants in three-dimensional topological insulators: Application to $Bi_{1-x}Sb_x$," *Physical Review B,* vol. 78, no. 4, p. 045426, 2008.

[30] Y. Xia *et al.*, "Observation of a large-gap topological-insulator class with a single Dirac cone on the surface," *Nature Physics,* vol. 5, no. 6, pp. 398-402, 2009.

[31] Y. Chen *et al.*, "Experimental realization of a three-dimensional topological insulator, Bi_2Te_3," *Science,* vol. 325, no. 5937, pp. 178-181, 2009.

[32] D. Hsieh *et al.*, "A tunable topological insulator in the spin helical Dirac transport regime," *Nature,* vol. 460, no. 7259, pp. 1101-1105, 2009.

[33] C. Jin *et al.*, "New quantum matters: Build up versus high pressure tuning," *Science China Physics, Mechanics and Astronomy,* vol. 56, no. 12, pp. 2337-2350, 2013.

[34] A. P. Pyatakov and A. K. Zvezdin, "Magnetoelectric and multiferroic media," *Physics-Uspekhi,* vol. 55, no. 6, pp. 557-581, 2012.

[35] P. J. Curie, *de physique*. Paris, 1894.

[36] W. Eerenstein, N. D. Mathur, and J. F. Scott, "Multiferroic and magnetoelectric materials," *Nature,* vol. 442, no. 7104, pp. 759-765, 2006.

[37] J. P. Rivera, "On definitions, units, measurements, tensor forms of the linear magnetoelectric effect and on a new dynamic method applied to Cr-Cl boracite," *Ferroelectrics,* vol. 161, no. 1, pp. 165-180, 1994.

[38] H. Schmid, "Multi-ferroic magnetoelectrics," *Ferroelectrics,* vol. 162, no. 1, pp. 317-338, 1994.

[39] L. D. Landau, J. Bell, M. Kearsley, L. Pitaevskii, E. Lifshitz, and J. Sykes, *Electrodynamics of continuous media*. elsevier, 1984.

[40] E. Ascher, H. Rieder, H. Schmid, and H. Stössel, "Some Properties of Ferromagnetoelectric Nickel‐Iodine Boracite, NiBOI," *Journal of Applied Physics*, vol. 37, p. 1404, 1966.

[41] A. Filippetti and N. A. Hill, "Coexistence of magnetism and ferroelectricity in perovskites," *Physical Review B*, vol. 65, no. 19, p. 195120, 2002.

[42] N. A. Hill, "First principles study of multiferroic magnetoelectric manganites," in *AIP Conference Proceedings*, 2000, vol. 535, p. 372.

[43] N. A. Hill and K. M. Rabe, "First-principles investigation of ferromagnetism and ferroelectricity in bismuth manganite," *Physical Review B*, vol. 59, no. 13, pp. 8759-8769, 1999.

[44] G. Smolenskii, V. Isupov, and A. Agranovskaya, "New ferroelectrics of complex composition of the Type $A_2^{2+}(BI^{3+} BII^{5+}) O_6$. I," *Sov. Phys. Solid State*, vol. 1, pp. 150-151, 1959.

[45] G. Smolenskii and I. Chupis, "Ferroelectromagnets," *Phys. Usp*, vol. 25, pp. 475-493, 1982.

[46] A. Van Run, D. Terrell, and J. Scholing, "An in situ grown eutectic magnetoelectric composite material," *Journal of Materials Science*, vol. 9, no. 10, pp. 1710-1714, 1974.

[47] E. Y. Tsymbal, E. R. Dagotto, C.-B. Eom, and R. Ramesh, *Multifunctional oxide heterostructures*. OUP Oxford, 2012.

[48] M. Bibes, "Nanoferronics is a winning combination," *Nature Materials*, vol. 11, no. 5, pp. 354-357, 2012.

[49] J. Van Suchtelen, "Product properties: a new application of composite materials," *Philips Res. Rep*, vol. 27, no. 1, pp. 28-37, 1972.

[50] R. Newnham, D. Skinner, and L. Cross, "Connectivity and piezoelectric-pyroelectric composites," *Materials Research Bulletin*, vol. 13, no. 5, pp. 525-536, 1978.

[51] C. W. Nan, "Magnetoelectric effect in composites of piezoelectric and piezomagnetic phases," *Physical Review B*, vol. 50, no. 9, p. 6082, 1994.

[52] J. Ryu, A. V. Carazo, K. Uchino, and H.-E. Kim, "Piezoelectric and magnetoelectric properties of lead zirconate titanate/Ni-ferrite particulate composites," *Journal of Electroceramics,* vol. 7, no. 1, pp. 17-24, 2001.

[53] C. W. Nan, M. Bichurin, S. Dong, D. Viehland, and G. Srinivasan, "Multiferroic magnetoelectric composites: Historical perspective, status, and future directions," *Journal of Applied Physics,* vol. 103, no. 3, pp. 031101-031101-35, 2008.

[54] A. Cho and P. Dernier, "Single‐crystal‐aluminum Schottky‐barrier diodes prepared by molecular‐beam epitaxy (MBE) on GaAs," *Journal of Applied Physics,* vol. 49, no. 6, pp. 3328-3332, 1978.

[55] T. Zhu, P. Chen, Q. Zhang, R. Yu, and B. Liu, "Giant linear anomalous Hall effect in the perpendicular CoFeB thin films," *Applied Physics Letters,* vol. 104, no. 20, p. 202404, 2014.

[56] R. E. Honig and D. A. Kramer, "Vapor-pressure data for the solid and liquid elements," 1970.

[57] A. A. Taskin, S. Sasaki, K. Segawa, and Y. Ando, "Achieving Surface Quantum Oscillations in Topological Insulator Thin Films of Bi_2Se_3," *Advanced Materials,* vol. 24, no. 41, pp. 5581-5585, 2012.

[58] H. D. Li *et al.*, "The van der Waals epitaxy of Bi_2Se_3 on the vicinal Si(111) surface: an approach for preparing high-quality thin films of a topological insulator," *New Journal of Physics,* vol. 12, no. 10, p. 103038, 2010.

[59] S. Schreyeck *et al.*, "Molecular beam epitaxy of high structural quality Bi_2Se_3 on lattice matched InP(111) substrates," *Applied Physics Letters,* vol. 102, no. 4, pp. 041914, 2013.

[60] Z. Zeng *et al.*, "Molecular beam epitaxial growth of Bi_2Te_3 and Sb_2Te_3 topological insulators on GaAs (111) substrates: a potential route to fabricate topological insulator p-n junction," *AIP Advances,* vol. 3, no. 7, pp. 072112, 2013.

[61] Y. Ni, Z. Zhang, I. C. Nlebedim, R. L. Hadimani, G. Tuttle, and D. C. Jiles, "Ferromagnetism of magnetically doped topological insulators in $Cr_xBi_{2-x}Te_3$ thin films," *Journal of Applied Physics,* vol. 117, no. 17, p. 17C748, 2015.

[62] Y. Ni, Z. Zhang, I. C. Nlebedim, R. L. Hadimani, and D. C. Jiles, "Influence of Mn Concentration on Magnetic Topological Insulator $Mn_xBi_{2-x}Te_3$ Thin-Film Hall-Effect Sensor," *Magnetics, IEEE Transactions on,* vol. 51, no. 11, pp. 1-4, 2015.

[63] D.-X. Qu, Y. S. Hor, J. Xiong, R. J. Cava, and N. P. Ong, "Quantum Oscillations and Hall Anomaly of Surface States in the Topological Insulator Bi_2Te_3," *Science*, vol. 329, no. 5993, pp. 821-824, 2010.

[64] H. Peng *et al.*, "Topological insulator nanostructures for near-infrared transparent flexible electrodes," *Nature Chemistry*, vol. 4, no. 4, pp. 281-286, 2012.

[65] H. Zhang, C.-X. Liu, X.-L. Qi, X. Dai, Z. Fang, and S.-C. Zhang, "Topological insulators in Bi_2Se_3, Bi_2Te_3 and Sb_2Te_3 with a single Dirac cone on the surface," *Nature physics*, vol. 5, no. 6, pp. 438-442, 2009.

[66] Y. Liu *et al.*, "Tuning Dirac states by strain in the topological insulator Bi_2Se_3," *Nature Physics*, vol. 10, no. 4, pp. 294-299, 2014.

[67] J. Zhang *et al.*, "Band structure engineering in (Bi1−xSbx)2Te3 ternary topological insulators," *Nature Communication*, vol. 2, p. 574, 2011.

[68] C. Zhang *et al.*, "Observations of a Metal–Insulator Transition and Strong Surface States in $Bi_{2-x}Sb_xSe_3$ Thin Films," *Advanced Materials*, vol. 26, no. 41, pp. 7110-7115, 2014.

[69] L. Bao *et al.*, "Quantum Corrections Crossover and Ferromagnetism in Magnetic Topological Insulators," *Scientific Reports*, vol. 3, p. 2391, 2013.

[70] S. Hikami, A. I. Larkin, and Y. Nagaoka, "Spin-Orbit Interaction and Magnetoresistance in the Two Dimensional Random System," *Progress of Theoretical Physics*, vol. 63, no. 2, pp. 707-710, 1980.

[71] H. Steinberg, J. B. Laloë, V. Fatemi, J. S. Moodera, and P. Jarillo-Herrero, "Electrically tunable surface-to-bulk coherent coupling in topological insulator thin films," *Physical Review B*, vol. 84, no. 23, p. 233101, 2011.

[72] B. L. Altshuler, A. G. Aronov, and D. E. Khmelnitsky, "Effects of electron-electron collisions with small energy transfers on quantum localisation," *Journal of Physics C: Solid State Physics*, vol. 15, no. 36, p. 7367, 1982.

[73] A. A. Taskin and Y. Ando, "Quantum oscillations in a topological insulator $Bi_{1-x}Sb_x$," *Physical Review B*, vol. 80, no. 8, p. 085303, 2009.

[74] H.-T. He *et al.*, "Impurity Effect on Weak Antilocalization in the Topological Insulator Bi_2Te_3," *Physical Review Letters*, vol. 106, no. 16, p. 166805, 2011.

[75] T. Habe and Y. Asano, "Interface metallic states between a topological insulator and a ferromagnetic insulator," *Physical Review B,* vol. 85, no. 19, p. 195325, 2012.

[76] Q. Liu, C.-X. Liu, C. Xu, X.-L. Qi, and S.-C. Zhang, "Magnetic Impurities on the Surface of a Topological Insulator," *Physical Review Letters,* vol. 102, no. 15, p. 156603, 2009.

[77] R. Yu, W. Zhang, H.-J. Zhang, S.-C. Zhang, X. Dai, and Z. Fang, "Quantized Anomalous Hall Effect in Magnetic Topological Insulators," *Science,* vol. 329, no. 5987, pp. 61-64, 2010.

[78] M. Liu *et al.*, "Crossover between Weak Antilocalization and Weak Localization in a Magnetically Doped Topological Insulator," *Physical Review Letters,* vol. 108, no. 3, p. 036805, 2012.

[79] J.-J. Zhu, D.-X. Yao, S.-C. Zhang, and K. Chang, "Electrically Controllable Surface Magnetism on the Surface of Topological Insulators," *Physical Review Letters,* vol. 106, no. 9, p. 097201, 2011.

[80] L. Bao *et al.*, "Quantum Corrections Crossover and Ferromagnetism in Magnetic Topological Insulators," *Scientific reports,* vol. 3, 2391, 2013.

[81] A. Arrott, "Criterion for ferromagnetism from observations of magnetic isotherms," *Physical Review,* vol. 108, no. 6, p. 1394, 1957.

[82] A. Arrott and J. E. Noakes, "Approximate Equation of State For Nickel Near its Critical Temperature," *Physical Review Letters,* vol. 19, no. 14, pp. 786-789, 1967.

[83] K. Wang *et al.*, "High-quality Bi_2Te_3 thin films grown on mica substrates for potential optoelectronic applications," *Applied Physics Letters,* vol. 103, no. 3, p. 031605, 2013.

[84] D. Zhang *et al.*, "Interplay between ferromagnetism, surface states, and quantum corrections in a magnetically doped topological insulator</title>," *Physical Review B,* vol. 86, no. 20, p. 205127, 2012.

[85] J. Van den Boomgaard, A. Van Run, and J. V. Suchtelen, "Magnetoelectricity in piezoelectric-magnetostrictive composites," *Ferroelectrics,* vol. 10, no. 1, pp. 295-298, 1976.

[86] H. Lind and S. Lidin, "A general structure model for Bi–Se phases using a superspace formalism," *Solid State Sciences,* vol. 5, no. 1, pp. 47-57, 2003.

[87] Y. S. Hor *et al.*, "Superconductivity in $Cu_xBi_2Se_3$ and its Implications for Pairing in the Undoped Topological Insulator," *Physical Review Letters,* vol. 104, no. 5, p. 057001, 2010.

[88] P. E. Salman Z, Pomjakushin V, Kanigel A, Chashka K, Conder K, Morenzoni E, Prokscha T, Sedlak K and Suter A, " The nature of magnetic ordering in magnetically doped topological insulator $Bi_{2-x}Fe_xSe_3$ " arXiv:1203.4850, 2012.

[89] C. A. F. Vaz, J. A. C. Bland, and G. Lauhoff, "Magnetism in ultrathin film structures," *Reports on Progress in Physics,* vol. 71, no. 5, p. 056501, 2008.

[90] H. Ohno *et al.*, "Electric-field control of ferromagnetism," *Nature,* vol. 408, no. 6815, pp. 944-946, 2000.

[91] J. G. Checkelsky, J. Ye, Y. Onose, Y. Iwasa, and Y. Tokura, "Dirac-fermion-mediated ferromagnetism in a topological insulator," *Nature Physics,* vol. 8, no. 10, pp. 729-733, 2012.

[92] E. Ramsden, *Hall-effect sensors: theory and application*. Newnes, 2011.

[93] R. S. Popovic, *Hall effect devices*. CRC Press, 2003.

[94] V. Kulbachinskii *et al.*, "Ferromagnetism in new diluted magnetic semiconductor $Bi_{2-x}Fe_xTe_3$," *Physica B: Condensed Matter,* vol. 311, no. 3, pp. 292-297, 2002.

[95] M. Z. Hasan and C. L. Kane, "Colloquium: topological insulators," *Reviews of Modern Physics,* vol. 82, no. 4, p. 3045, 2010.

[96] Y. Ni, Z. Zhang, I. C. Nlebedim, R. Hadimani, G. Tuttle, and D. C. Jiles, "Ferromagnetism of magnetically doped topological insulators in $Cr_xBi_{2-x}Te_3$ thin films," *Journal of Applied Physics,* vol. 117, no. 17, p. 17C748, 2015.

[97] X. Chen *et al.*, "Thermal expansion coefficients of Bi_2Se_3 and Sb_2Te_3 crystals from 10 K to 270 K," *Applied Physics Letters,* vol. 99, no. 26, p. 261912, 2011.

[98] J. Choi *et al.*, "Magnetic properties of Mn - doped Bi_2Te_3 and Sb_2Te_3," *Physica Status Solidi (b),* vol. 241, no. 7, pp. 1541-1544, 2004.

[99] J. Bos *et al.*, "Ferromagnetism below 10 K in Mn-doped BiTe," *Physical Review B,* vol. 74, no. 18, p. 184429, 2006.

[100] M. Watson *et al.*, "Study of the structural, electric and magnetic properties of Mn-doped Bi_2Te_3 single crystals," *New Journal of Physics,* vol. 15, no. 10, p. 103016, 2013.

[101] J. Růžička *et al.*, "Structural and electronic properties of manganese-doped Bi_2Te_3 epitaxial layers," *New Journal of Physics,* vol. 17, no. 1, p. 013028, 2015.

[102] D.-X. Qu, Y. Hor, J. Xiong, R. Cava, and N. Ong, "Quantum oscillations and Hall anomaly of surface states in the topological insulator Bi_2Te_3," *Science,* vol. 329, no. 5993, pp. 821-824, 2010.

[103] Y. Ni, Z. Zhang, C. I. Nlebedim, and D. C. Jiles, "Influence of Ga-concentration on the electrical and magnetic properties of magnetoelectric $CoGa_xFe_{2-x}O_4/BaTiO_3$ composite," *Journal of Applied Physics,* vol. 117, no. 17, p. 17B906, 2015.

[104] A. Gerber and O. Riss, "Perspective of spintronics applications based on the extraordinary hall effect," *Journal of Nanoelectronics and Optoelectronics,* vol. 3, no. 1, pp. 35-43, 2008.

[105] Y. Lu, J. Cai, H. Pan, and L. Sun, "Ultrasensitive anomalous Hall effect in SiO_2/Fe-Pt/SiO_2 sandwich structure films," *Applied Physics Letters,* vol. 100, no. 2, p. 022404, 2012.

[106] S. Zhang *et al.*, "Large enhancement of the anomalous Hall effect in Co/Pt multilayers sandwiched by MgO layers," *Applied Physics Letters,* vol. 97, no. 22, p. 222504, 2010.

[107] S. Ikeda *et al.*, "A perpendicular-anisotropy CoFeB–MgO magnetic tunnel junction," *Nature Materials,* vol. 9, no. 9, pp. 721-724, 2010.

[108] S.-g. Cheng, "The quantum anomalous Hall effect in a topological insulator thin film—The role of magnetic disorder," *EPL (Europhysics Letters),* vol. 105, no. 5, p. 57004, 2014.

[109] M. Onoda and N. Nagaosa, "Topological nature of anomalous Hall effect in ferromagnets," *Journal of the Physical Society of Japan,* vol. 71, no. 1, pp. 19-22, 2002.

[110] T. Fujita, M. B. A. Jalil, and S. G. Tan, "Topological insulator cell for memory and magnetic sensor applications," *Applied Physics Express,* vol. 4, no. 9, p. 094201, 2011.

[111] M. B. Jalil, S. Tan, and Z. Siu, "Quantum anomalous Hall effect in topological insulator memory," *Journal of Applied Physics*, vol. 117, no. 17, p. 17C739, 2015.

[112] J.-S. Lee, K.-H. Ahn, Y.-H. Jeong, and D. M. Kim, "Quantum-well Hall devices in Si-delta-doped $Al_{0.25}Ga_{0.75}As$/GaAs and pseudomorphic $Al_{0.25}Ga_{0.75}As/In_{0.25}Ga_{0.75}As$/GaAs heterostructures grown by LP-MOCVD: performance comparisons," *Electron Devices, IEEE Transactions on*, vol. 43, no. 10, pp. 1665-1670, 1996.

[113] J. Ryu, S. Priya, K. Uchino, and H.-E. Kim, "Magnetoelectric effect in composites of magnetostrictive and piezoelectric materials," *Journal of electroceramics*, vol. 8, no. 2, pp. 107-119, 2002.

[114] B. Li, C. Q. Wang, W. Zhang, C. J. Hang, J. M. Fei, and H. Wang, "Fabrication of multiferroic $Ba_{0.7}Sr_{0.3}TiO_3$-$Ni_{0.8}Zn_{0.2}Fe_2O_4$ composite nanofibers by electrospinning,", *Materials Letters*, vol. 91, pp. 55-58, Jan 2013.

[115] R. C. Kambale, D.-Y. Jeong, and J. Ryu, "Current Status of Magnetoelectric Composite Thin/Thick Films," *Advances in Condensed Matter Physics*, vol. 2012, 824643, 2012.

[116] M. Liu *et al.*, "Giant electric field tuning of magnetic properties in multiferroic ferrite/ferroelectric heterostructures," *Advanced Functional Materials*, vol. 19, no. 11, pp. 1826-1831, 2009.

[117] V. Corral-Flores, D. Bueno-Baques, and R. Ziolo, "Synthesis and characterization of novel $CoFe_2O_4$–$BaTiO_3$ multiferroic core–shell-type nanostructures," *Acta Materialia*, vol. 58, no. 3, pp. 764-769, 2010.

[118] Q. Jiang, Z. Shen, J. Zhou, Z. Shi, and C.-W. Nan, "Magnetoelectric composites of nickel ferrite and lead zirconnate titanate prepared by spark plasma sintering," *Journal of the European Ceramic Society*, vol. 27, no. 1, pp. 279-284, 2007.

[119] S. Tan, S. Shannigrahi, S. Tan, and F. Tay, "Synthesis and characterization of composite $MgFe_2O_4$–$BaTiO_3$ multiferroic system," *Journal of Applied Physics*, vol. 103, no. 9, p. 094105, 2008.

[120] I. Nlebedim, Y. Melikhov, J. Snyder, N. Ranvah, A. Moses, and D. Jiles, "Dependence of magnetomechanical performance of $CoGa_xFe_{2-x}O_4$ on temperature variation," *Journal of Applied Physics*, vol. 109, no. 7, p. 07A908, 2011.

[121] S. Song, C. Lo, S. Lee, S. Aldini, J. Snyder, and D. Jiles, "Magnetic and magnetoelastic properties of Ga-substituted cobalt ferrite," *Journal of Applied Physics*, vol. 101, no. 9, pp. 09C517, 2007.

[122] S. Halgedah and M. Fuller, "The dependence of magnetic domain structure upon magnetization state with emphasis upon nucleation as a mechanism for pseudo - single - domain behavior," *Journal of Geophysical Research: Solid Earth*, vol. 88, no. B8, pp. 6505-6522, 1983.

[123] K. Itoh and M. Kinoshita, *Molecular magnetism: new magnetic materials*. Kodansha, 2000.

[124] I. Nlebedim, M. Vinitha, P. Praveen, D. Das, and D. Jiles, "Temperature dependence of the structural, magnetic, and magnetostrictive properties of zinc-substituted cobalt ferrite," *Journal of Applied Physics*, vol. 113, no. 19, p. 193904, 2013.

[125] Z. Wang *et al.*, "Magnetoelectric effect in crystallographically textured $BaTiO_3$ films deposited on ferromagnetic metallic glass foils," *Journal of Applied Physics*, vol. 109, no. 3, p. 034102, 2011.

[126] T. Li, "Ultrafast laser spectroscopy in complex solid state materials," *PhD thesis*, 2014.